論文 / 著書情報
Article / Book Information

題目(和文)	Aサイトオーダー型ダブルペロブスカイト鉄酸化物における原子価混合-分離転移
Title(English)	Valence mixing-separation transition in A-site ordered double-perovskite iron-oxide systems
著者(和文)	中村仁
Author(English)	Jin Nakamura
出典(和文)	学位:博士(理学), 学位授与機関:東京工業大学, 報告番号:甲第5325号, 授与年月日:2003年3月26日, 学位の種別:課程博士, 審査員:
Citation(English)	Degree:Doctor (Science), Conferring organization: Tokyo Institute of Technology, Report number:甲第5325号, Conferred date:2003/3/26, Degree Type:Course doctor, Examiner:
学位種別(和文)	博士論文
Type(English)	Doctoral Thesis

Valence Mixing-Separation Transition in *A*-site Ordered Double-Perovskite Iron-Oxide Systems

Jin NAKAMURA

00D26074

A Thesis Submitted to the Interdisciplinary Graduate School
of Science and Engineering
through the Department of Innovative and Engineered Materials
in Partial Fulfillment of the Requirements for the Degree of Doctor of Science
at Tokyo Institute of Technology

Supervisors :

Prof. Hisao YAMAUCHI and Prof. Maarit KARPPINEN

March, 2003

Notes:

1. The references are indicated as follows:

   - [I], [II], [III], ... for the papers including my name (**J. Nakamura**)
   - [1], [2], [3], ... for the other papers

2. The oxidation state of an element is expressed for, *e.g.* divalent iron, as follows:

   - Fe^{2+} in solutions
   - Fe^{II} in solids

   A mixed valent state, *e.g.* $Fe^{2.5+}$, is written with an Arabic figure.

Contents

Chapter 1. Introduction **1**
1.1 Background of the Present Work 1
1.1.1 *A*-site Ordered Double Perovskite 1
1.1.2 Verwey-Type Transition in Ba*RE*$Fe_2O_{5+\delta}$ 3
1.1.3 Single-Perovskite Iron-Oxides 7
1.1.4 Verwey transition in Magnetite (Fe_3O_4) 8
1.2 Objectives of the Present Work 12

Chapter 2. Experimental **13**
2.1 Sample Synthesis 13
2.2 Control of Excess Oxygen Amount 14
2.3 Characterization 14
2.3.1 Determination of Excess Oxygen Amount 14
2.3.2 Determination of Phase Purity and Unit-Cell Parameters 16
2.3.3 Precise Studies of the Structures 16
2.3.4 Differential Scanning Calorimetry (DSC) 16
2.3.5 Magnetic Property Measurements 17
2.3.6 Electrical Transport Property Measurements 17
2.3.7 TEM Observation 17
2.3.8 Mössbauer Spectroscopy 18
2.3.9 SEM Observation 19
2.3.10 Band Structure Calculation 19

Chapter 3. New Synthesis Technique for (Ba,Sr)(*RE*,Ca)$Fe_2O_{5+\delta}$ **21**
3.1 Encapsulation Technique with Oxygen Getter 21
3.2 Sample Quality and Solubility Limit 29
3.3 Conclusion 35

Chapter 4. Magnetic and Magnetoresistance Properties **37**
4.1 Introduction 37
4.2 Results and Discussions 40

4.2.1 Magnetic Properties of BaREFe$_2$O$_{5+\delta}$ 40
4.2.2 Magnetoresistance Properties of BaREFe$_2$O$_{5+\delta}$ 42
4.3 Conclusion 47

Chapter 5. Oxidation Schemes 49
5.1 Introduction 49
5.2 Results and Discussions 50
5.2.1 Oxidation Schemes by Excess Oxygen and Ca Substitution 50
5.2.2 Differences between Two Oxidation Schemes 56
5.3 Conclusion 63

Chapter 6. Iso-Valent Substitution Schemes 65
6.1 Introduction 65
6.2 Results and Discussions 66
6.2.1 Change in the Lattice Parameters 66
6.2.2 The Change of T_V 68
6.3 Conclusion 79

Chapter 7. Charge Ordering and Premonitory Transition 81
7.1 Introduction 81
7.2 Results and Discussions 83
7.2.1 Charge Ordering 83
7.2.2 Premonitory Transition 87
7.3 Conclusion 90

Chapter 8. Suggestions for Future Works 91

Chapter 9. Summary 95

References 98
Acknowledgments 109
Curriculum Vitae 110

Chapter 1. Introduction

1.1 Background of the Present Work

1.1.1 *A*-site Ordered Double Perovskite

An *A*-site ordered double perovskite, $AA'B_2O_{5+\delta}$, is derived from the simple perovskite, $ABO_{3-\delta}$, by co-occupation of the *A* site by two different cations with different charges and/or sizes. In Fig. 1.1.1 the structures of a simple perovskite and an *A*-site ordered double perovskite are represented. In the double perovskite *A*, *A'* and *B* sites are typically occupied by alkaline earth, rare earth and transition metal elements, respectively. The two different *A* atoms, *A* and *A'*, are ordered along the *c* axis. Therefore the unit cell contains two perovskite blocks, that is, "double perovskite". An *A*-site ordered double perovskite is usually oxygen deficient such that the oxygen atom in the *A'* layer is partly or totally lacking. These features are important if one likes to study dimensional features of transition metal oxides; in the case of the single perovskite *A* and *A'* atoms exist randomly, and the oxygen vacancies are also random. The double perovskite structure can be called as the 0112 structure. This naming originates in the concept of homologous series (Fig. 1.1.2), developed for categorizing the structures of high T_c superconductors [1,2]. Together the simple and the double perovskite form the first two members of the $01(n\text{-}1)n$ homologous series. This is reason why our group write an *A*-site ordered double perovskite as "$AA'B_2O_{5+\delta}$", *e.x.* Ba*RE*$Fe_2O_{5+\delta}$, although other groups write it as "$A'AB_2O_{5+\delta}$", *e.x.* *RE*$BaFe_2O_{5+\delta}$.

The first compound of the *A*-site ordered double-perovskite structure was $BaY(Cu_{0.5}Fe_{0.5})_2O_{5+\delta}$ discovered by Er-Rakho *et al.* in 1988 [3]. After this discovery, many other materials with the 0112 structure were found, *e.g.*, Ba*RE*$CuFeO_{5+\delta}$ [4,5], $BaY(Co_{1-x}Cu_x)_2O_{5+\delta}$ [6-8], $BaY(Co_{0.5}Cu_{0.5-x}Fe_x)_2O_{5+\delta}$ [9], *etc.* Concerning the 0112 compounds with the transition metal site (*B*) occupied by only one kind of element, we know the Ba*RE*$Co_2O_{5+\delta}$, Ba*RE*$Mn_2O_{5+\delta}$, and Ba*RE*$Fe_2O_{5+\delta}$ systems.

Ba*RE*$Co_2O_{5+\delta}$ was first reported for *RE* = Y by Zhuo *et al.* [10,11]. In this compound, co-existence of excess-oxygen ordering [10,12-16], charge-ordering [15,17-19], MR [14] and MI transition [14,15,20-22] has been reported. These phenomena are related to the variation

in the spin configuration of Co, *i.e.* high-, low- or intermediate-spin configuration.

The first report on the Ba*RE*$Mn_2O_{5+\delta}$ phase was also for *RE* = Y [23]. For the manganese oxides, single-perovskite type $Ln_{1-x}A_xMnO_3$ phases (Ln: lanthanide, A: alkaline earth) are known to exhibit colossal magnetoresistance (CMR), and spin-, charge- and orbital- ordering [24,25]. Also for the Ba*RE*$Mn_2O_{5+\delta}$ system, these phenomena were reported [26-34].

The 0112 compounds with the transition metal site occupied by Cu only are difficult to synthesize. If it were done, chances are that such compounds would be superconducting. In fact, an early effort to extend the solid solubility of Cu at the transition-metal site in the $BaY(Cu_{0.5+x}Fe_{0.5-x})_2O_{5+\delta}$ system found a narrow solubility region around the optimum of equal amounts of Fe and Cu [35]. So far the highest Cu concentration achieved at the *B* site is 70 %: a single-phase sample of $BaY(Cu_{0.7}Fe_{0.3})_2O_{5+\delta}$ was obtained through high-pressure heat treatment [36].

The *A*-site ordered double-perovskite phase with the *B*-site occupied by iron only, *i.e.* Ba*RE*$Fe_2O_{5+\delta}$ (*RE* = Nd, Sm), was synthesized for the first time by Karen *et al.* in 1999 [37]. In the same year, an interesting phenomenon was discovered in this system [38]. That is a "Verwey-type transition", being akin to the Verwey transition of magnetite (Fe_3O_4).

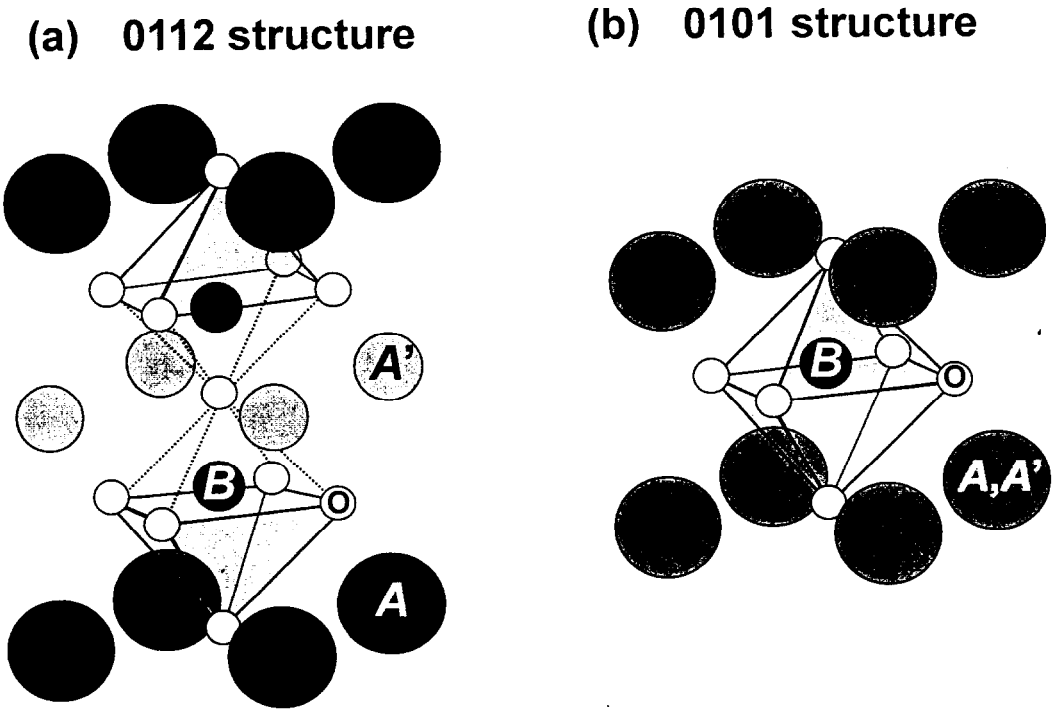

Fig. 1.1.1: A schematic illustration of (a) the *A*-site ordered double perovskite (0112) structure $AA'B_2O_{5+\delta}$, and (b) the single perovskite (0101) structure $(A,A')BO_{3-\delta}$.

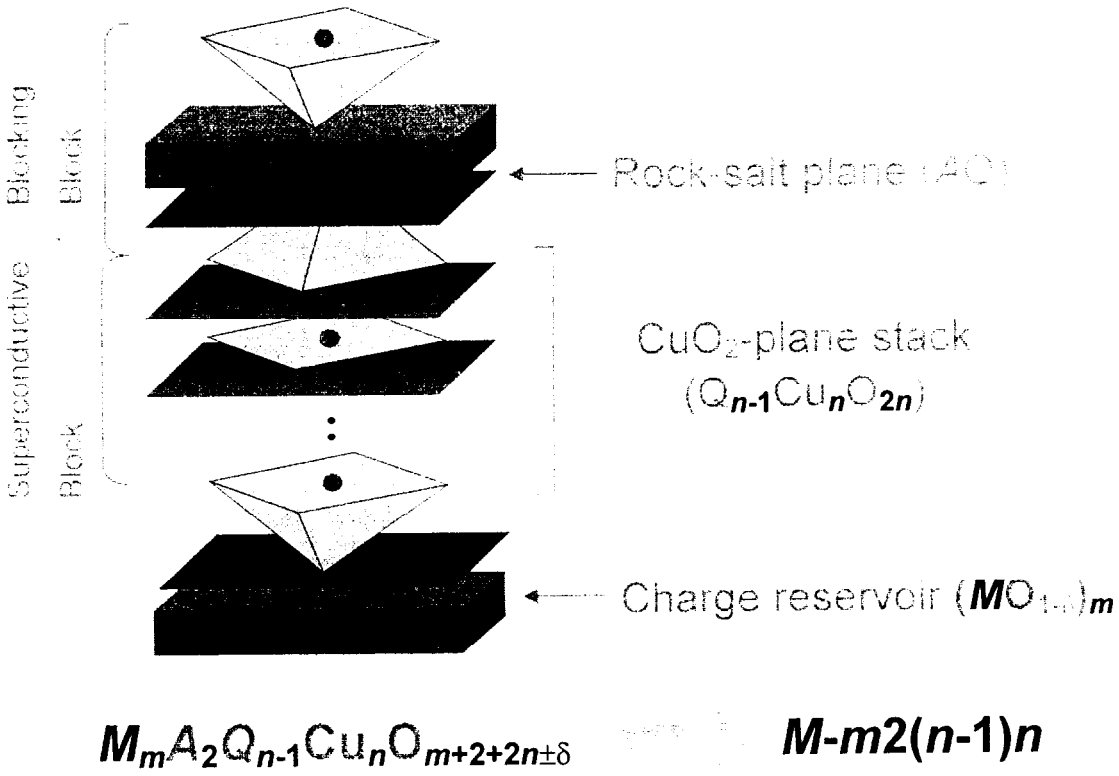

Fig. 1.1.2: Structure of a homologous series (category A) [1,2].

1.1.2 Verwey-Type Transition in Ba*RE*$Fe_2O_{5+\delta}$

In *A*-site ordered double-perovskite, $BaSmFe_2O_{5+\delta}$, a phase transition was observed with Mössbauer spectroscopy [38]. At temperatures lower than the transition temperature two components due to divalent and trivalent iron were seen in the Mössbauer spectrum. On the other hand at higher temperatures than the transition temperature, only single component was seen. Based on the isomer-shift and internal-field values, this component was assigned to iron at the mixed-valence state of 2.5+ (Fig. 1.1.3). The same transition has been observed also in resistivity, susceptibility and heat-capacity data (Fig. 1.1.4). Therefore this transition is very akin to the Verwey transition of magnetite, Fe_3O_4: it may be called as a Verwey-type transition.

In the *A*-site ordered double perovskite system, Ba*RE*$Fe_2O_{5+\delta}$, for $\delta = 0$ *i.e.* Ba*RE*$Fe_2O_{5.0}$, the average valence of Fe is 2.5+. The number of $Fe^{2.5+}$ species in the mixed-valence state

decreases monotonically with increasing amount of excess oxygen, δ, which was also observed in the Mössbauer spectroscopy at 300 K (above the Verwey-type transition temperature, T_V) [38]. On the other hand, the number of six-coordinated (CN = 6) Fe^{III} increases linearly with δ. This means that the Fe^{III} (CN = 6) atoms does not participate in the mixed-valence state, and it is considered that the mixed valence iron species make the coupling between Fe^{II} and Fe^{III} only in five coordination (CN = 5).

So far, the crystal and magnetic structures were studied on a sample of BaREFe$_2$O$_{5+\delta}$ (RE = Nd, Sm, Gd, Tb) by powder neutron, synchrotron x-ray diffraction and Mössbauer spectroscopy [37,39,40,41]. It was shown that at higher temperatures this material is paramagnetic with identical square-pyramidal coordinations at all iron atoms. Upon cooling below T_N (= 450 K), an antiferromagnetic (AFM) spin order appears, being accompanied by a magnetostrictive orthorhombic distortion. At T_V (« T_N) discontinuous increase in distortion occurs. From rietveld refinements, below T_V, the charge ordering between Fe^{II} and Fe^{III} occurs, and the spins have AFM interactions in all three directions (G type) whereas in the mixed valence state a ferromagnetic (FM) interactions appears between the iron atoms facing each other across the RE layer (Fig. 1.1.5).

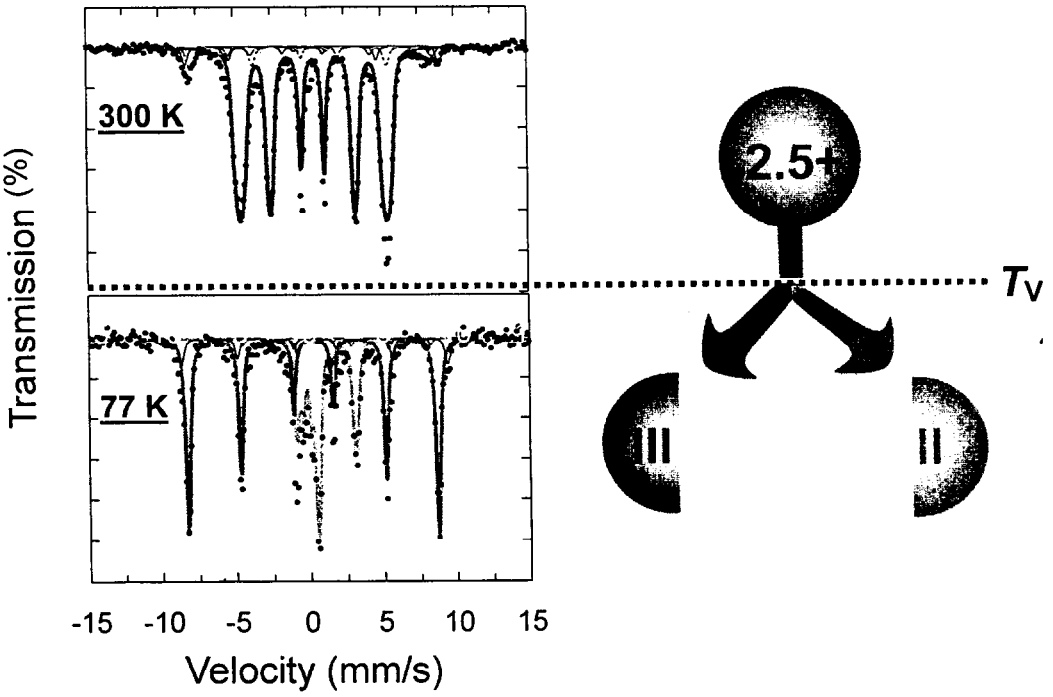

Fig. 1.1.3: ^{57}Fe Mössbauer spectra of BaSmFe$_2$O$_{5+\delta}$ recorded at 300 K and 77 K [28]. The picture of right hand indicates the valence of iron in the sample.

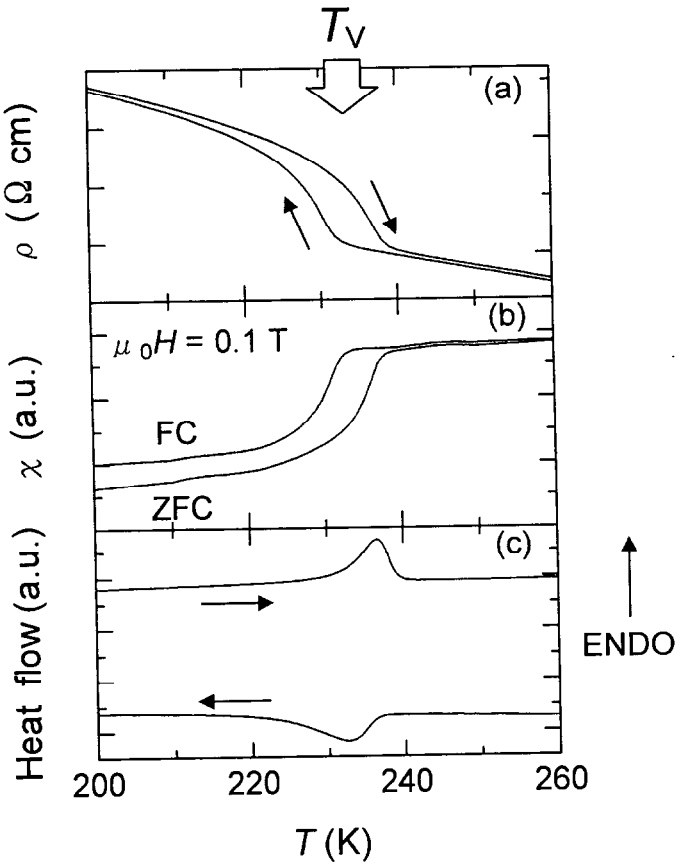

Fig. 1.1.4: (a) Resistivity and MR, (b) magnetic susceptibility and (c) heat flow *vs.* temperature in a $BaSmFe_2O_{5.04}$ sample. T_V indicates the Verwey-type transition temperature.

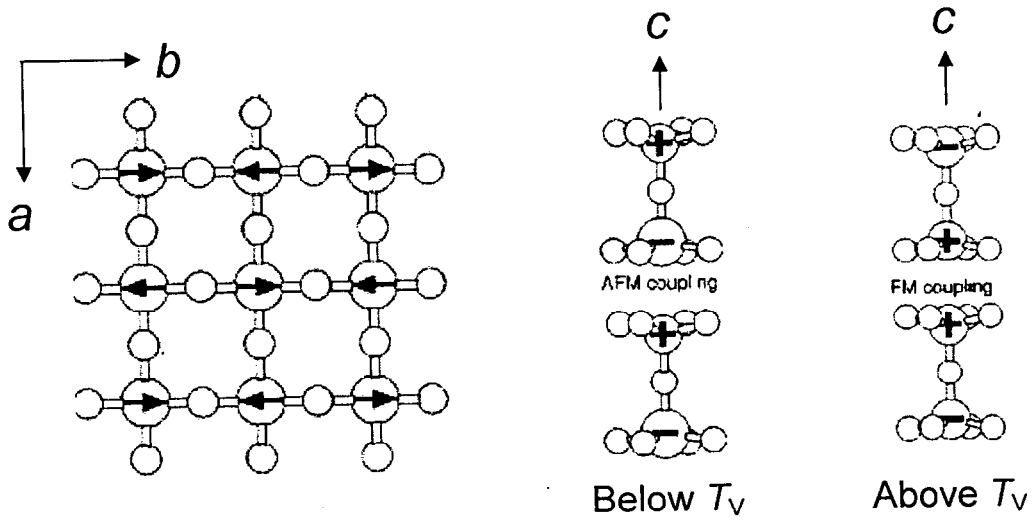

Fig. 1.1.5: Magnetic structure of $BaREFe_2O_{5+\delta}$ (*RE* = Tb, $\delta \approx 0$) as reported by Karen *et al.* [29].

The existence of another transition was reported in this *A*-site ordered double-perovskite iron-oxide systems [39]. It is called as "premonitory" transition, which is at a temperature as high as 30 K above T_V. In the region between the premonitory transition temperature (T_p) and T_V, iron is in two valences, $Fe^{2.5+\varepsilon}$ and $Fe^{2.5-\varepsilon}$, and the lattice maintains its distortion, but the volume increases a little, continuously structurally homogeneously. This premonitory transition can be observed only in the low excess oxygen content region (Fig 1.1.6). It looks that the Verwey-type transition occurs in two steps.

So far this *A*-site ordered double-perovskite iron-oxide systems are studied by only two groups, *i.e.* our group and university of Oslo's group (Karen *et al.*). So this phase have still unknown features yet.

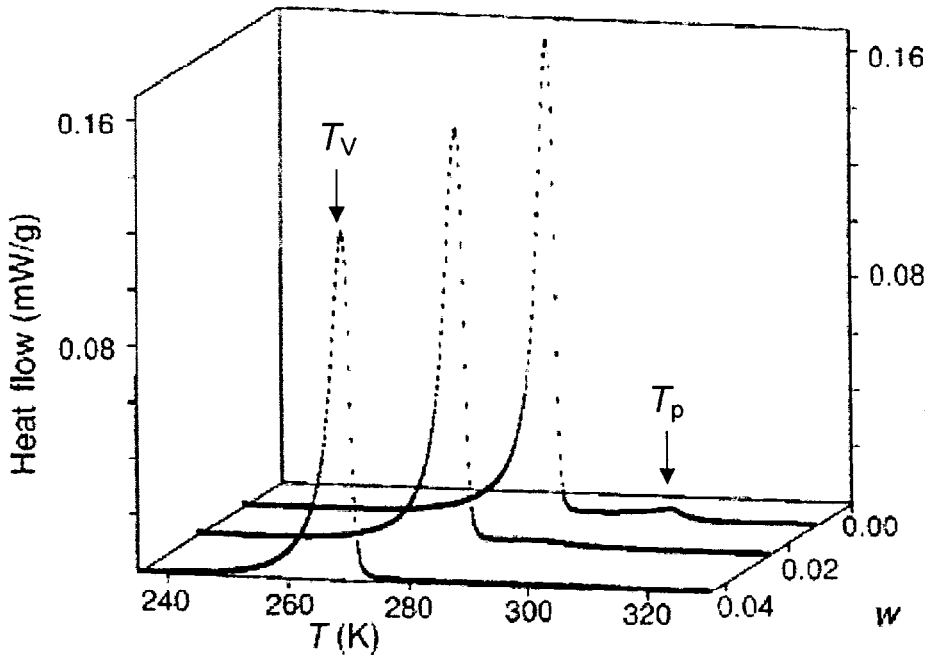

Fig. 1.1.6: Endothermal caloric effects of the Verwey-type transition in $BaTbFe_2O_5$ as seen by DSC upon heating [39]. The big and small jumps correspond with Verwey-type transition and premonitory transition, respectively.

1.1.3 Single-Perovskite Iron-Oxides

Single-perovskite iron-oxides are one of related system of *A*-site ordered double-perovskite iron-oxides. In the single-perovskite iron oxides, *e.g.* $CaFeO_3$, $RE_{1-x}Sr_xFeO_3$ *etc.*, as it is well known, the charge disproportionation (CD) phenomenon; $2Fe^{IV}$ (higher temperature) $\leftrightarrow$ Fe^{III} + Fe^{II} (lower temperature) occurs [42-46]. At lower temperatures, especially in $RE_{1/3}Sr_{2/3}FeO_3$, the charge ordering has been found [47-51]. Layers of nominal Fe^{III} and Fe^{V} species are ordered in the sequence ...533533... along the pseudocubic [111]*c* direction or along the rhombohedral *z* direction (Fig. 1.1.7). *RE* and Sr ions are distributed in a disordered way in the *A*-site. The rhombohedral lattice distortion increased as the *RE* ionic radius decreased in $RE_{1/3}Sr_{2/3}FeO_3$ [52]. This leads to a decrease in hybridization between O 2p and Fe 3d states or in the one-electron bandwidth (W), and other data, *e.g.* resistivity change (Fig. 1.1.8) *etc*, indicate that the charge ordering (CO) stability is rather decreased with decreasing *RE* ionic radius or p-d hybridization effect.

In this single-perovskite system, oxygen deficiency also has an important role [53,54]. Ordering of oxygen vacancies has not been reported, which means oxygen is in disorder. In the single-perovskite iron oxides, negative magnetoresistance was observed in the temperature regime where the CD/CO transition takes place [I].

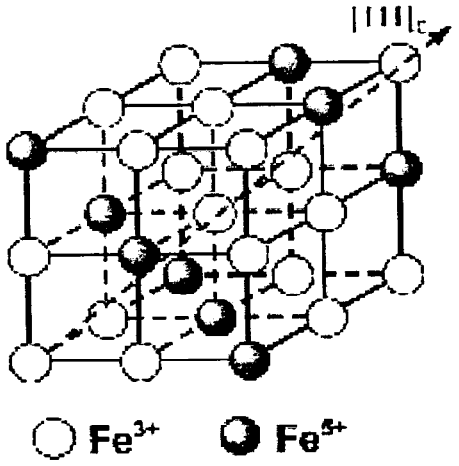

Fig. 1.1.7: The charge ordering in the single perovskite iron oxide, $Nd_{1/3}Sr_{2/3}FeO_3$ [52].

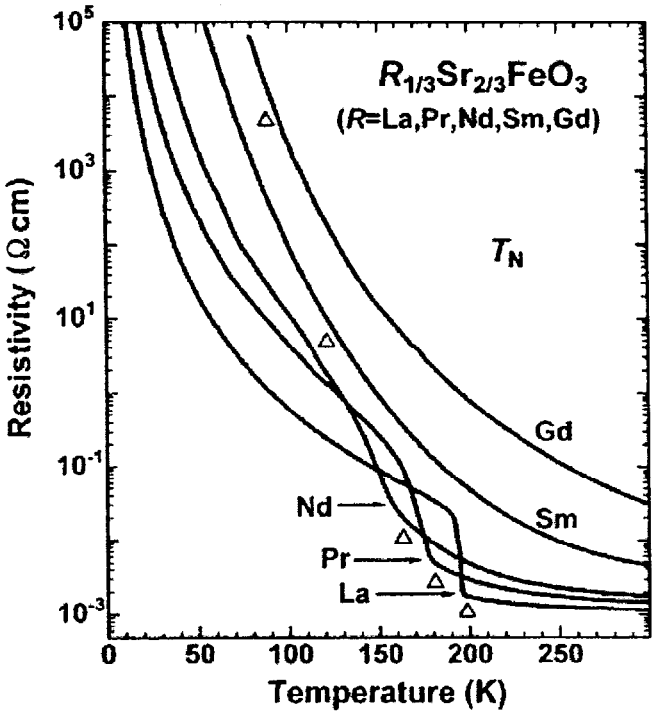

Fig. 1.1.8: Temperature dependence of resistivity for $R_{1/3}Sr_{2/3}FeO_3$ system in a cooling process. Open triangles indicate the critical temperature (T_N) for the antiferromagnetic phase transition [52].

1.1.4 Verwey transition in Magnetite (Fe_3O_4)

An *A*-site ordered double-perovskite Ba*RE*$Fe_2O_{5+\delta}$ system shows the Verwey-type transition, which has been mentioned before, and this naming originates in magnetite. Magnetite (Fe_3O_4) is the oldest known magnetic material. It is a ferrimagnet with a Néel temperature of 851 K, and has an inverse spinel structure. Iron atoms are located in two nonequivalent positions in the unit cell, *i.e.* 8 tetrahedral *A* sites are occupied by Fe^{III} and 16 octahedral *B* sites by equal numbers of Fe^{II} and Fe^{III} (Fig. 1.1.9). Below 851 K, magnetite is ferrimagnetic with *A*-sites moments aligned antiparallel to the *B*-site moments. A rapid electron hopping between Fe^{II} and Fe^{III} ions takes place among *B* sites, such that the sites are structurally and spectroscopically equivalent.

Verwey [55] discovered that magnetite undergoes a sharp, first order transition on cooling down to below ~ 125 K at which the resistivity increases sharply by 2 orders of magnitudes (Fig. 1.1.10 [36]), and the structure distorts from cubic symmetry [57]. This was explained by a charge ordering (CO) of Fe^{II} and Fe^{III} on the *B* sites in alternating layers, although this was not confirmed despite the large number of previous studies. Magnetite was the first material in which a charge ordering transition was proposed to explain the metal insulator transition [55]. However it should be noted that the physical origin of this phase transition and electronic state of the iron atoms in both phases are not well understood [58]. For the charge ordering problem, there are many studies as follows. Mössbauer spectra demonstrate that localized Fe^{II} and Fe^{III} are present at the octahedral sites, and a recent study resolved two environments for each cation in addition to the tetrahedral Fe^{III} signal [59]. The low temperature structure is a rhombohedral distortion of the cubic spinel arrangement to the first approximation [60] but this splits the *B* sites in a 3:1 ratio and so is not consistent with the expected CO. Neutron [61] and x-ray [62] diffraction studies of single crystals and electron microscopy [63] have shown that the low temperature structure has a monoclinic $\sqrt{2}\,a \times \sqrt{2}\,a \times 2a$ supercell (a is the cell parameter of the undistorted cubic phase) with *Cc* space group symmetry, containing 8 unique *A* sites and 16 unique *B*-sites for cations. A recent ^{57}Fe NMR study [64] has resolved the 8 tetrahedral and 15 of the 16 octahedral iron environments. The only published refinement of the low temperature superstructure of magnetite was based on a single crystal neutron diffraction experiment at 10 K by Iizumi *et al.* [65]. An $a/\sqrt{2} \times a/\sqrt{2} \times 2a$ subcell was used with additional *Pmca* or $Pmc2_1$ orthorhombic symmetry constraints to reduce the complexity of the model. Although some differences between the inequivalent *B* sites were found, these were not concluded to be significant evidence for CO. A recent resonant x-ray diffraction study also reported no evidence for charge disproportionation [66]. And also hiigh-pressure effects have been reported [67-71], and then recently magnetite showed metal behavior under high-pressure like a 8 GPa [72].

Thus, the arguments for magnetite still continue.

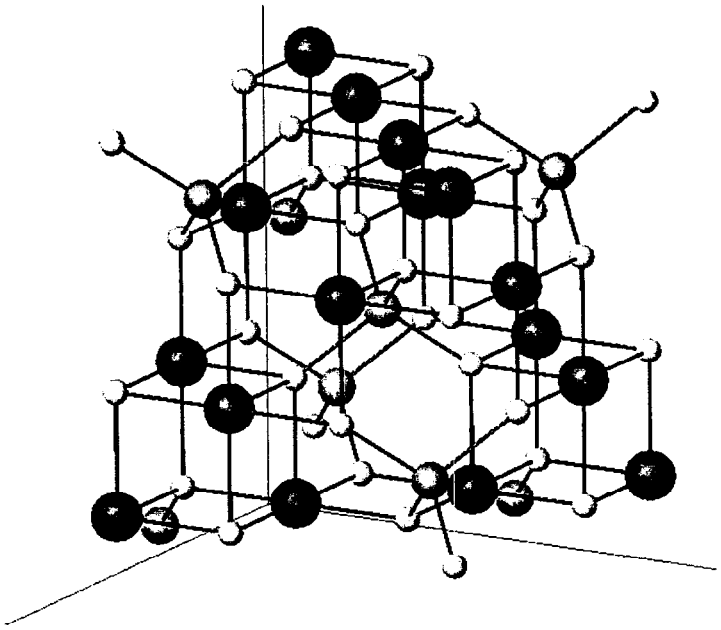

Fig. 1.1.9: The inverse spinel structure. *A* sites, *B* sites and oxygen atoms are represented by silver, black and white sphere, respectively.

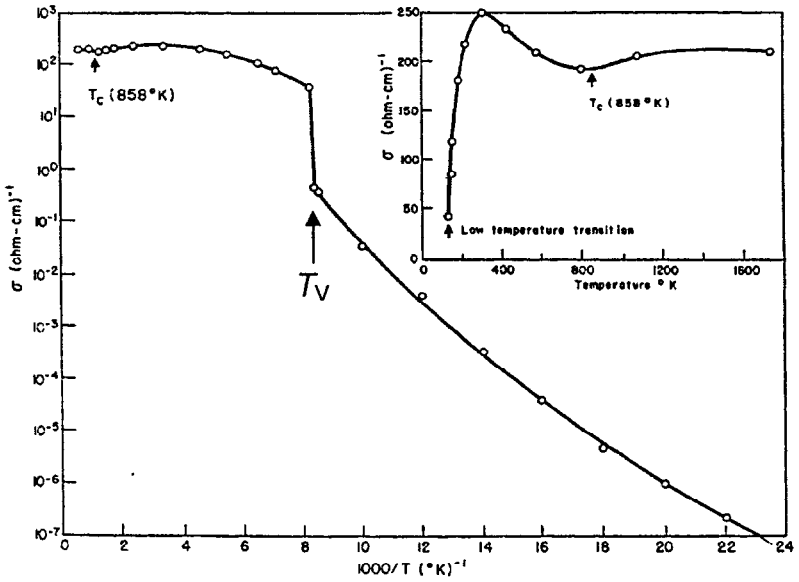

Fig. 1.1.10: Temperature dependence on the dc conductivity of the magnetite single crystal [56].

Furthermore magnetite is predicted as a half-metallic material [73-78], in which one spin direction is metallic while another spin is semiconducting. This character was first postulated by DeGroot *et al.* [79] in 1983 based on theoretical band-structure calculations of the ferromagnetic Heusler alloy NiMnSb. So far in addition to magnetite and Heusler alloys (*e.g.* NiMnSb, PtMnSb [80]), limited number of oxides, *i.e.* $La_{1-x}Ca_xMnO_3$ [81-83], $La_{1-x}Sr_xMnO_3$ [82], CrO_2 [84,85], and Sr_2FeMoO_6 [86], have been confirmed to be half metallic. Here in the iron oxide Sr_2FeMoO_6 the mixed valence state $Fe^{2.5+}$ was reported [87], and it seems to be interesting to investigate that the relationship between the mixed valence state and half-metallic properties. The band calculation for the magnetite shows a minority-spin band at the Fermi energy consisting of t_{2g} orbitals on the Fe (*B*-site) sublattice (Fig. 1.1.11) [73].

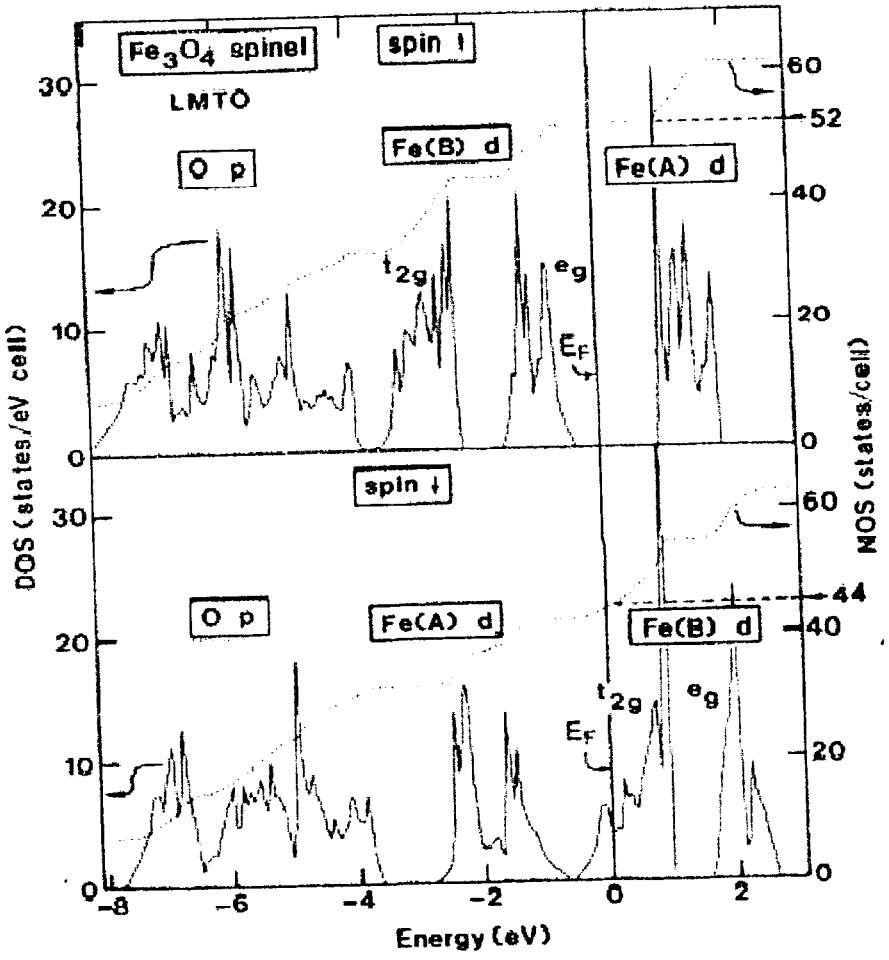

Fig. 1.1.11: Spin-projected one-electron densities and numbers of states for magnetite [73]. The calculation predicts a net magnetic moment of 8.0 μ_B per unit cell which consists of two formula units.

1.2 Objectives of the Present Work

Various "super-functions" of the transition-metal oxides including colossal magnetoresistance and high-T_c superconductivity, having their origins in the strong electron correlation, have intensively been studied. Still there exist possibilities that unknown super-functions would be discovered among such materials. With this anticipation/hope in mind, to search for new materials is worthwhile.

Recently samples of *A*-site ordered double-perovskite, Ba*RE*$Fe_2O_{5+\delta}$, were successfully synthesized [27] and Verwey-type transitions were observed [28]. Since the 0112 structure of *A*-site ordered double perovskites is of the simplest layered transition-metal oxide, it is one of the key structures for understanding the functional properties of strongly-correlated-electron transition-metal oxides. For Ba*RE*$Co_2O_{5+\delta}$ and Ba*RE*$Mn_2O_{5+\delta}$, many interesting research results have been reported, while, for Ba*RE*$Fe_2O_{5+\delta}$, only a limited number of studies have been reported yet.

The original Verwey transition in magnetite (Fe_3O_4) involves the phase transition from a mixed-valence state ($Fe^{2.5+}$) to coexistence of Fe^{II} and Fe^{III}. Magnetite of the inverse spinel structure has only limited sites for cation and/or anion substitutions as compared with the *A*-site ordered double-perovskite structure, this hinders us from studying element substitution effects in Fe_3O_4. The purpose of the present research is to investigate and control the valence mixing-separation transition, the magnetic and magnetotransport properties in the *A*-site ordered double-perovskite (Ba,Sr)(*RE*,Ca)$Fe_2O_{5+\delta}$ system in terms of the chemical substitution/doping effects, and examine the possibility of appearance of novel functions.

Chapter 2. Experimental

2.1 Sample Synthesis

Polycrystalline samples of Ba*RE*$Fe_2O_{5+\delta}$ (*RE* = Ho, Y, Dy, Tb, Eu, Sm, Nd, La), $Ba(Sm_{1-x}Ca_x)Fe_2O_{5+\delta}$ ($0 \leq x \leq 0.1$) and $(Ba_{1-y}Sr_y)SmFe_2O_{5+\delta}$ ($0 \leq y \leq 0.15$) were prepared from high-purity powder mixtures of $BaCO_3$, $SrCO_3$, RE_2O_3 (*RE* = Ho, Y, Dy, Tb, Eu, Sm, Nd, La), $CaCO_3$ and Fe_2O_3. Prior to sample synthesis RE_2O_3 powders were fired at 1000 °C for 10 h in air to get rid of hydroxide contamination. Tb_2O_3 was obtained from Tb_4O_7 after firing at 950 °C for 20 h in a 5 % H_2/Ar gas mixture. (Tb_4O_7 could not be used as a starting material as commercial powder contained oxide impurities.)

The actual synthesis was carried out by means of an oxygen-getter-controlled low-O_2-pressure encapsulation method developed during the course of this research. Stoichiometric mixtures of the starting materials were calcined at 900 °C for 15 h in air. The calcined powder samples were first pelletized, and then sintered as encapsulated in an evacuated fused-silica tube together with Fe metal grains (Fig. 2.1.1). The role of the Fe metal grains was to act as a getter of oxygen. The sintering was carried out at 985 °C for 40 h. At this temperature, the oxygen partial pressure is expected to equilibrate at 7.6×10^{-16} atm due to the redox couple of Fe/FeO [88,II] (see Chapter 3). After sintering, the sample in a fused-silica tube was cooled in air down to room temperature in about 30 minutes.

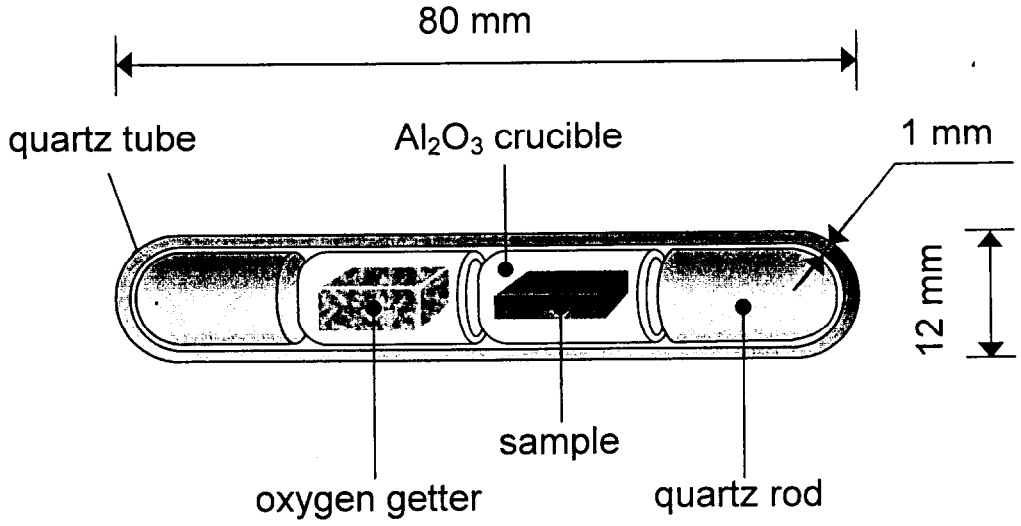

Fig. 2.1.1: Cross-section of the ampoule used for the encapsulation synthesis.

2.2 Control of Excess Oxygen Amount

Using a thermobalance (TG/DTA 2000S, BRUKER axs, and Pyris 1 TGA, PerkinElmer), the amount of excess oxygen in the samples was controlled by means of post-annealing. In the case of annealing in a reduced atmosphere, the sample was annealed for 20 – 30 h in a flowing 5 % H_2/Ar gas mixture at 500 – 650 °C. In the case of annealing in oxygen atmosphere, the sample was annealed for 20 – 30 h in a flowing 0.1 % O_2/Ar gas mixture at 900 °C with taking care of avoiding the decomposition, which was found to easily occur in an oxidized atmosphere.

2.3 Characterization

2.3.1 Determination of Excess Oxygen Amount

The oxygen content of the samples was determined by cerimetric titration, which has been used to determine the oxygen content in perovskite-type iron oxides [37,38,89,90]. A powdered sample of about 30 mg was dissolved under an Ar atmosphere in about 100 ml of 3 M HCl containing about 30 mg of $FeCl_2 \cdot 4H_2O$. The dissolution (aided with temperature around 60 °C) lasted for about 15 min. The resulting solution was titrated at room temperature under an Ar atmosphere with one drop of ferroin as an indicator. First of all the reaction (1) occurs in solution. The excess of Fe^{2+} was titrated with about 0.01 M cerium sulphate solution, in where the reaction (2) occurs, and the endpoint was detected as the orange color of the solution turned green. Each determination was performed in duplicate or triplicate. The excess oxygen content δ was calculated from the titration results using Eq. (3). In this calculation, the concentration of cerium sulphate solution c and the correction coefficient f were calculated using Eqs. (4) and (5). The estimated standard deviation of the δ value was less than 0.005.

• **Reactions**

$$\begin{cases} Fe^{IV} + Fe^{2+} \rightarrow 2Fe^{3+} & (1) \\ Fe^{II} + Ce^{4+} \rightarrow Fe^{3+} + Ce^{3+} & (2) \end{cases}$$

• **Excess oxygen δ**

$$\delta = \frac{\left(\frac{m_{FeCl_2 \cdot 4H_2O}}{M_{FeCl_2 \cdot 4H_2O}} \cdot f - c \cdot V\right) \cdot M_{sample}(\delta = 0) + m_{sample}}{2 \cdot m_{sample} + \left(c \cdot V - \frac{m_{FeCl_2 \cdot 4H_2O}}{M_{FeCl_2 \cdot 4H_2O}} \cdot f\right) \cdot M(O)} \quad (3)$$

c : concentration of cerium sulphate solution

V (ℓ) : amount of titrated cerium sulphate solution

$M_{FeCl_2 \cdot 4H_2O}$: molecular weight of $FeCl_2 \cdot 4H_2O$

$m_{FeCl_2 \cdot 4H_2O}$ (g) : weight of $FeCl_2 \cdot 4H_2O$

$M_{sample}(\delta = 0)$: molecular weight of sample at $\delta = 0$

m_{sample} (g) : weight of sample

M(O) : atomic weight of oxygen

f : the correction coefficient f of $FeCl_2 \cdot 4H_2O$

• **Concentration of cerium sulphate solution, *c***

$$c\,(Ce(SO_4)_2) = \frac{m(Fe(NH_4)_2(SO_4)_2 \cdot 6H_2O)}{M(Fe(NH_4)_2(SO_4)_2 \cdot 6H_2O) \cdot V(Ce(SO_4)_2)} \quad (4)$$

M : molecular weight of $Fe(NH_4)_2(SO_4)_2 \cdot 6H_2O$

m (g) : weight of $Fe(NH_4)_2(SO_4)_2 \cdot 6H_2O$

V (ℓ) : amount of titrated cerium sulphate solution

• **The correction coefficient *f* of $FeCl_2 \cdot 4H_2O$**

$$f = \frac{c(Ce(SO_4)_2) \cdot V(Ce(SO_4)_2) \cdot M(FeCl_2 \cdot 4H_2O)}{m(FeCl_2 \cdot 4H_2O)} \quad (5)$$

c : concentration of cerium sulphate solution

V (ℓ) : amount of titrated cerium sulphate solution

M : molecular weight of $FeCl_2 \cdot 4H_2O$

m (g) : weight of $FeCl_2 \cdot 4H_2O$

2.3.2 Determination of Phase Purity and Unit-Cell Parameters

The phase purity and unit-cell parameters were evaluated based on conventional x-ray powder diffraction (XRD) measurements carried out with Cu *Kα* radiation (M18XHF, BRUKER axs). The powder was set on a "non-reflection" holder of silicon single crystal. Typical experimental parameters for the measurement were as follows: operating power: 45 kV × 200 mA, scanning range: 3 – 120 ° (2θ), sampling width: 0.02 ° (2θ), scanning rate: 5 ° /min, at room temperature (20 – 30 °C). Phases included in the samples were usually identified using JCPDS (Joint Committee on Powder Diffraction Standards) cards.

2.3.3 Precise Studies of the Structures

The precise structures and atomic positions were studied by synchrotron x-ray powder diffraction (SXRD). The bulk sample was crashed and ground in an agate mortal with ethanol. The powder was put into ethanol and stirred. After 5 minutes, a supernatant fluid was taken by the syringe with leaving a sunken thing. The supernatant fluid was stirred once more, then after 45 minutes, the supernatant part was sucked up with syringe. Thus, by evaporating ethanol, a very fine powder with uniform particle size was obtained. The powder was put into a quartz capillary of 0.1 mm inside diameter. Data were collected at SPring-8, Japan (beam line: BL02B2). High-energy x rays with wavelength λ = 0.5 Å were used. The wavelength of the incident x rays was confirmed using standard CeO_2. The diffraction patterns of the samples were recorded on an imaging plate. The measurements were carried out in the temperature range of 100 – 350 K. Scans were done up to 75 ° in 2θ with the step size of 0.01 °. The diffraction data were analyzed by the Rietveld refinements with RIETAN-2000 program.

2.3.4 Differential Scanning Calorimetry (DSC)

A liquid-nitrogen operated differential scanning calorimeter (Pyris 1 DSC, PerkinElmer) was used to register thermal flux curves upon heating and cooling at a rate of 20 K/min between 100 K and 400 K. For the measurement a powdered sample (10 – 50 mg) was sealed in an aluminum pan. The calibration was performed by using the melting of In.

2.3.5 Magnetic Property Measurements

Magnetic property measurements were performed by a dc SQUID magnetometer (MPMS-XL5, Quantum Design). Temperature *vs.* magnetic susceptibility of all samples were measured in both zero-field-cooled (ZFC) and field-cooled (FC) modes in a constant applied field. Magnetization curves were obtained under an applied field up to 5 T. These data were collected in temperature range from 5 to 400 K. For sample preparation a small bulk sample (about 20 – 100 mg) was sealed in a gelatin capsule with cotton, and the capsule was attached to a straw.

2.3.6 Electrical Transport Property Measurements

Electrical transport property measurements were performed by Physical Property Measurement System (PPMS-9, Quantum Design). Here a standard four-probe technique was used in the temperature range from 5 to 400 K. The pellets were shaped into parallel with a cross-section of 2 – 3 mm^2. Au paste (TR-1301, Tanaka Kikinzoku Hanbai K.K.) was put on the sample surface, then heated at 750 °C for 15 min in a 5 % H_2/Ar gas mixture. As an electrode, Au wire (ϕ: 0.05 mm), which was fixed by Ag paste (4922N, DUPONT) was used.

Magnetotransport property measurements were performed under an applied field of -7 to 7 T, in a direction perpendicular to the current flow, in the temperature range of 5 to 400 K. The samples were measured in both a field-scanning mode (at constant temperature) and a temperature scanning mode (at a constant external field).

2.3.7 TEM Observation

Electron diffraction (ED) and high-resolution transmission electron microscopic (HRTEM) studies were performed by transmission electron microscope (TEM) operating at 300 kV (H-9000, Hitachi). A specimen was prepared by a conventional crushing method, *i.e.*, the sample was crushed in an agate mortar and dispersed into ethanol or CCl_4, then one drop of that liquid was dripped on a Cu grid coated with carbon support films. ED studies were also performed in Matsui group at National Institute for Materials Science (NIMS) as a function of temperature.

2.3.8 Mössbauer Spectroscopy

^{57}Fe Mössbauer spectra of the samples were recorded at fixed temperatures in the temperature range 5 – 300 K in transmission geometry at Helsinki University of Technology, or at Åbo Akademi University in Finland. The absorbers were made by spreading the sample material mixed with varnish evenly on an Al foil. The thickness of the sample material (expressed in mass per area) was approximately 20 mg/cm^2. A linear Doppler velocity sweeping from – 15 to + 15 mm/s was used. An Amersham ^{57}Co:Rh (20 mCi, December 1998) source was used for producing the Mössbauer γ quanta, during the time interval of May 2000 – January 2001. All spectra exhibited magnetic splitting and were thus fitted with the full Hamiltonian of combined electric and magnetic interaction. The following hyperfine parameters were included in the fit: the internal magnetic field experienced by the Fe nucleus (B), the chemical isomer shift relative to α-Fe (δ), the quadrupole coupling constant (eQV_{zz}), the resonance line widths (Γ), and the relative intensities of the components (I). The following conditions and constraints were applied:

(i) For each component a certain variation in the parameter B was allowed in order to simulate the fact that the internal fields have a certain spread due to, *e.g.*, local distortions of the coordination polyhedra. A Gaussian distribution was assumed and its width (ΔB) was introduced as a fit parameter.

(ii) The asymmetry parameter η and the angle θ between the direction of the magnetic and the electric quantization axes were omitted in most fittings (set equal to zero).

(iii) All components were constrained to have equal line widths Γ.

(iv) A small asymmetric quadrupole component, originating from traces of iron in the Be detector window and in the Al foil was kept fixed during the fits. These impurity defects cover less than ~ 2 % of the spectral intensity obtained in the measurements.

2.3.9 SEM Observation

Microstructure, especially grain size was observed by means of a field emission scanning electron microscope (FE-SEM) operating at 15 kV (S-4500, Hitachi). The clucked surface of the bulk samples were coated by sputtering of Pt-Pd.

2.3.10 Band Structure Calculation

The density of state (DOS) for the up- and down-spin state of $BaYFe_2O_{5.0}$ was calculated by Hamada *et al.* in Tokyo University of Science. The electronic structure had been calculated with the full-potential linearized augmented plane-wave (FLAPW) method within the LDA + U scheme with the effective U parameters of 2 eV for Fe. The structural data was based on the tetragonal phase, and the atomic positions were referred to $BaTbFe_2O_{5+\delta}$ ($\delta \approx 0$), which ware obtained from neutron scattering data reported by Karen *et al.* [39].

Chapter 3. New Synthesis Technique for (Ba,Sr)(*RE*,Ca)$Fe_2O_{5+\delta}$

3.1 Encapsulation Technique with Oxygen Getter

The sample synthesis was carried out by means of an oxygen-getter-controlled low-O_2-pressure encapsulation method developed during the course of this research (Fig. 3.1.1). The details about the encapsulation method are written in Chapter 2. In this synthesis technique, equilibrium of the redox couple is utilized (Fig. 3.1.2). For the *A*-site ordered double-perovskite (Ba,Sr)(*RE*,Ca)$Fe_2O_{5+\delta}$ samples which was used in this study, the reaction of Fe/FeO [88,II] was utilized, and the oxygen partial pressure was expected to equilibrate at 7.6×10^{-16} atm at 985 °C, at which the sample was synthesized.

On the other hand, Karen *et al.* synthesized the master sample from a nanoprecursor obtained by liquid mixing in a citrate melt [37-41], and after calcinations and homogenization, the cold-pressed powder was sintered under a reduced condition, *i.e.* in an atmosphere of Ar and H_2 saturated by water vapor. Summarizing their sintering conditions, those are in a hatched region in Fig. 3.1.2. This mean that both of conditions, our conditions and the conditions by Karen *et al.*, are suitable to synthesize the *A*-site ordered double-perovskite iron oxides.

However the synthesis technique of Karen *et al.* seems to be complex. On the other hand, one of the merits of our technique, *i.e.* an oxygen-getter-controlled low-O_2-pressure encapsulation method, is that "it is simple". Further more it is easy to control a reduced atmosphere in good accuracy. Actually "oxygen getter" has been used when the sample is reduced, but it may be first time to apply to the sample synthesis of such oxides.

This synthesis technique also can be applied to other sample synthesis. An example is shown in next part. Or otherwise so far this oxygen-getter-controlled low-O_2-pressure encapsulation method has been applied to the *B*-site ordered double-perovskite Sr_2FeMoO_6 [87,III,IV,103-106], and very recently also to *A*-site ordered double-perovskite $BaYMn_2O_{5+\delta}$ by using equilibrate of FeO/Fe_3O_4.

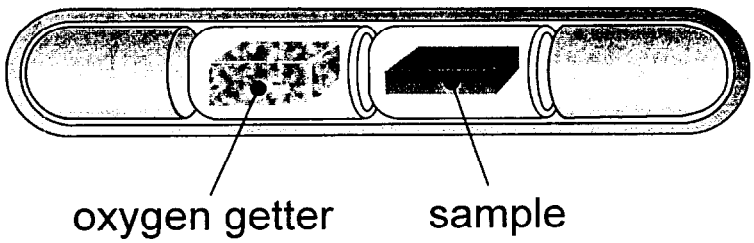

Fig. 3.1.1: Cross-section of the ampoule used for the encapsulation method.

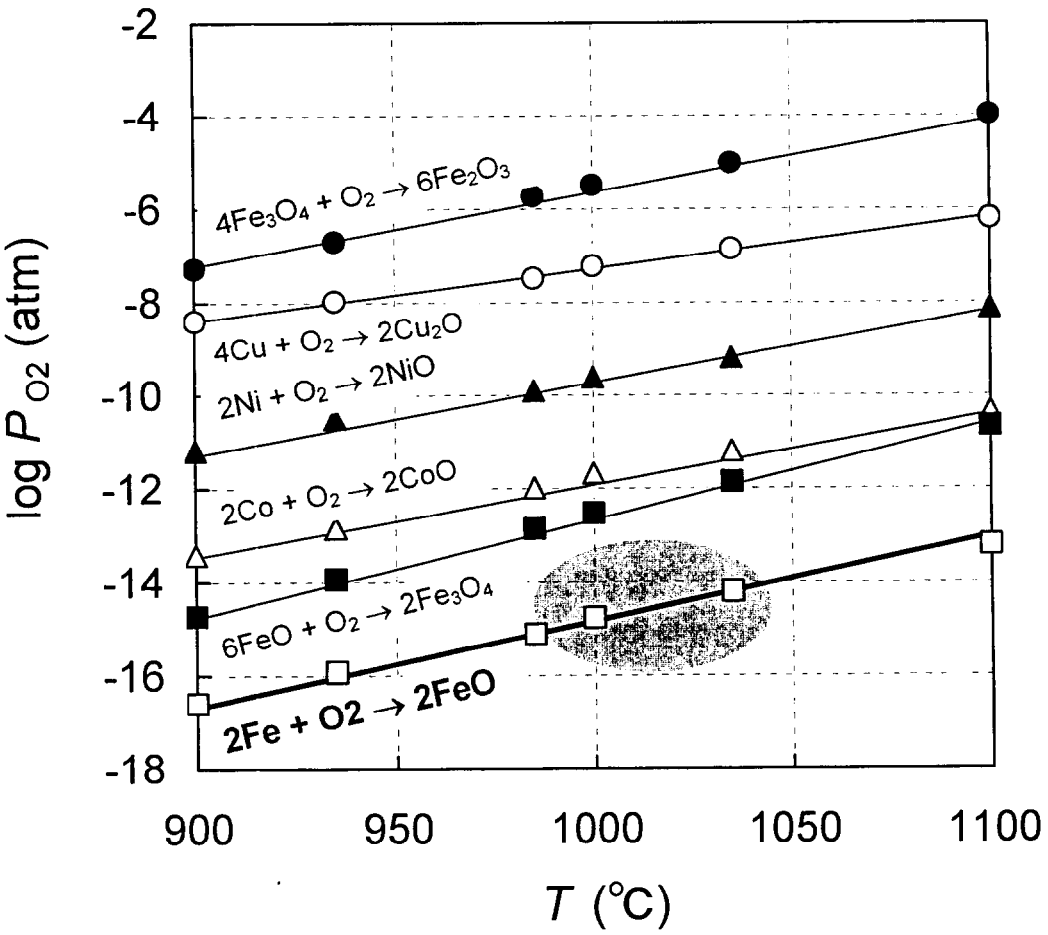

Fig. 3.1.2: Oxygen partial pressure *vs.* temperature for the different iron oxide redox couples [59]. The lines indicate the equilibrium which is shown by the formula. The hatched region is indicating the synthesis conditions of Karen *et al.* [37-41].

There is one good example which is showing the validity of this encapsulation technique with oxygen getter. Fig. 3.1.3 (a) is the XRD pattern of commercial magnetite (Fe_3O_4) powder, which is including some wüstite (FeO). If we want to get rid of this FeO from the commercial Fe_3O_4, or to synthesize a single-phase Fe_3O_4, what we should do. To obtain a single-phase Fe_3O_4, three trials were performed. Those are written below, and it is summarized in Table 3. 1.1.

Table. 3.1.1: Starting material and oxygen getter for Case 1, 2 and 3. The methods used at synthesis are written as a comment.

	Starting material	**Oxygen getter**	**Comment**
Case 1	Commertial Fe_3O_4	–	in Ar flow
Case 2	Fe_2O_3	Cu/Cu_2O	encupusulation technique
Case 3	Commercail Fe_3O_4	Co/CoO	encupusulation technique

Case 1. Sintering in Ar flow

Fig. 3.1.4 is a phase diagram of Fe – O [91-95]. The single-phase Fe_3O_4 is in the hatched region in the figure. So if the sintering is performed in this condition, the single-phase Fe_3O_4 can be obtained. So the commercial Fe_3O_4 powder was pelletized and sintered at 1200 °C for 15 hours in Ar flow and quenched in air. The XRD pattern of the product is shown in Fig. 3.1.3 (b). The phase is confirmed as hematite (Fe_2O_3). Actually the region for single-phase Fe_3O_4 is narrow in the phase diagram (Fig. 3.1.4), so it is difficult to control an atmosphere using like this way.

Case 2. Sintering with Cu/Cu_2O as oxygen getter

Using the encapsulation technique with Cu/Cu_2O as oxygen getter, the pelletized Fe_2O_3, which was starting material, was sintered at 1000 °C for 15 hours, and quenched. At the sintering condition, the reactions (1) and (2) are expected in the ampoule.

$$6Fe_2O_3 \rightarrow 4\mathbf{Fe_3O_4} + O_2 \qquad (1)$$

$$4\,Cu + O_2 \rightarrow 2Cu_2O \quad \text{(oxygen getter)} \qquad (2)$$

The XRD pattern of the product is shown in Fig. 3.1.3 (c). The phase is confirmed as two phases, *i.e.* Fe_2O_3 and Fe_3O_4. The Cu/Cu_2O oxygen getter is not enough to product the Fe_3O_4 from Fe_2O_3.

Case 3. Sintering with Co/CoO as oxygen getter at 1000 °C for 15 h with CoO and Co as an oxygen getter

Using the encapsulation technique with Co/CoO as oxygen getter, the pelletized commercial Fe_3O_4, which was starting material, was sintered at 1000 °C for 15 hours, and quenched. At the sintering condition, the reactions (3) and (4) are expected in the ampoule.

$$6FeO + O_2 \rightarrow 2\mathbf{Fe_3O_4} \quad (3)$$

$$2Co + O_2 \rightarrow 2CoO \quad \text{(oxygen getter)} \quad (4)$$

The concept is as below. The commercial Fe_3O_4 is including some FeO, as mentioned before, and the FeO gets the oxygen from CoO, then that becomes Fe_3O_4. After all the FeO become Fe_3O_4, the oxygen-partial pressure is expected to equilibrate at Co/CoO line. In other word, the Fe_3O_4 does not become Fe_2O_3 because of the "block" by Co/CoO line. Actually the product was the single-phase Fe_3O_4 (Fig. 3.1.3 (d)).

The conductivity of this single-phase Fe_3O_4 is shown in Fig. 3.1.5. Verwey transition temperature (T_V) is 122 K in the cooling process. The transition is quite sharp and a magnitude of the jump is of about two orders.

The Mössbauer spectra of this Fe_3O_4 at 150 K (above T_V) are shown in Fig. 3.1.6. Above T_V the intensities are very close to theoretical values, *i.e.* Fe^{III} (*A* site) is 35.3(3) % and $Fe^{2.5+}$ (*B* site) is 64.7(7) % (Table. 3.1.2). Isomer shift of $Fe^{2.5+}$ is between that of Fe^{II} and Fe^{III}. Furthermore, Field is lower than for high-spin Fe^{III} and eQVzz is zero (typical for valence mixing). Below T_V, the situation is complicated as several components emerge, but they are charge separated into Fe^{II} and Fe^{III}.

These data are indicating that the Fe_3O_4 obtained by encapsulation technique with oxygen getter is a good sample. It should be also noted that it is available to quench in a reduced atmosphere. As you can see above, this encapsulation technique with oxygen getter is quite useful for such oxides.

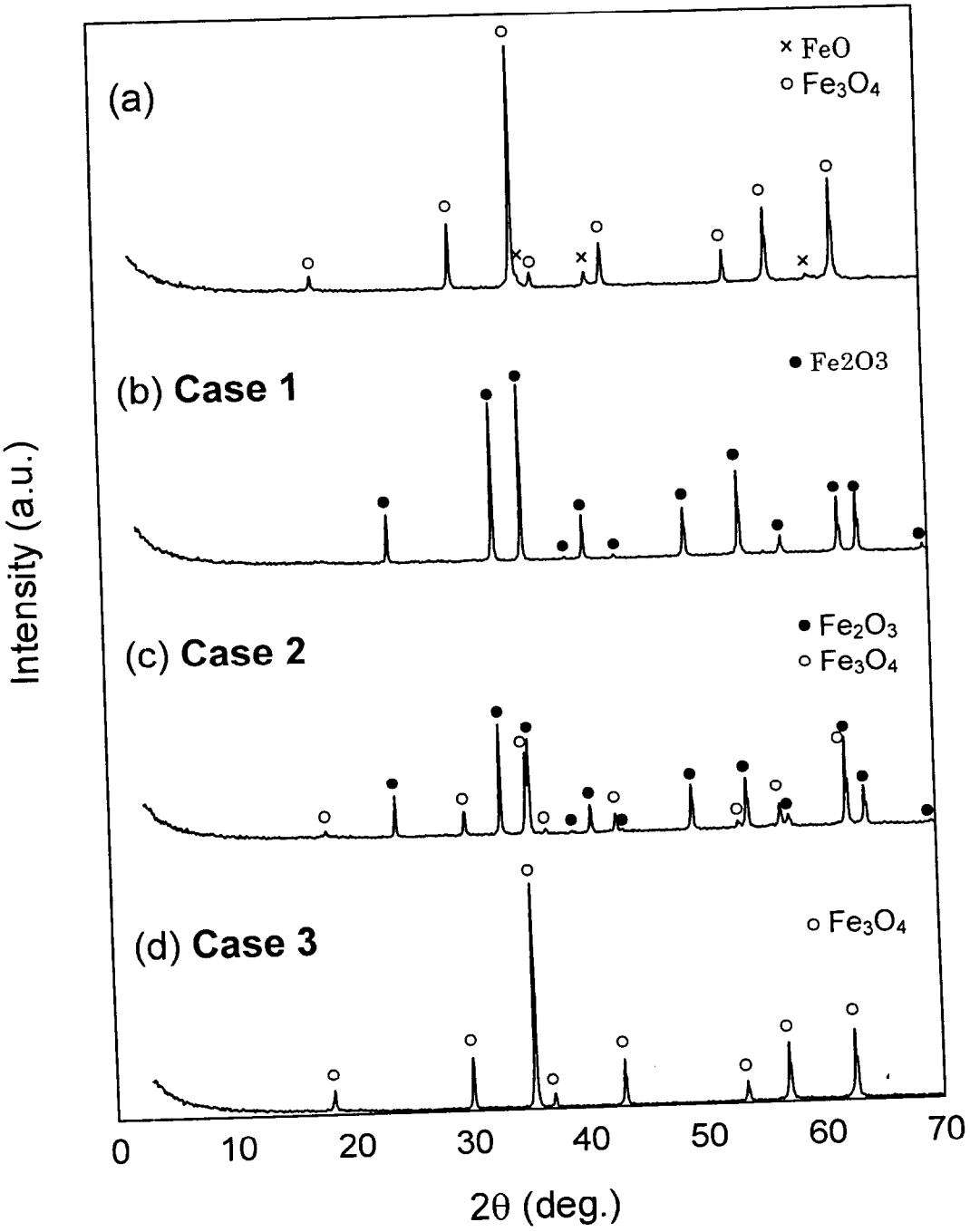

Fig. 3.1.3: XRD patterns for:

(a) Commercial Fe_3O_4,

(b) products after 1200 °C for 15 h in Ar flow (**Case 1**),

(c) products after 1000 °C for 15 h with Cu/Cu_2O as oxygen getter (**Case 2**),

(d) products after 1000 °C for 15 h with CoO/Co as oxygen getter (**Case 3**).

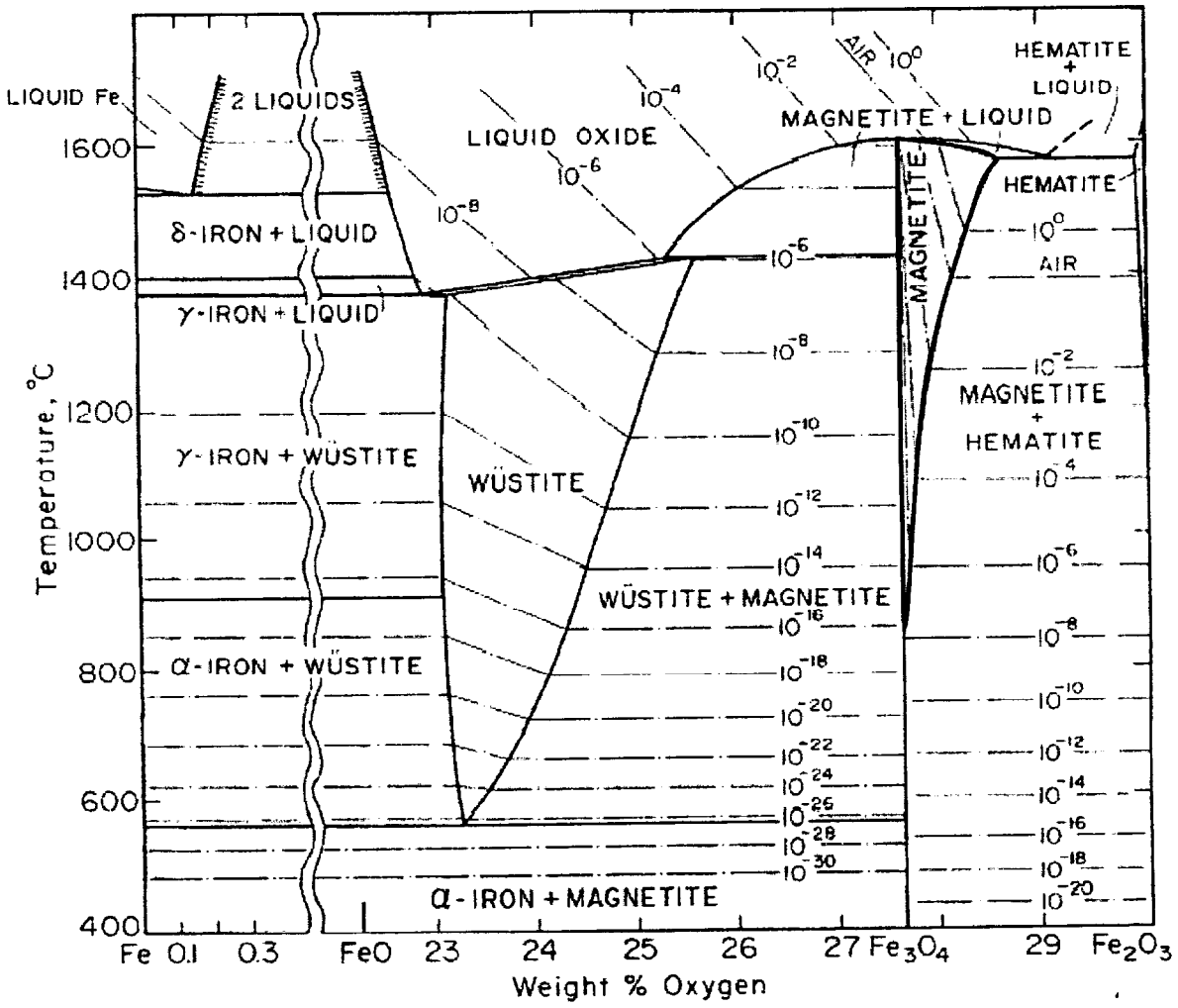

Fig. 3.1.4: Temperature-composition section for the system Fe – O at 1 atm [91-95]. Light dash-dot lines are oxygen isobars in atm.

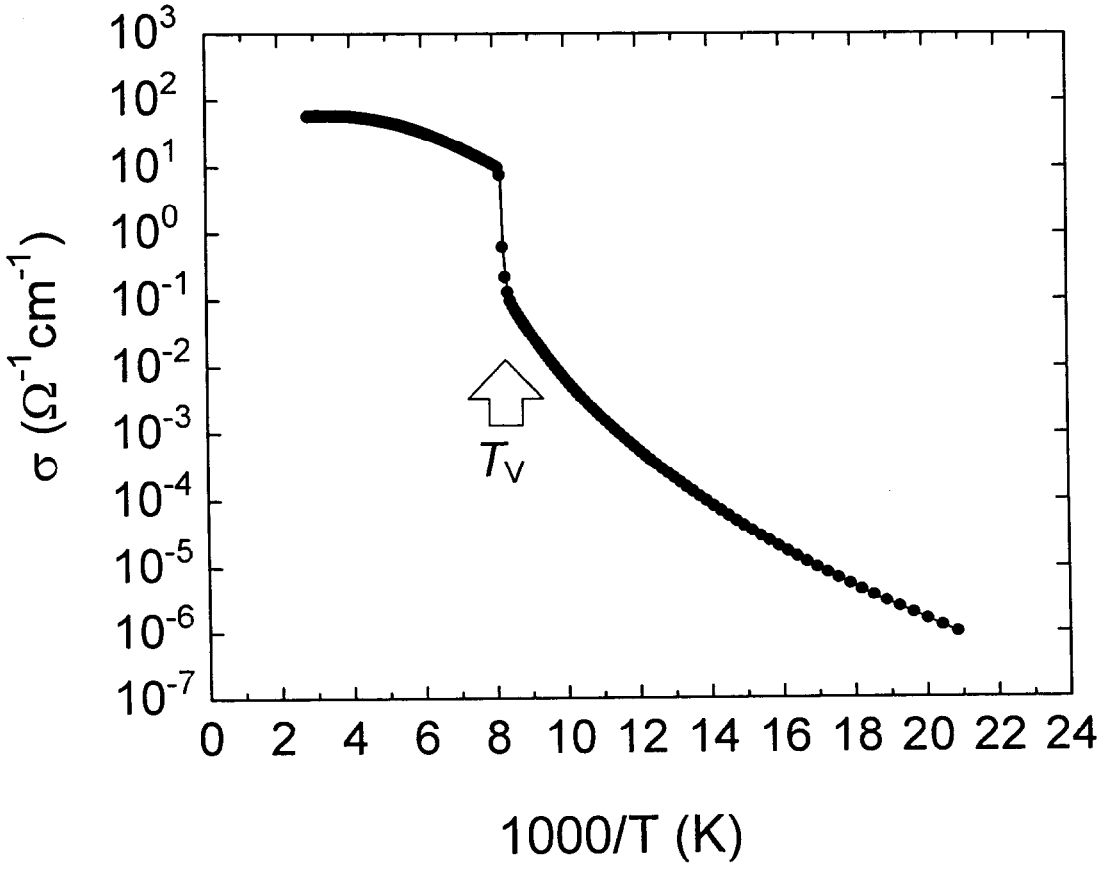

Fig. 3.1.5: Temperature dependence on the conductivity (cooling process) of the single-phase Fe_3O_4 obtaind by encapsulation technique.

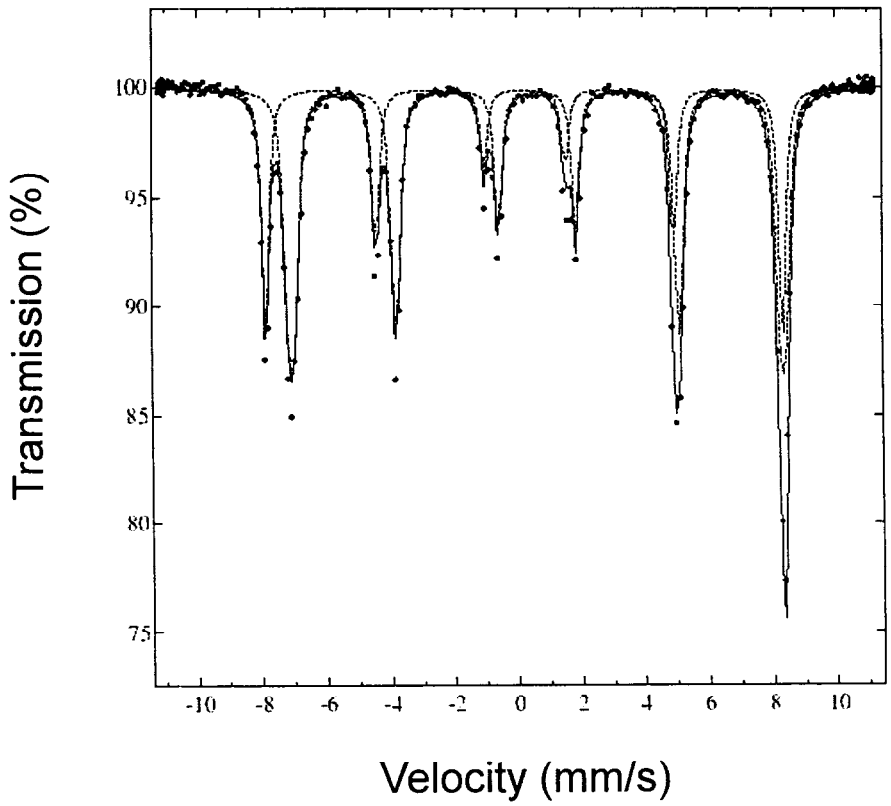

Fig. 3.1.6: Mössbauer spectra of Fe_3O_4 (150 K; above T_V) obtained by encapsulation technique. The spectra were fitted as Fe^{III} and $Fe^{2.5+}$.

Table. 3.1.2: The results of Mössbauer spectroscopy at 150 K (above T_V) for the Fe_3O_4 obtained by encapsulation technique.

	Inensity (%)	Field (T)	Isomer (mm/s)	eQVzz (mm/s)
Fe^{III}	35.3(3)	50.14(1)	0.354(1)	0.5(1)
$Fe^{2.5+}$	64.7(7)	47.716(9)	0.753(1)	-0.0(1)

3.2 Sample Quality and Solubility Limit

Using the encapsulation technique with oxygen getter (Fe metal), all the samples were synthesized. Fig. 3.2.1 (a), (b), (c) and (d) are for the high-resolution transmission-electron micrographs (HR-TEM), electron-diffraction (ED) pattern, XRD pattern and that's simulated pattern, respectively for the as-prepared $BaSmFe_2O_{5+\delta}$ sample. These figures indicate the double-perovskite structure. In the XRD pattern, the (0, 0, ℓ) peak are big, because of preferred orientation.

Fig. 3.2.2 and Fig. 3.2.3 show the SEM images for as-prepared $BaSmFe_2O_{5+\delta}$, which is synthesized by encapsulation technique, and $BaGdFe_2O_{5.019}$, which is gotten from Karen *et al.*, respectively. For $BaSmFe_2O_{5+\delta}$ sample, the average grain size is about 5 – 10 μm, while the grain size for $BaGdFe_2O_{5.019}$ sample are bigger. The deference between these samples on the grain size is due to the sintering way.

For the $Ba(Sm_{1-x}Ca_x)Fe_2O_{5+\delta}$ samples, all the synthesized samples were of single phase judging from the XRD patterns. The *c*-axis lattice parameter was found to slightly increase with increasing excess oxygen δ [II], whereas it slightly decreased upon increasing the Ca-substitution level, x (Fig. 5.2.1 (a) and (b) in Chapter 5). In the $Ba(Sm_{1-x}Ca_x)Fe_2O_{5.0}$ sample series, the length of the c axis lost its x dependence between x = 0.1 and 0.15, indicating that the solubility limit of Ca lies in the vicinity of x = 0.15. Similar leveling-off behaviors were revealed also from the other measurements performed for the sample series, *i.e.* resistivity and magnetization measurements.

Partial Sr-for-Ba substitution (Sr substitution) was succeeded up to 15 %, *i.e.*, $(Ba_{1-y}Sr_y)SmFe_2O_{5+\delta}$ ($0 \leq y \leq 0.15$) (Fig. 3.2.4). Complete substitution of the *RE* site by different *RE* ion (*RE* substitution) was tried ranging from La to Ho, *i.e.*, $BaREFe_2O_{5+\delta}$ (*RE* = La, Nd, Sm, Eu, Tb, Dy, Ho, Y). Fig. 3.2.5 shows the XRD patterns collected at room temperature for *RE* substituted samples. Here for the *RE* = Y sample, the XRD pattern is quite different, because the room temperature is below T_V of this phase, where the degree of orthorhombisity increase. And also *RE* = La sample shows like a single perovskite. This would mean that there are disorder between Ba and La. In these figures, the (0, 0, ℓ) peak of some samples are big, as it was mentioned befor, because of preferred orientation.

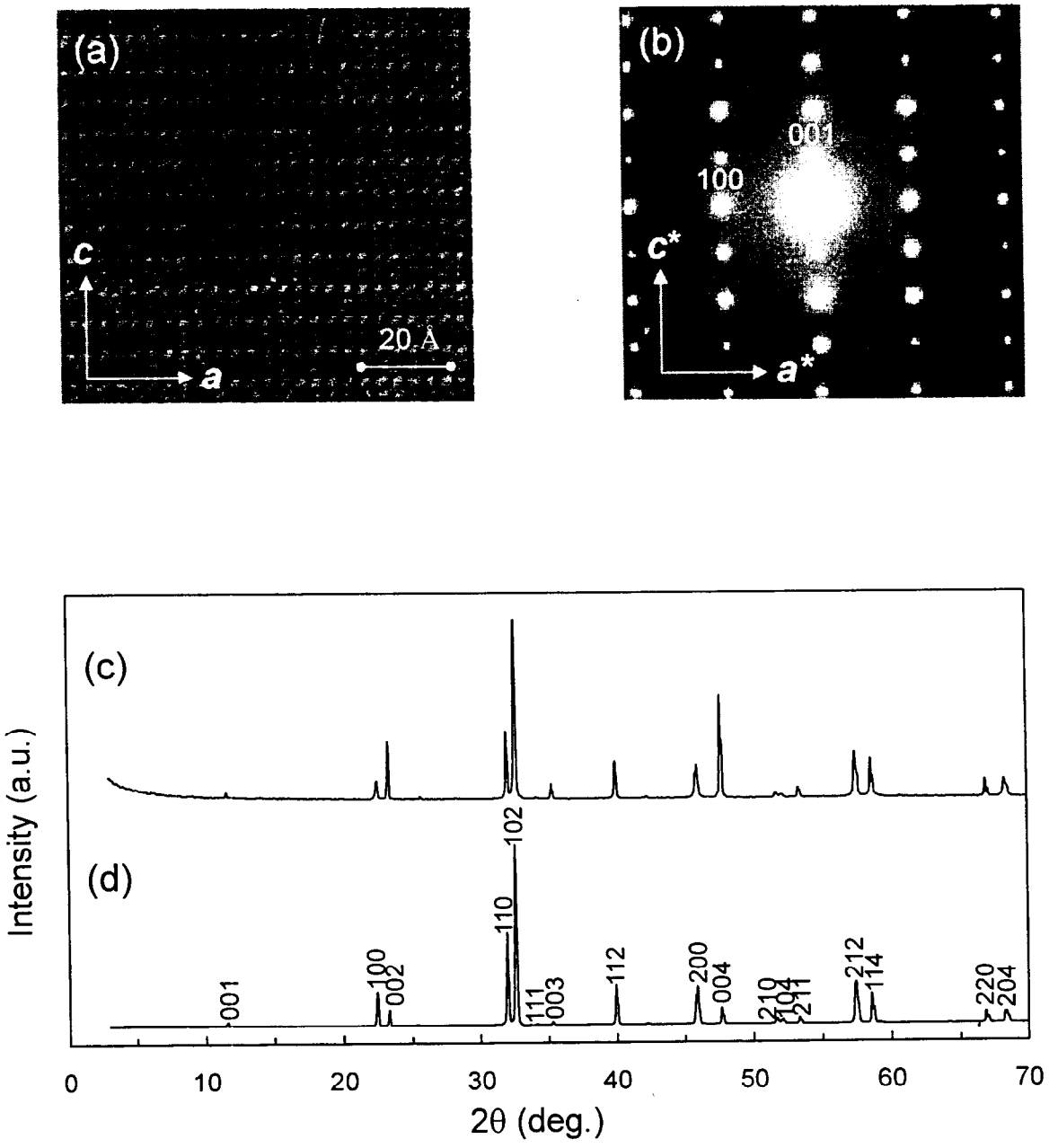

Fig. 3.2.1: Observation of the structure for the as-prepared $BaSmFe_2O_{5+\delta}$ sample at room temperature. (a) HR-TEM, (b) ED pattern, (c) XRD pattern and (d) simulated pattern.

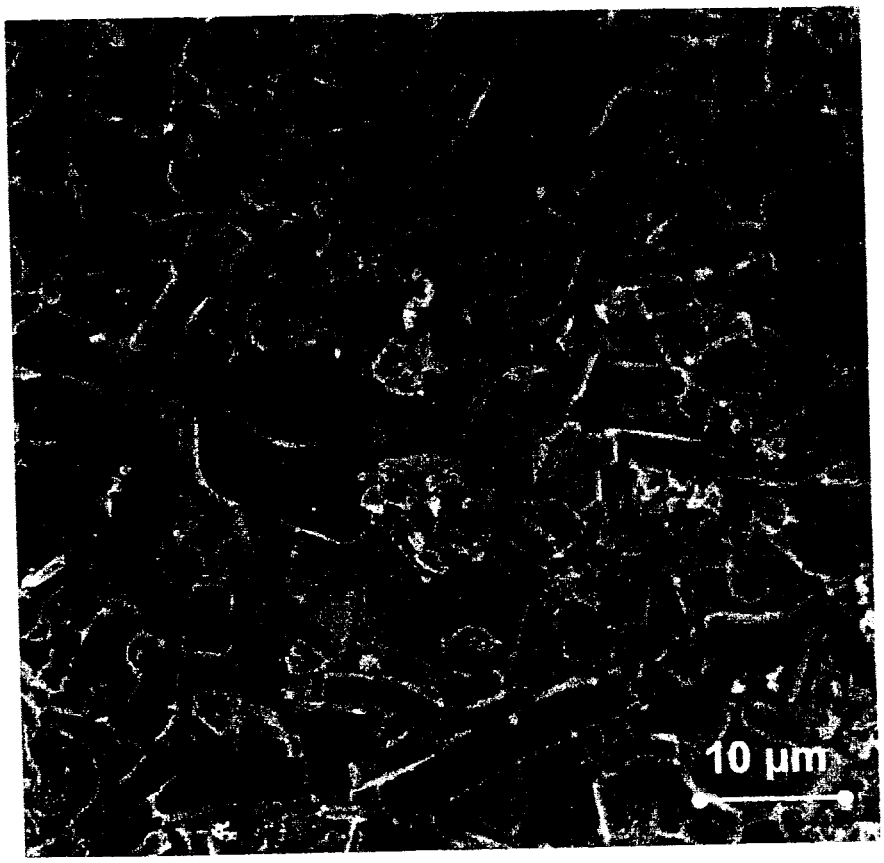

Fig. 3.2.2: SEM image of as-prepared $BaSmFe_2O_{5+\delta}$ sample. Typical grain size is about 5 – 10 µm.

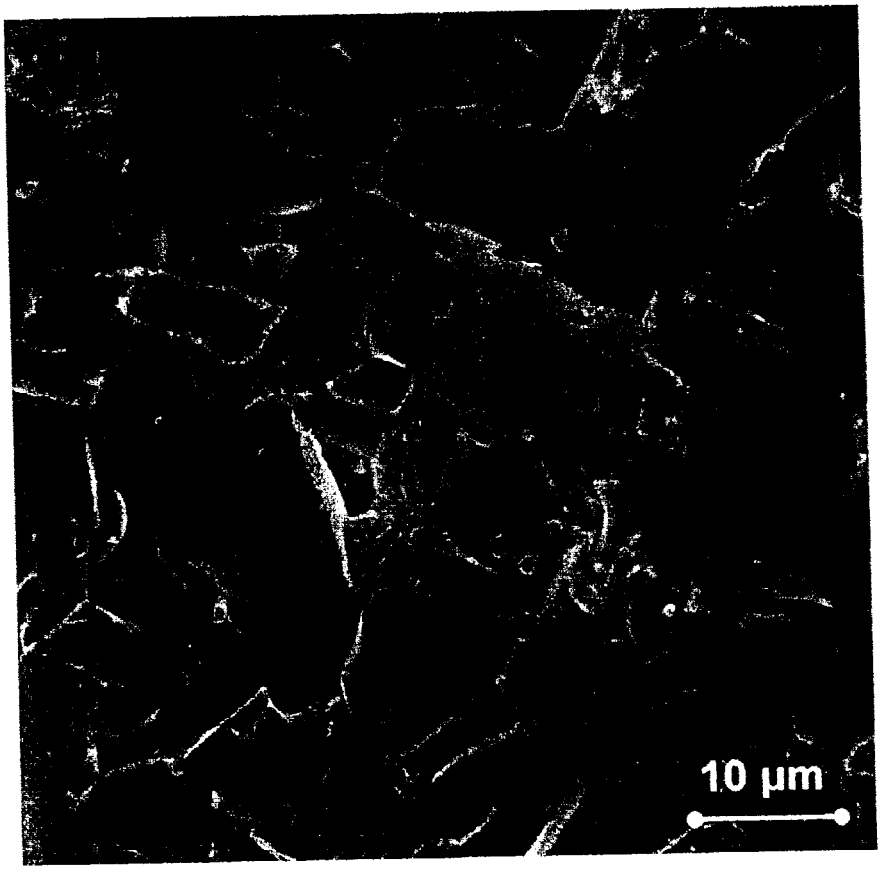

Fig. 3.2.3: SEM image of $BaGdFe_2O_{5.019}$ sample. The grains are tightly connecting each other.

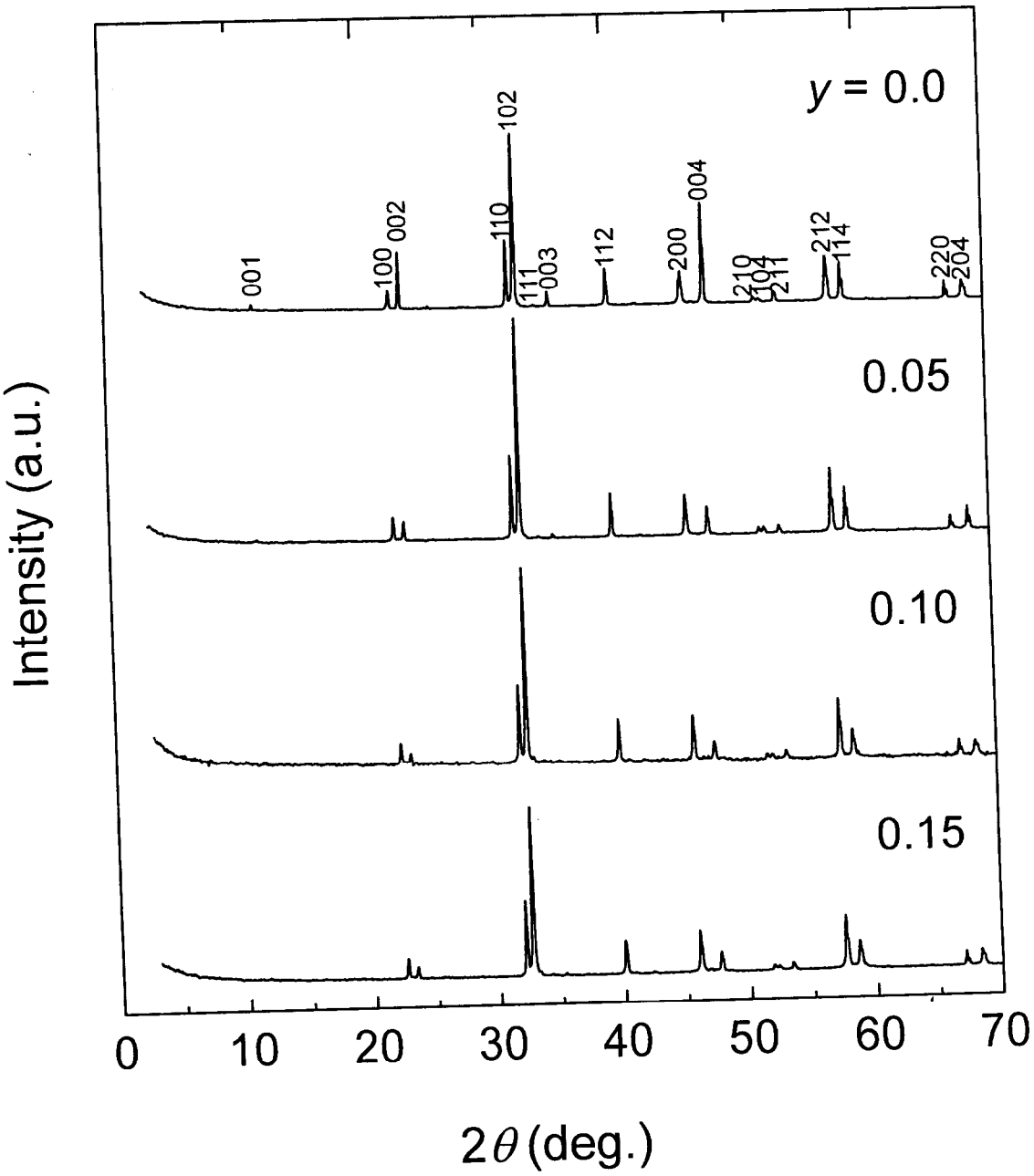

Fig. 3.2.4: XRD patterns for as-synthesized $(Ba_{1-y}Sr_y)SmFe_2O_{5+\delta}$ ($0.0 \leq y \leq 0.15$) samples at room temperature.

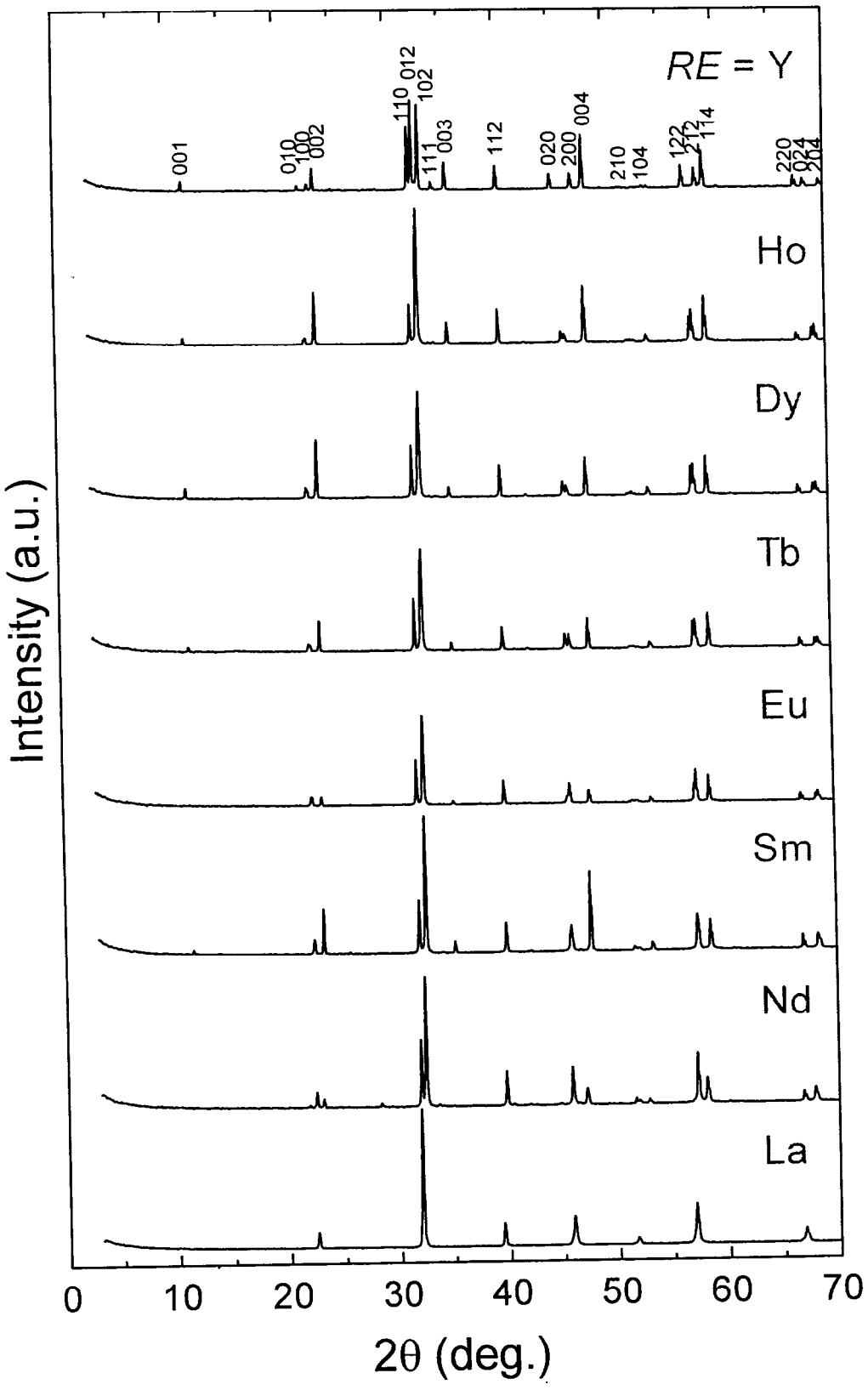

Fig. 3.2.5: XRD patterns for as-synthesized Ba*RE*$Fe_2O_{5+\delta}$ (*RE* = Ho, Y, Dy, Tb, Eu, Sm, Nd, La) samples at room temperature.

3.3 Conclusion

The sample synthesis was carried out by means of a novel oxygen-getter-controlled low-O_2-pressure encapsulation method that was developed during the course of this research. By utilizing this method, single-phase samples were obtained of the $Ba(Sm_{1-x}Ca_x)Fe_2O_{5+\delta}$ ($0 \leq x < 0.15$), $(Ba_{1-y}Sr_y)SmFe_2O_{5+\delta}$ ($0 \leq y \leq 0.15$) and $BaREFe_2O_{5+\delta}$ (*RE* = Y, Ho, Dy, Tb, Gd, Eu, Sm, Nd, La) systems. Furthermore by means of post annealing technique, $BaSmFe_2O_{5+\delta}$ ($0 \leq \delta \leq 0.28$) samples were obtained.

Chapter 4. Magnetic and Magnetoresistance Properties

4.1 Introduction

Negative magnetoresistance in the transition metal oxides is attractive because of the discovery of colossal magnetoresistance (CMR) in $RE_{1-x}A_xMnO_3$ (*RE*: rare earth and *A*: alkaline earth element) [81,96-98].

In an *A*-site ordered double perovskite system, a relatively big negative magnetoresistance effect (resistance ratio $R_{0T}/R_{7T} \approx 10$ at 10 K) has been seen also in the Co-based double perovskite Ba*RE*$Co_2O_{5+\delta}$ (*RE* = Eu, Gd) samples [14] at temperatures where the magnetic ordering competes between ferro- and antiferromagnetism. In the samples exhibiting the optimal magnetoresistance properties the Co valence was reported to be close to III, as judged by the oxygen content ($\delta \approx 0.5$). These results show that the strong interplay between magnetic and electronic properties exist, where the excess oxygen play an important role. In the iron-based *A*-site ordered double perovskite Ba*RE*$Fe_2O_{5+\delta}$ samples, the report related to the magnetoresistance effect has not existed.

In this Ba*RE*$Fe_2O_{5+\delta}$ samples, so far the magnetic properties has been reported as follows. Lindén *et al.* reported the Mössbauer spectra of Ba*RE*$Fe_2O_{5+\delta}$ (*RE* = Sm, $0.022 \leq \delta \leq 0.646$) as a function of temperature [38]. For all the samples which have different the amount of oxygen content, above and below T_V, all spectra were fitted using magnetic sextets, reflecting the antiferromagnetic ordering. In this paper, the magnetic susceptibility data were also reported for the same sample series, and those showed a small jump at T_V, *i.e.* the magnitude of magnetic susceptibility decreased with cooling temperature through T_V (Fig. 4.1.1). Karen *et al.* reported the spin arrangement in Ba*RE*$Fe_2O_{5+\delta}$ (*RE* = Tb, $\delta \approx 0$) by neutron powder diffraction [39]. It indicates that basically spin arrangement is antiferromagnetic, but only above T_V an interaction between FeO_2 plane across the *RE* layer becomes ferromagnetic (Fig. 4.1.2).

These magnetic fluctuations at T_V are useful for the magnetoresistance effect, so it is interesting to investigate about magnetoresistance, especially at T_V, in the iron-based double perovskite Ba*RE*$Fe_2O_{5+\delta}$ samples [V].

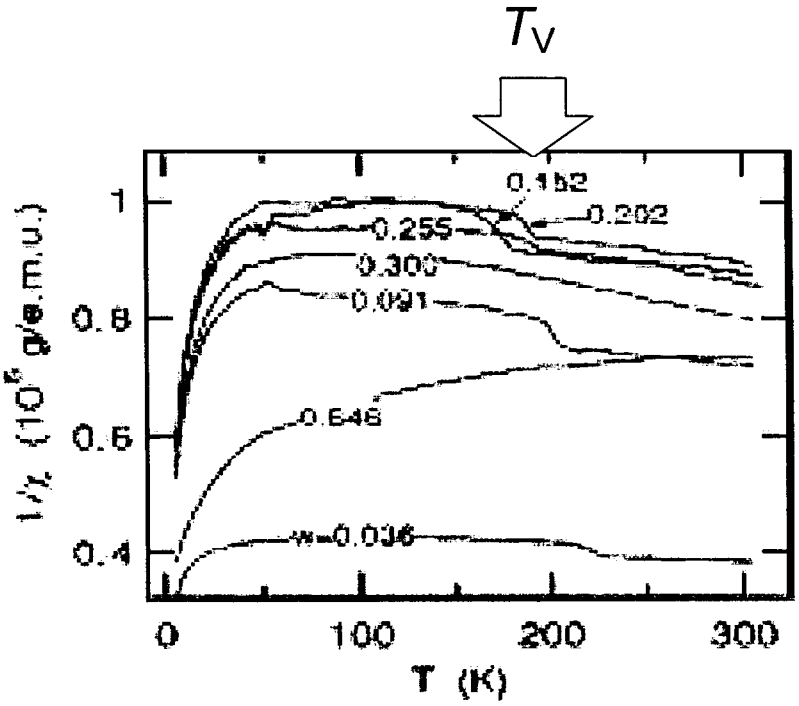

Fig. 4.1.1: Inverse magnetic susceptibility vs. temperature for selected samples of Ba*RE*Fe_2O_{5+w} (*RE* = Sm) reported by Lindén *et al.* [38]. A behavior at lower temperature is recognized as the influence of RE^{III} paramagnetic component.

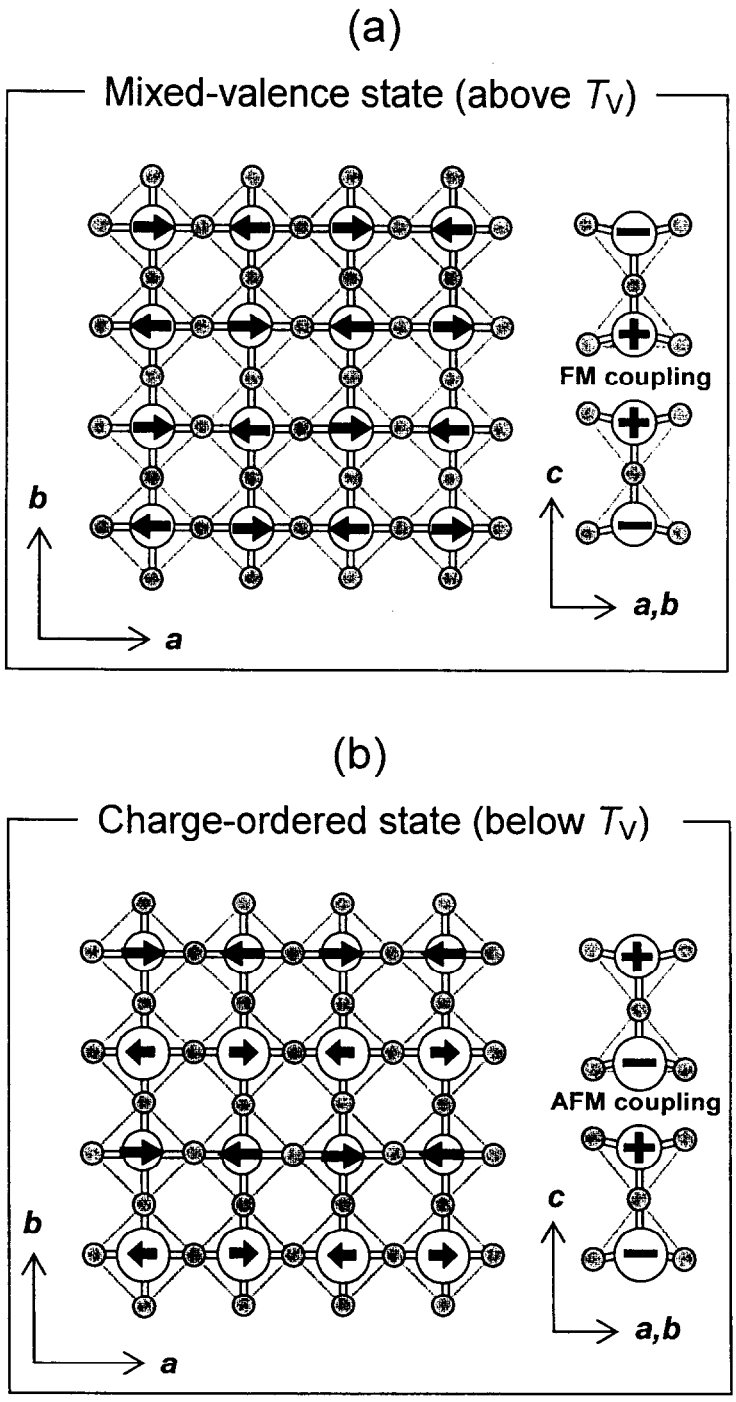

Fig. 4.1.2: Magnetic structure of Ba*RE*$Fe_2O_{5+\delta}$ (*RE* = Tb, $\delta \approx 0$) for: (a) mixed-valence state, and (b) charge-ordered state obtained from neutron scattering, reported by Karen *et al.* [39]. In the charge-ordered state, Fe^{II} and Fe^{III} are represented by larger and smaller spheres, respectively.

4.2 Results and Discussions

4.2.1 Magnetic Properties of Ba*RE*$Fe_2O_{5+\delta}$

To investigate the actual magnitude of the jump at T_V in the magnetic susceptibility, Ba*RE*$Fe_2O_{5+\delta}$ (*RE* = Y, $\delta \approx 0$) were measured. Here Y^{III} atom has no magnetic moment. Therefore this magnetic property derives from the moment of only Fe. If other RE^{III} species is included in the sample, the jump of magnetic susceptibility at T_V does not appear clearly, because the curve from RE^{III} para component which increases exponentially with decreasing temperature is added. As you can see in Fig. 4.2.1 (a), the Verwey-type transition was clearly observed around 300 K in the cooling process. Here the applied field was $\mu_0 H$ = 2 T. The magnetic moment was entirely small ($\approx$ 0.02 μ_B) owing to the antiferromagnetic property. At T_V the change of magnetic moment was only small value of about 0.003 μ_B, but relatively sharp. This absolute value of the change at T_V depends on the applied magnetic field linearly [VI], and it implies that the ratio of the increase with applied field is the same above and below T_V.

Certainly Fig. 4.2.1 (b), which shows the dependence of magnetization on the magnetic field shows that thing, *i.e.* at both temperature regions (higher and lower than T_V) the magnetization curves are almost on a straight line, which suggests that antiferromagnetic properties dominate in both regions. This antiferromagnetic arrangement is reasonable, since spins of the transition metal atom tend to arrange antiferromagneticlly if an oxygen atom exists between the transition metal atoms. The ferromagnetic arrangement which reported in REF 39 suggests one possibility which certain interaction between Fe atoms over the *RE* layer exists, although oxygen atoms which interpose the carriers are nothing and the distance between these Fe atoms is about 3.6 Å, which is not so small. So this interaction should be small, which is also reasonable for explanation of jump in the susceptibility. The same spin arrangement model with the reported ones (*RE* = Tb sample) also would be applied to other Ba*RE*$Fe_2O_{5.0}$ system (here *RE* = Y).

At T_V a small but sharp magnetic change occurs. To investigate a relationship between the magnetic and transport properties, next the magnetotransport properties are investigated around T_V.

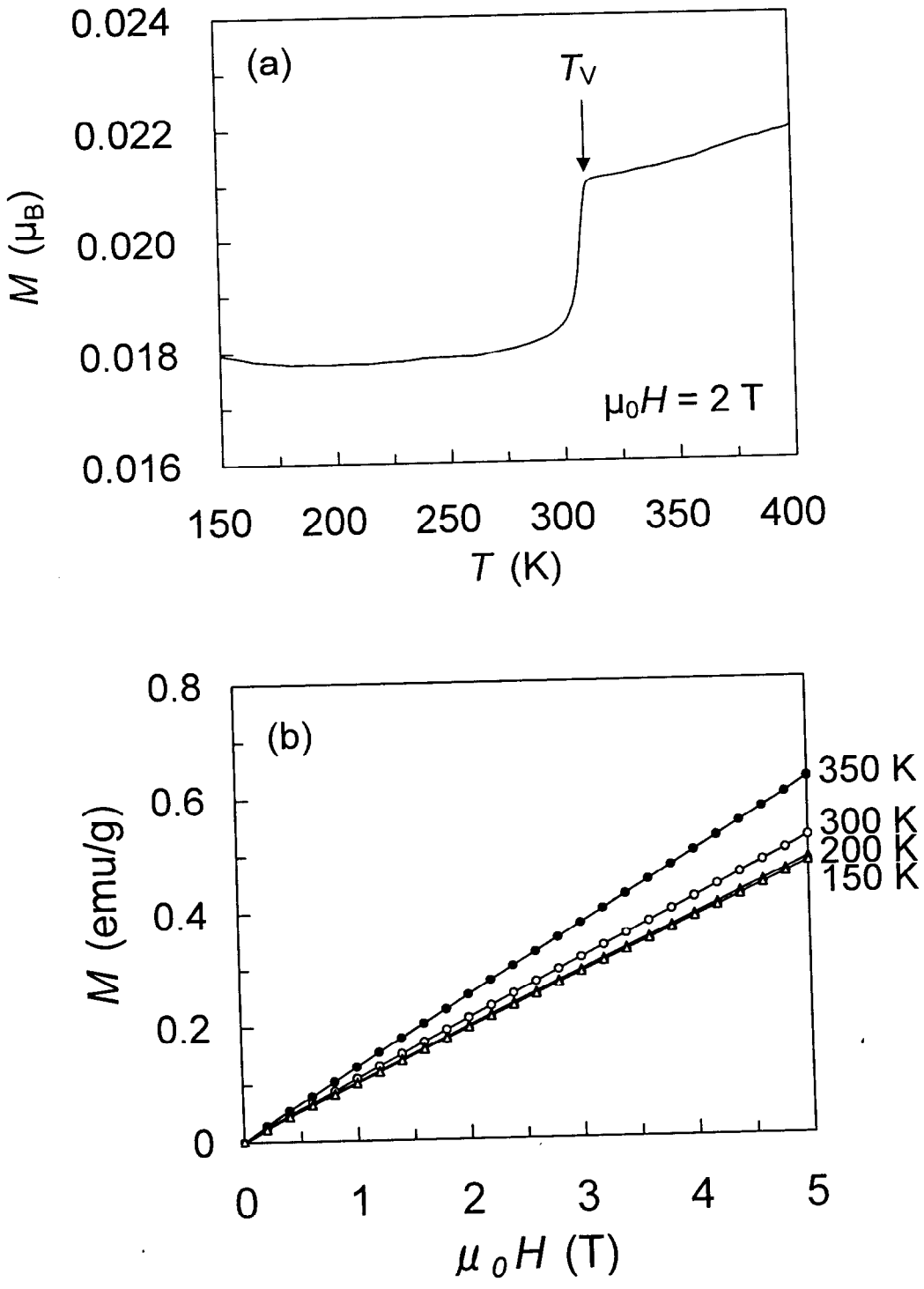

Fig. 4.2.1: Magnetic properties for Ba*RE*Fe$_2$O$_{5+\delta}$ (*RE* = Y, $\delta \approx 0$): (a) magnetic susceptibility under 2 T, and (b) magnetization at various temperatures in the vicinity of T_V.

4.2.2 Magnetoresistance Properties of Ba*RE*$Fe_2O_{5+\delta}$

In Fig. 4.2.2 the results from the resistivity *vs.* temperature measurements of the two Ba*RE*$Fe_2O_{5+\delta}$ (*RE* = Sm, $\delta \approx 0.04$ and 0.1) samples are shown using a logarithmic *y* scale and inverse temperature. At $T \approx T_V$ there is a change in the activation energy E_a, which results in a strong increase in the slope of the curves. An estimate of the activation energy can be obtained using the following expression for the sample resistivity, ρ:

$$\rho = \rho_0 \exp(E_a/k_B T) \qquad (1)$$

where ρ_0 is a constant and k_B is Boltzmann's constant. In the temperature region above T_V the plot appears to be linear as expected for a semiconductor. The slopes correspond to activation energies of 0.18 and 0.33 eV for the $BaSmFe_2O_{5.1}$ and $BaSmFe_2O_{5.04}$ samples, respectively. Below T_V the dependence deviates from a linear one, but at least for the $BaSmFe_2O_{5.1}$ sample the activation energy is higher than above the transition temperature. The deviation from a linear dependence at $T < T_V$ may suggest that the charge carriers propagate by a hopping mechanism. Additionally a hysteretical behavior in the region around the transition temperature is observed, which shows first order transition.

For the $BaSmFe_2O_{5.04}$ sample a magnetoresistance effect was observed, as seen in the resistivity curves of Fig. 4.2.3 (a). In particular in the transition region the external field of 7 T served to reduce the resistivity value. In order to obtain the magnitude of the MR effect the samples were measured at fixed temperatures by scanning the field. The MR value is defined as

$$\mathrm{MR}(T,H)\ (\%) = \frac{\rho(T,0) - \rho(T,H)}{\rho(T,H)} \times 100 \qquad (2)$$

where *T* and *H* denote the temperature and external field, respectively. In Fig. 4.2.3 (b) the resulting MR curves are presented for various temperatures. A peak in the MR value occurs at $T \approx T_V$. The peak at T_V becomes evident in a plot of the MR values (recorded for $\mu_0 H = 7$ T) *vs.* temperature. The result is given in Fig. 4.2.4, here the data by scanning the field like a Fig. 4.2.3 (b) was used for plotting it.

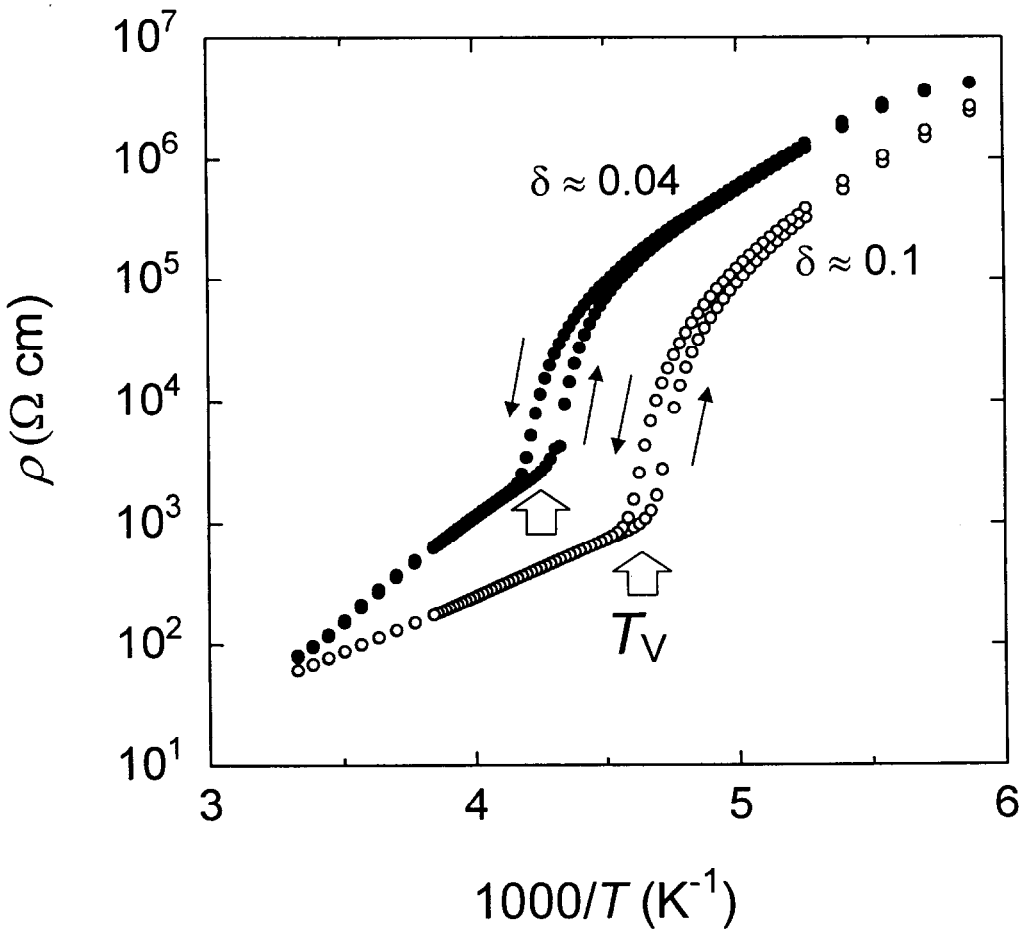

Fig. 4.2.2: Sample resistivity *vs.* inverse temperature in the heating and cooling process for the $BaSmFe_2O_{5+\delta}$ ($\delta \approx 0.04$: solid circle, and 0.1: open circle) samples, recorded at $\mu_0 H = 0$ T.

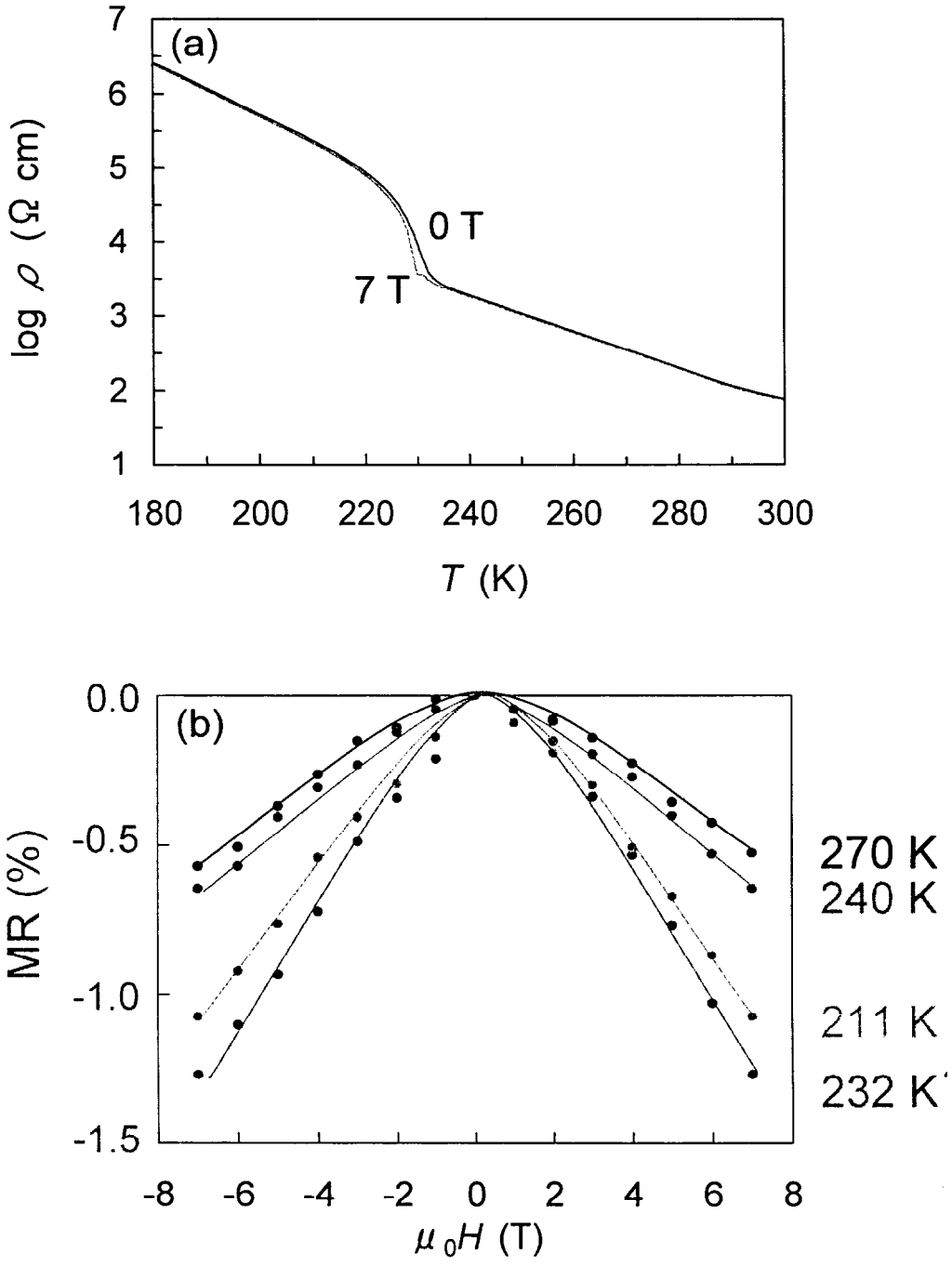

Fig. 4.2.3: (a) sample resistivity *vs.* temperature at $\mu_0 H$ = 0 T and 7 T in the cooling process, (b) MR *vs.* external field $\mu_0 H$ curves obtained at various fixed temperatures in the vicinity of T_V for the $BaSmFe_2O_{5+\delta}$ ($\delta \approx 0.04$) sample.

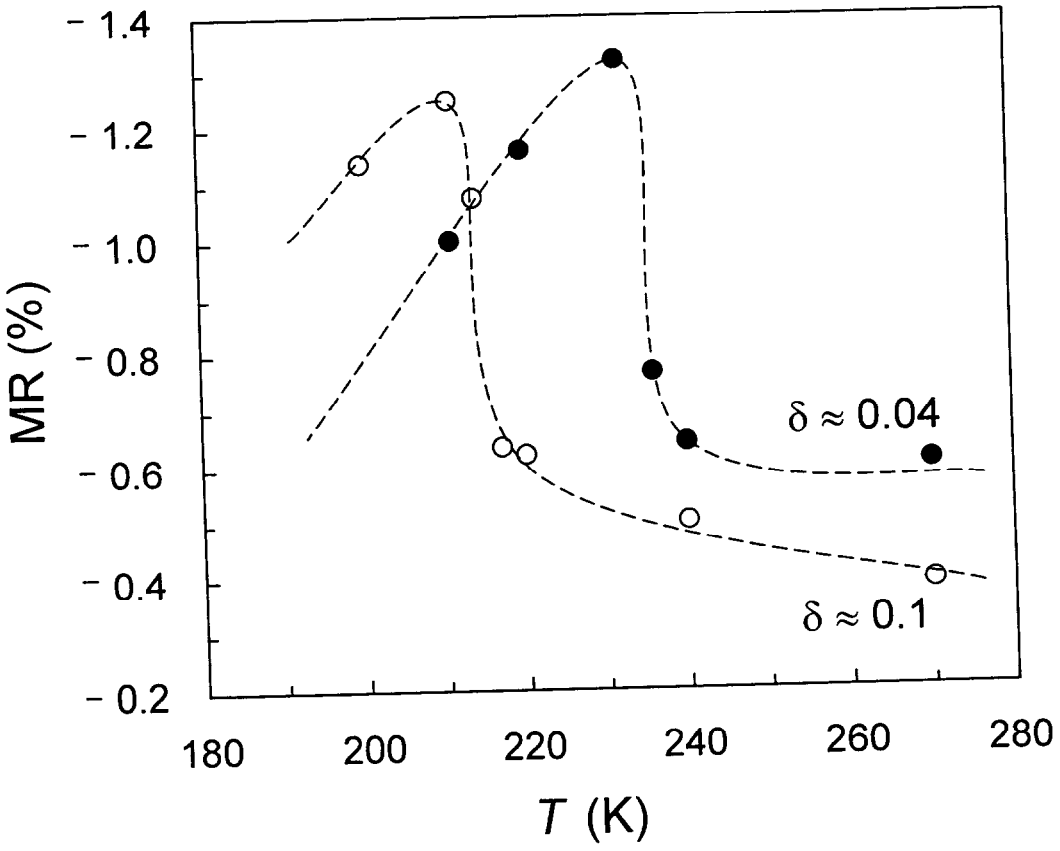

Fig. 4.2.4: The maximal MR values obtained at 7 T *vs.* temperature, for the $BaSmFe_2O_{5+\delta}$ ($\delta \approx 0.04$ and 0.1) samples. Lines are drawn as guides for the eye.

The origin of the current MR effect, *albeit* small, is believed to be different from that of the CMR [24,25] and TMR [99] systems. In the former the MR effect is closely connected to a magnetic transition, *e.g.*, competition between ferro- and antiferromagnetism [100], or between ferro- and paramagnetism. In addition to this the conductivity is substantially different for the competing phases and the location of the transition point itself is sensitive to the external field. Therefore the sample resistivity also depends on the applied magnetic field. Materials exhibiting TMR effects are half-metals, *i.e.*, the charge carriers are spin polarized. The scattering of charge carriers at grain/domain boundaries is therefore tunable by an external magnetic field, thus leading to a magnetic field-dependent sample conductivity. The magnetization data of the present samples exhibit an increase of ~ 1 % when T_V is passed from below, otherwise there is no sign of competition between various types of magnetic ordering. Contrary to the CMR and TMR systems the origin of magnetoresistance in the present case is likely to be directly connected to the charge-separation transition itself. Half-metallic features may indeed be present, but the occurrence of a peak at $T = T_V \ll T_C$ is not expected for half-metallic systems. On the contrary, the MR values for half-metals are found to decrease as a function of increasing temperature [86].

On the other hand, in single-perovskite iron-oxides $RE_{1/3}Sr_{2/3}FeO_{3-\delta}$ (*RE* = La, Pr) relatively small negative MR effect ($\approx$ 2.5 %) was also observed in the vicinity of the charge disproportionation (CD) and charge ordering (CO) temperature (Fig. 4.2.5) [I]. This phase and double-perovskite iron-oxides are similar each other, so the mechanism of the negative MR effect would be the same.

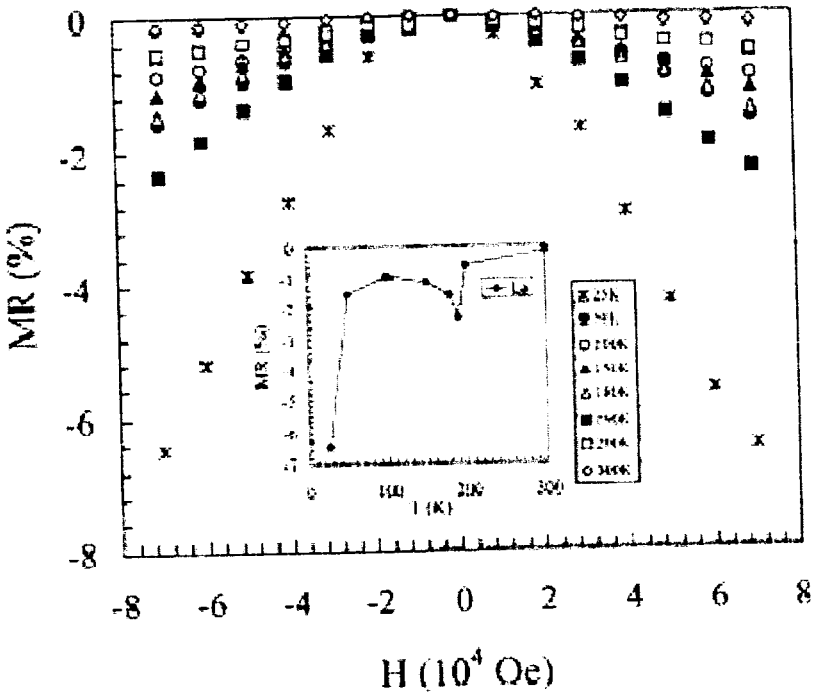

Fig. 4.2.5: Magnetoresistance *vs.* external field at various temperatures for single-perovskite iron-oxide $La_{1/3}Sr_{2/3}FeO_{3-\delta}$. The insets show the plots of MR *vs.* temperature [I].

4.3 Conclusion

For single-phase samples of the $BaSmFe_2O_{5+\delta}$ system, the highest negative magnetoresistance value of 1.4 % was obtained for the sample with the least amount of excess oxygen, $\delta = 0.04$, in the vicinity of T_V. At T_V the change in magnetization is minimal. It is therefore considered that the small value of MR is a reflection of the small change in magnetization at T_V. This system also has T_C (> 400 K) related to the change from para- to ferri-magnetism. Large MR effect would be seen in the vicinity of T_C.

Chapter 5. Oxidation Schemes

5.1 Introduction

In this iron-based double perovskite Ba*RE*$Fe_2O_{5+\delta}$ systems, so far it has been studied about oxygen loading effect as oxidation schemes [37-40]. In this case it was appeared that Verwey-type transition was suppressed with loading the excess oxygen. But at the same time with oxidation schemes, the connection between iron and iron across the *RE* layer are made, then the coordination number (*CN*) of Fe is changed. This effect is important for Verwey-type transition, because it has been reported that the six-coordinated Fe^{III} species do not participate in forming $Fe^{2.5+}$ pairs, *i.e.* it may be assumed that the presence or absence of the excess oxygen bears little or no impact on the Verwey-type transition [38].

At this point of view it is useful to study and compare the dependency of the Verwey-type transition on oxidation effect by two different oxidation schemes, *i.e.* by oxygen doping to the excess oxygen site (Fig. 5.1.1(a)) and Ca substitution at the *RE* site (Fig. 5.1.1(b)). For Ca substitution system, δ was fixed to 0, and *RE* is fixed to Sm for both systems [VII].

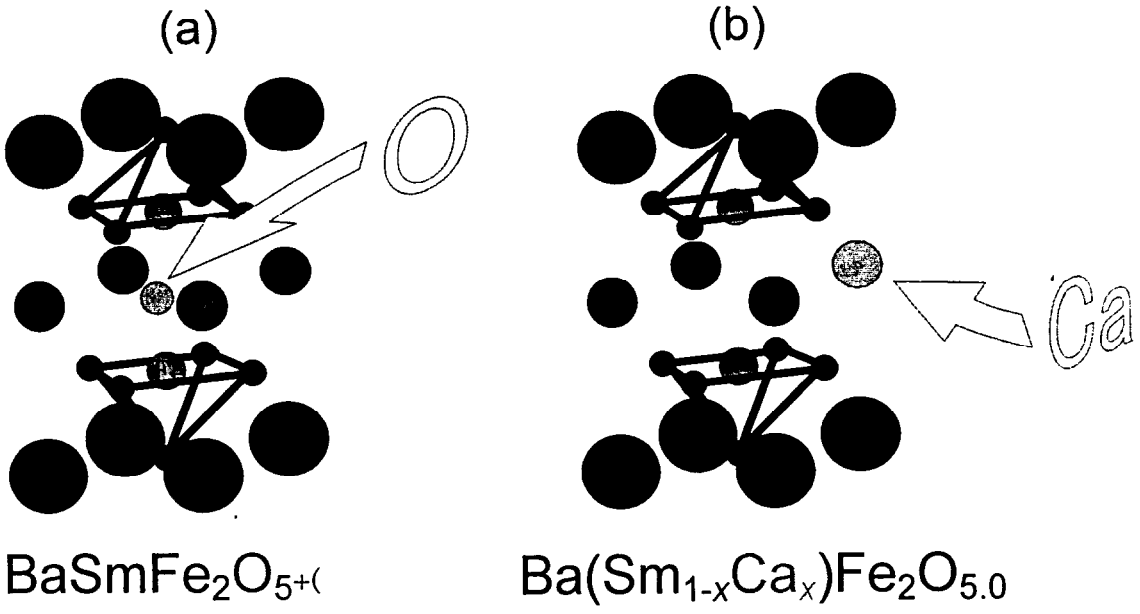

Fig. 5.1.1: A schematic illustration of (a) O-doped $BaSmFe_2O_{5+\delta}$, and (b) Ca-substituted $Ba(Sm_{1-x}Ca_x)Fe_2O_{5.0}$ sample.

5.2 Results and Discussions

5.2.1 Oxidation Schemes by Excess Oxygen and Ca Substitution

The *c*-axis lattice parameter was found to slightly increase with increasing the amount of excess oxygen δ [II,38], whereas it slightly decreased upon increasing the Ca-substitution level, *x* (Fig. 5.2.1(a) and (b)).

The Mössbauer spectra for the O-doped samples were essentially identical to those reported elsewhere [38]. In brief, the component assigned to the fluctuating valence state, $Fe^{2.5+}$, dominated the spectra of samples with low oxygen contents. Upon adding more oxygen, additional components emerged. Two components with internal fields of ~ 50 T and isomer shifts of ~ 0.35 mm/s were originated from 5- and 6-coordinated Fe^{III}. Additionally a component corresponding to unpaired Fe^{II} was seen. For the Ca-substituted samples similar spectra were obtained, except that the component corresponding to pure 5-coordinated Fe^{III} was found to gain intensity with increasing Ca content. At the same time the component for $Fe^{2.5+}$ became asymmetric with broadened resonance line-widths. The presence of small quantity (2 – 3 %) of the second ~ 50 T component, *i.e.* 6-coordinated Fe^{III}, indicated that the samples contained small amounts of excess oxygen. When cooled to 77 K, *i.e.* a temperature well below T_V, the characteristic 8 T component of Fe^{II} having participated in the valence mixing emerged for both Ca-substituted and O-doped samples. At the same time the saturated ~ 56 T component assigned to 5-coordinated Fe^{III} gained intensity, thereby signifying the valence-separation process.

The resistivity (ρ) *vs.* temperature (T) curves measured for the two sample series at 0 T are shown in Fig 5.2.2 (a) and (b). The Verwey-type transition is seen as a sharp increase in resistivity for the undoped sample. As the oxygen content, δ, increased the temperature corresponding to the jump slightly shifted, but still remained rather sharp (Fig. 5.2.2 (a)). On the other hand, Ca substitution shifted the jump to the lower temperature and broadened the transition region (Fig. 5.2.2 (b)). Above T_V, Ca substitution monotonically decreased resistivity, whereas the trend with O doping was rather opposite, though less clear.

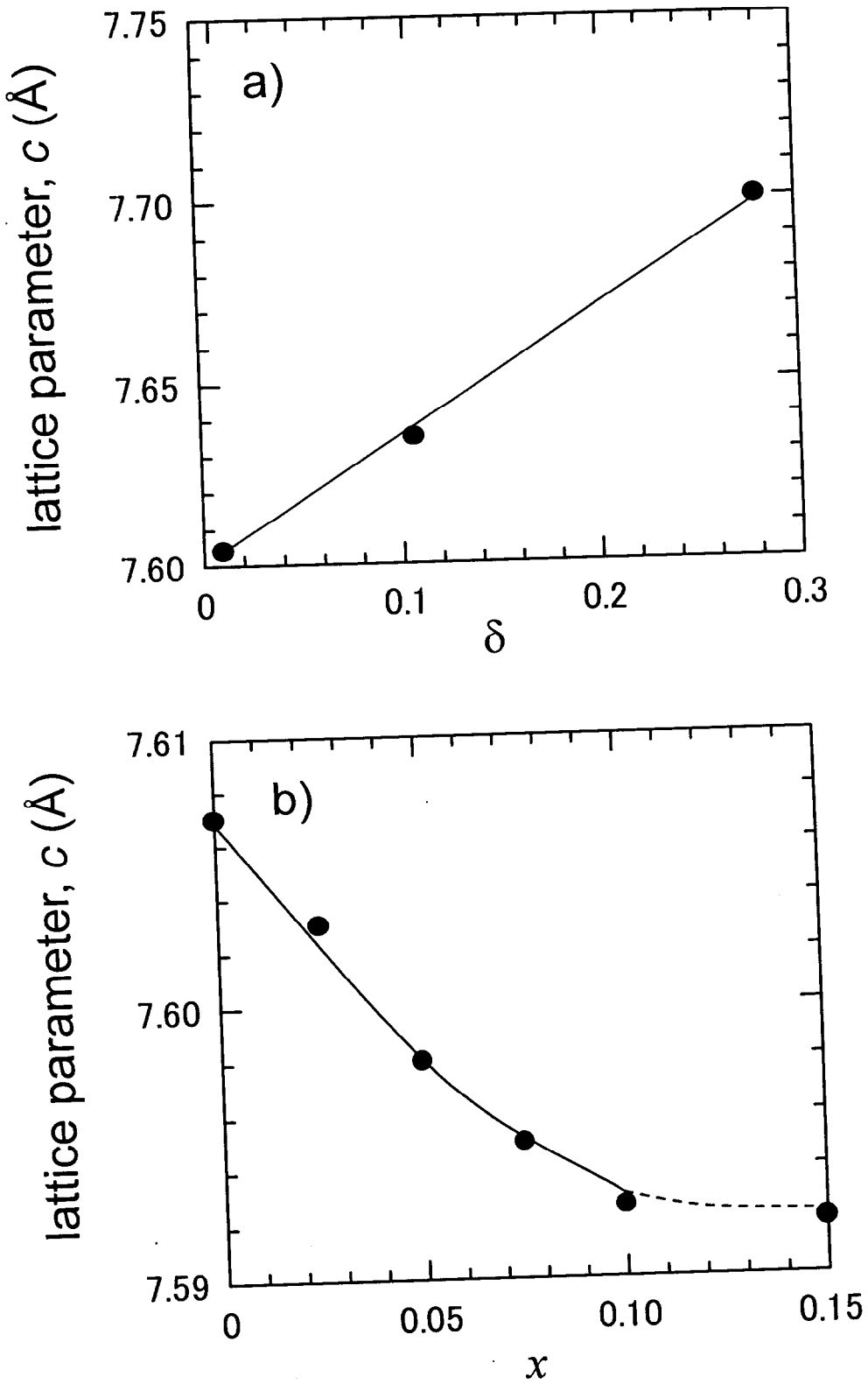

Fig. 5.2.1: Lattice parameter, *c vs.* δ/x for: (a) O-doped $BaSmFe_2O_{5+\delta}$, and (b) Ca-substituted $Ba(Sm_{1-x}Ca_x)Fe_2O_{5.0}$ samples.

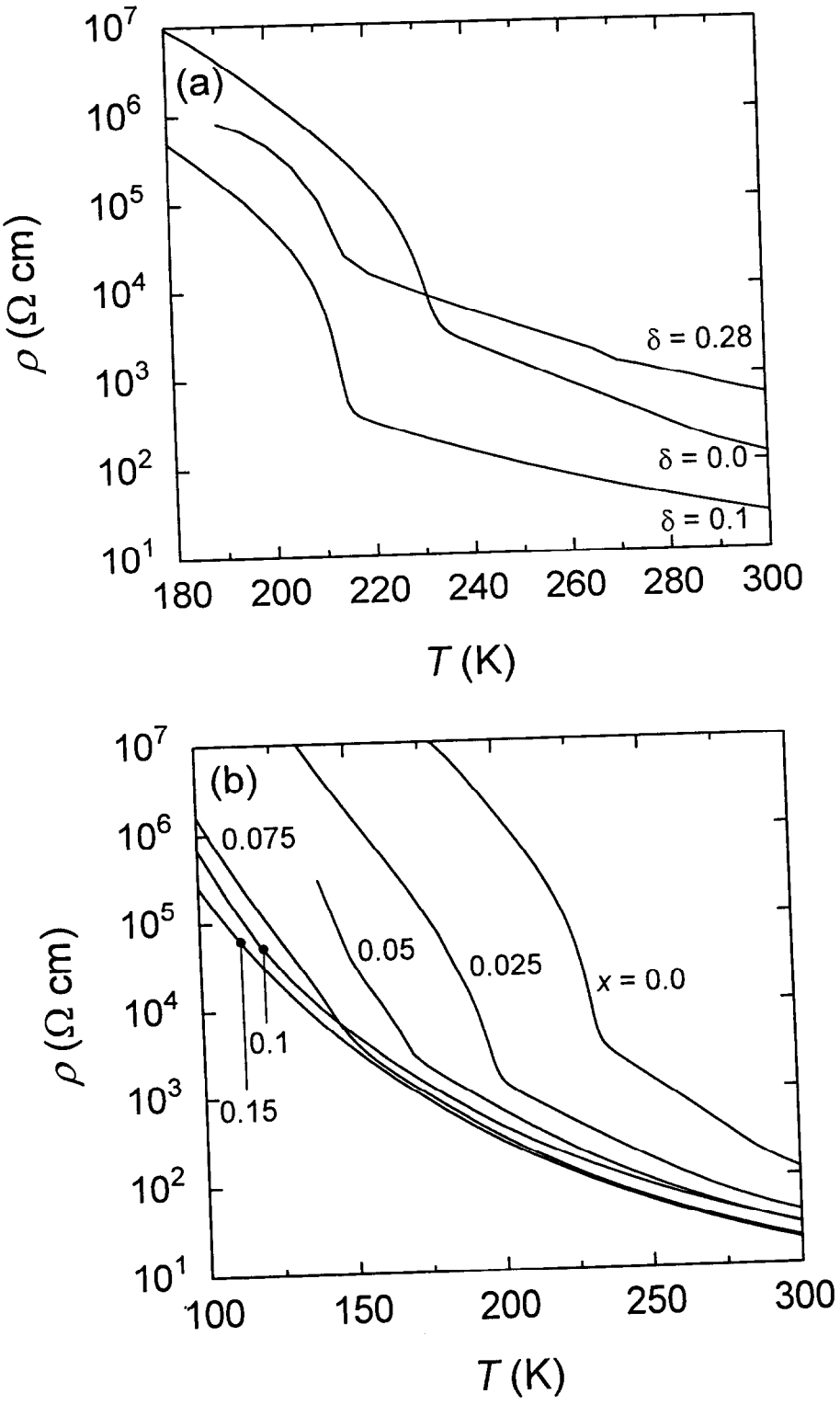

Fig. 5.2.2: Resistivity (ρ) *vs.* temperature (T) for: (a) O-doped $BaSmFe_2O_{5+\delta}$, and (b) Ca-substituted $Ba(Sm_{1-x}Ca_x)Fe_2O_{5.0}$ samples.

The Verwey-type transition was also clearly seen in magnetotransport properties of the samples measured at fixed temperatures using a maximum field of 7 T in the field-scan mode. The magnetoresistivity (MR) defined by

$$\mathrm{MR}(T,H)\,(\%) = \frac{\rho(T,0) - \rho(T,H)}{\rho(T,H)} \times 100 \qquad (1)$$

is plotted against temperature in Fig 5.2.3 (a) and (b) at $\mu_0 H$ = 7 T for the O-doped and Ca-substituted samples, respectively. From the MR vs. T curves, T_V was taken as the temperature where MR at $\mu_0 H$ = 7 T reaches its maximum. In Table 5.2.1 the T_V values determined from resistivity, magnetoresistivity and magnetic susceptibility measurements are given. The T_V values obtained for the O-doped samples using all the three methods agree rather well. For the Ca-substituted samples this is no longer the case. The origin of this discrepancy is not clearly known at the moment.

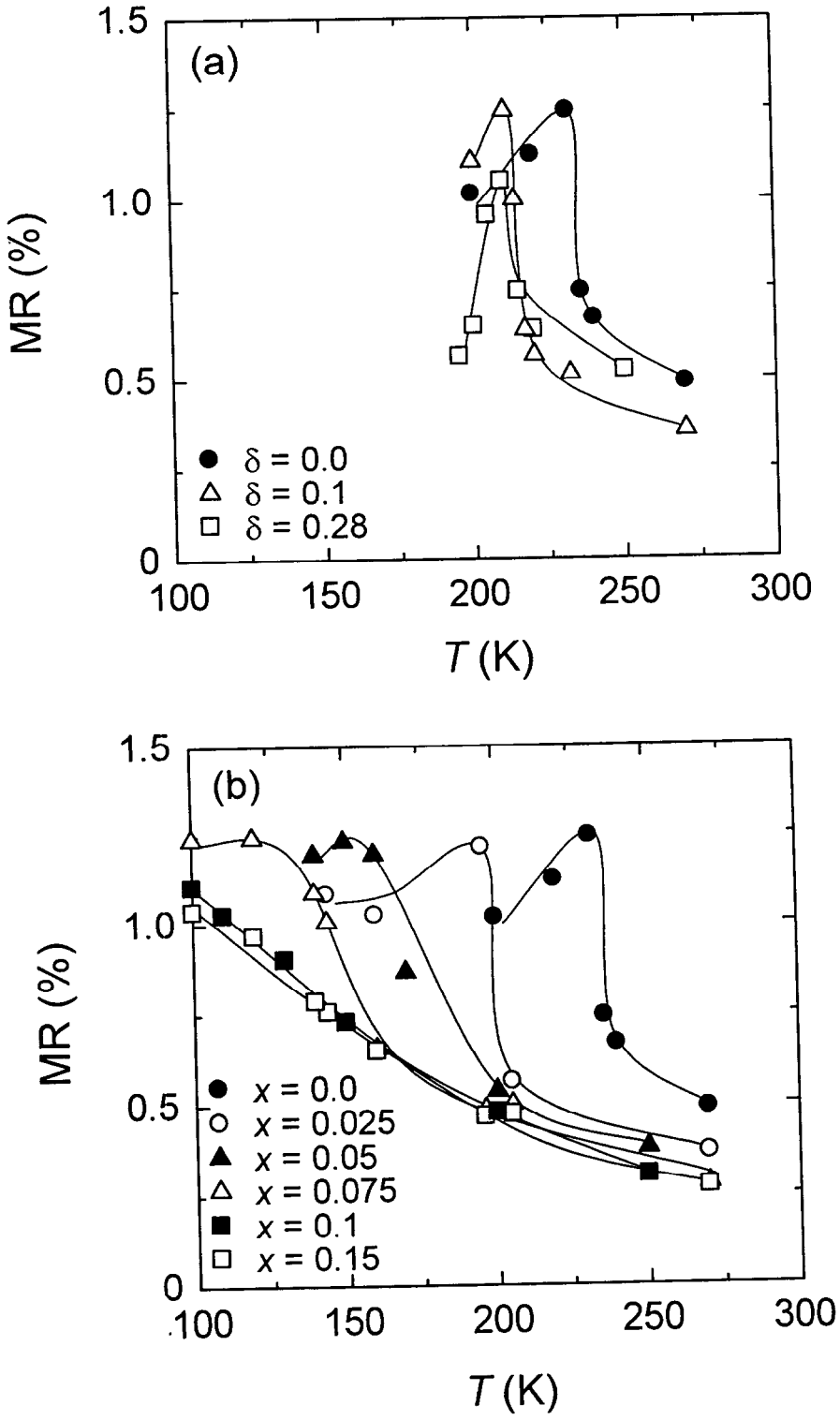

Fig. 5.2.3: Magnetoresistivity (MR) (as defined in Eq. (1)) *vs.* temperature (T): for (a) O-doped $BaSmFe_2O_{5+\delta}$, and (b) Ca-substituted $Ba(Sm_{1-x}Ca_x)Fe_2O_{5.0}$ samples.

Table. 5.2.1: Values of the Verwey-type transition temperature (T_V) determined from the dependence of magnetic susceptibility (χ), resistivity (ρ) and magnetoresistivity (MR; see Eq. (1)) for $BaSmFe_2O_{5+\delta}$ samples with various oxygen contents, $5+\delta$, and for $Ba(Sm_{1-x}Ca_x)Fe_2O_{5.0}$ samples with various Ca-substitution levels, x.

$BaSmFe_2O_{5+\delta}$

δ	0.0	0.1	0.28
χ	232(2)	215(2)	214(2)
ρ	233(2)	215(2)	214(2)
MR	232(2)	211(2)	210(2)

$Ba(Sm_{1-x}Ca_x)Fe_2O_{5.0}$

x	0	0.025	0.05	0.075
χ	232(2)	200(6)	171(6)	152(10)
ρ	233(2)	199(4)	170(6)	154(8)
MR	232(2)	196(2)	150(4)	120(6)

5.2.2 Differences between Two Oxidation Schemes

In Fig. 5.2.5 the experimentally obtained T_V values (taken from the MR peak) are plotted as a function of the average Fe valence. For the case of O doping the average Fe valence (V_{Fe}) is related to δ as

$$V_{Fe} = 2.5 + \delta, \tag{2}$$

whereas for Ca substitution the average valence is given by

$$V_{Fe} = 2.5 + x/2. \tag{3}$$

The two doping schemes lead to two different branches in the T_V *vs.* V_{Fe} plot. That is, oxidation alone cannot explain the T_V *vs.* V_{Fe} behavior. Lattice distortions might have some effect on the value of T_V. However, the change in *c*-axis length is of opposite sign for the two doping schemes. The following approach is therefore adopted: starting at a low temperature below T_V the occurrence of the Verwey-type transition can be regarded as a kind of melting, *i.e.* the entropy increases in the neighborhood of T_V, as shown *e.g.* by calorimetric measurements [38]. Furthermore, as mentioned in the introduction of this chapter, it has been shown that six-coordinated Fe^{III} species do not participate in forming $Fe^{2.5+}$ pairs [38], *i.e.* we may assume that their presence or absence bears little or no impact on the Verwey-type transition. It is therefore conceivable that the temperature at which the $Fe^{2.5+}$ pairs are formed is dictated by the ratio, of available five-coordinated Fe^{III} species to Fe^{II} species (with five-coordination) or rather the entropy change at T_V. The situation for the two doping schemes is illustrated in Fig. 5.2.6: Ca substitution and O doping differ in the sense that O doping does not change the number of five-coordinated Fe^{III}. In the interval $0 \leq \delta \leq 0.5$ the portion of five-coordinated Fe^{III} is constantly 50 %, whereas the number of Fe^{II} species decreases upon oxygen loading. Ca substitution, on the other hand, both increases the number of five-coordinated Fe^{III} and decreases the number of Fe^{II}. And the ratio of Fe^{III} ($CN = 5$) to Fe^{II} ($CN = 5$) are plotted against average valence of Fe for Ca-substituted and O-doped sample (Fig. 5.2.7).

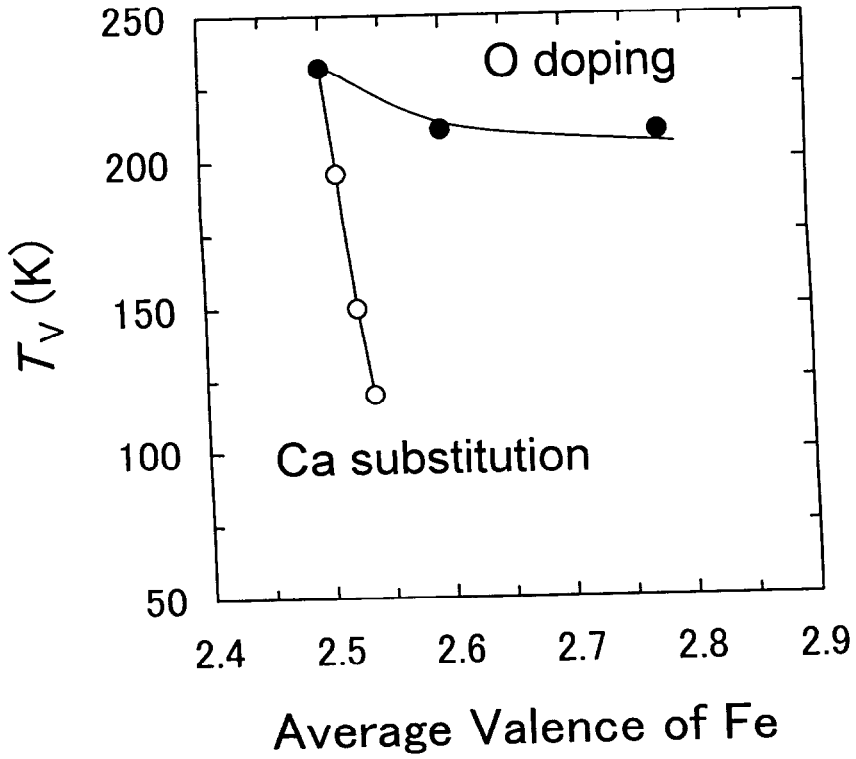

Fig. 5.2.5: Dependence of T_V on average valence of Fe for the O-doped and Ca-substituted samples. The T_V values determined only from MR – T measurements were used.

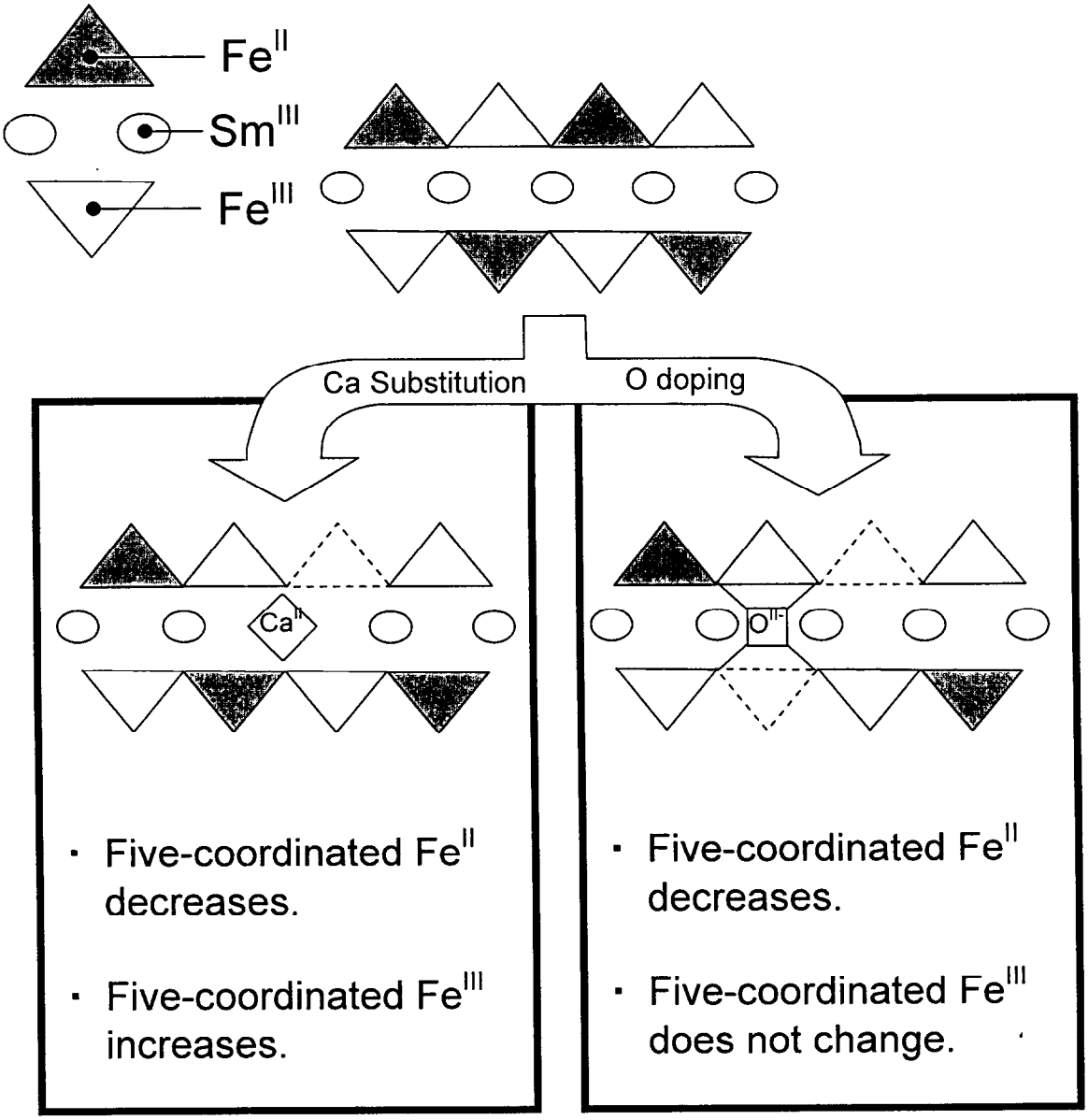

Fig. 5.2.6: A Schematic illustration of the changes in Fe coordination numbers and valences upon O doping or Ca substitution in $Ba(Sm_{1-x}Ca_x)Fe_2O_{5+\delta}$.

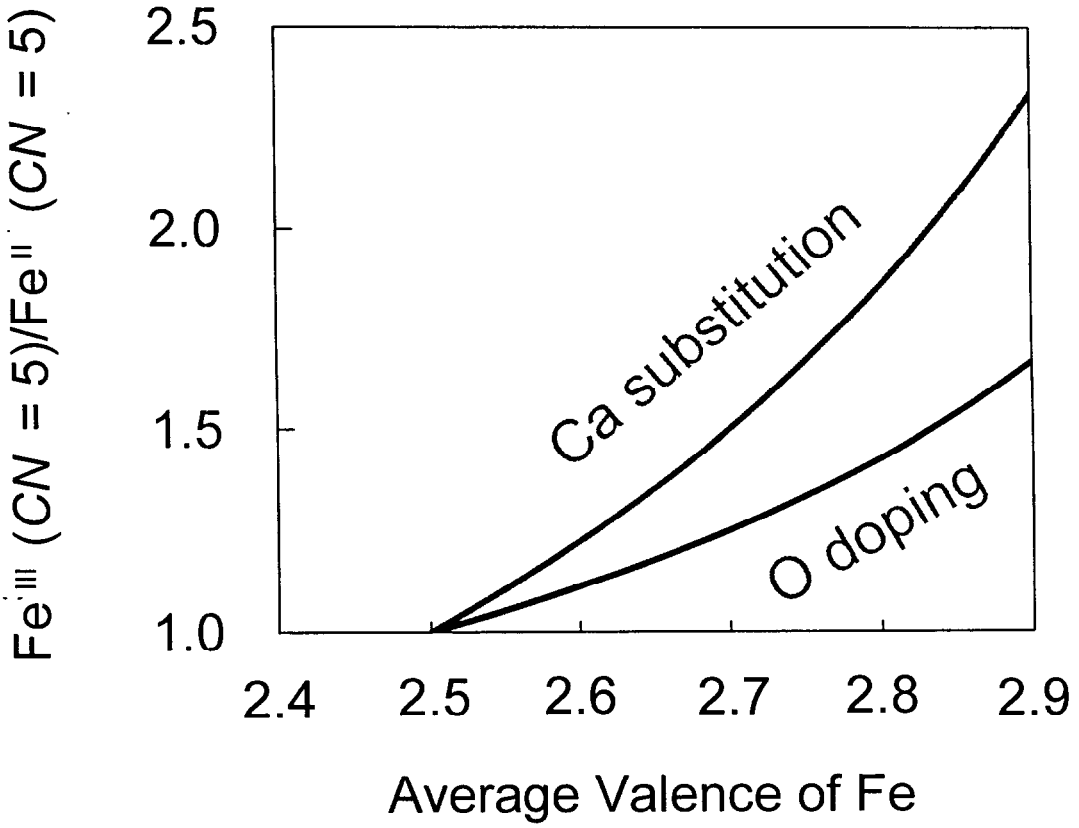

Fig. 5.2.7: The ratio of Fe^{III} (CN = 5) to Fe^{II} (CN =5) *vs.* Average Valence of Fe: for O-doped $BaSmFe_2O_{5+\delta}$, and Ca-substituted $Ba(Sm_{1-x}Ca_x)Fe_2O_{5.0}$ samples.

Proceeding to calculate the entropy change (ΔS) at T_V for the two substitution schemes we first note that the entropy change upon melting, for the non-substituted sample ($\delta = 0, x = 0$) is simply [101]:

$$S = k_B N \ln 2 . \tag{4}$$

This is the increase in entropy upon a complete melting of the (charge-)ordered Fe^{II} Fe^{III} structure. For oxygen loading the number of microstates is obtained through a simple combinatorial calculation:

$$\Omega_O = \frac{[N(1-\delta)]!}{[N((1/2)-\delta)]![N/2]!} , \tag{5}$$

where $N((1/2) - \delta)$ is the number of Fe^{II} and $N(1 - \delta)$ is the total amount of five-coordinated Fe. The entropy is now obtained as $S = \ln(\Omega)$, yielding:

$$S_O = k_B N[(1-\delta)\ln(\frac{1-\delta}{(1/2)-\delta}) + \frac{1}{2}\ln(1-2\delta)] . \tag{6}$$

For Ca substitution the number of Fe^{II} and Fe^{III} species are $N/2(1 - x)$ and $N/2(1 + x)$, respectively. In this case the number of microstates is given by:

$$\Omega_{Ca} = \frac{N!}{[N/2(1-x)]![N/2(1+x)]!} , \tag{7}$$

leading to the following expression for the entropy:

$$S_{Ca} = \frac{1}{2} k_B N [\ln 4 + x\ln(\frac{1-x}{1+x}) - \ln(1-x^2)] . \tag{8}$$

Note that upon setting x and δ to zero in Eqs. (6) and (8) we get Eq. (4), as expected. Expressing Eqs. (6) and (8) with the common variable V_{Fe} using Eqs. (2) and (3) we get:

$$S_O = k_B N[(1 + (2.5 - V_{Fe}))\ln(\frac{3.5 - V_{Fe}}{3 - V_{Fe}}) + \frac{1}{2}\ln(6 - 2V_{Fe})] \quad (9)$$

and

$$S_{Ca} = \frac{1}{2} k_B N[\ln 4 + 2(V_{Fe} - 2.5)\ln(\frac{1 - 2(V_{Fe} - 2.5)}{1 + 2(V_{Fe} - 2.5)}) - \ln(1 - 4(V_{Fe} - 2.5)^2)], \quad (10)$$

for the O-doped and Ca-substituted samples, respectively.

In order to facilitate comparison with the experimental T_V values we use the expression:

$$\Delta S = \Delta Q/T_V, \quad (11)$$

where ΔQ is the change in enthalpy upon melting. We have to make a reasonable assumption for ΔQ. Assuming that the number of $Fe^{2.5+}$ pairs decreases linearly with the increase of V_{Fe} we may write:

$$\Delta Q = Q_0(1 - 2(V_{Fe} - 2.5)), \quad (12)$$

i.e. the amount of energy required to melt the mixed valence pairs is directly proportional to their number. We may now proceed to calculate a theoretical T_V *vs.* V_{Fe} dependence using (9,10) and (11,12). Q_0 is simply chosen to yield T_V = 232 K (Table. 5.2.1) for $x = \delta = 0$. The data of Fig. 5.2.8 was constructed using this procedure. We immediately note that the Ca-substitution scheme leads to lower T_V, although the decrease is slower than experimentally found.

According to Ref. 38 not all five-coordinated Fe^{III} species can participate in $Fe^{2.5+}$ pair formation, *i.e.* some Fe^{III} species adjacent to the oxygen octahedral are 'immobilized' from $Fe^{2.5+}$ pair formation, leaving only a fraction, $(0.5 - \delta)$ to participate in such pair formation. If this correction is considered the entropy change at T_V would decrease slightly, but so would ΔQ. Therefore the $T_V = \Delta Q/\Delta S$ ratio would not necessarily change much in this zeroth-order calculation.

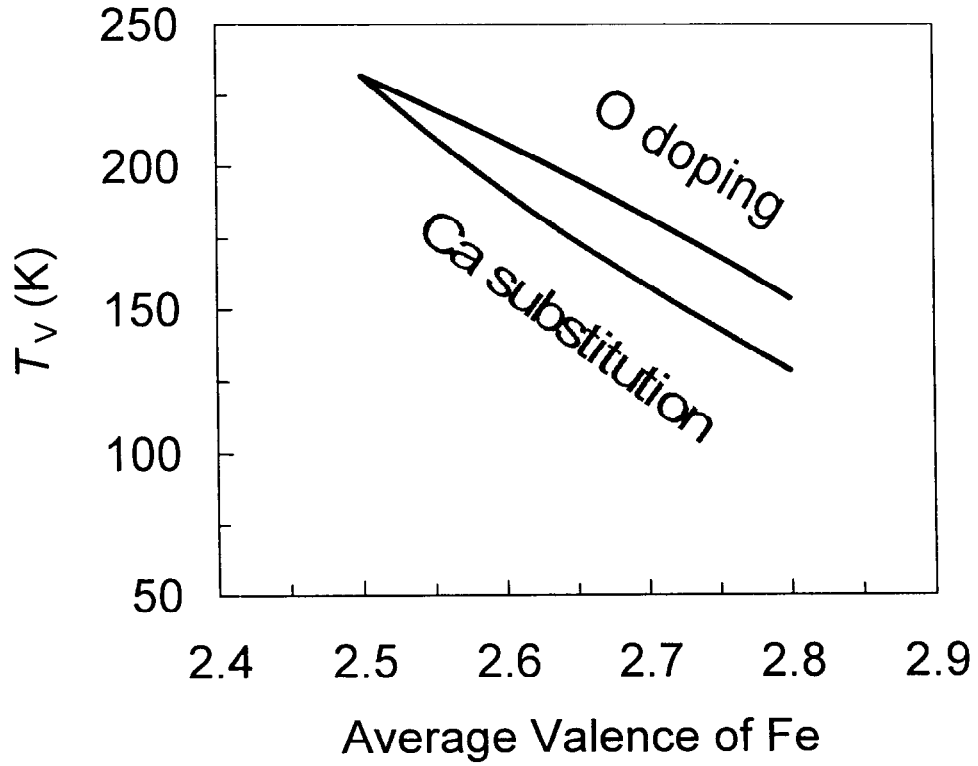

Fig. 5.2.8: The theoretical T_V *vs.* V_{Fe} behavior, as obtained from the combinatorial-entropy model, see text.

Additional support for the above results can be found by comparing experimental ΔS values, with the calculated. In Ref. 39 a total enthalpy change of 2.623 kJ/mol, the Verwey-type transition temperature of 285.1 K and a total entropy change of 9.20 J/molK are reported for a sample of $BaTbFe_2O_{5.0}$ (exhibiting the same mixed-valence and Verwey-type behavior as the Sm-based samples). Using expression (6) and by noting that each mole of $BaSmFe_2O_{5.0}$ contains 2 moles of Fe we get S = 11.52 J/molK in rather good agreement with the experimental result.

The magnitude of the calculated entropy change shows that a combinatorial entropy calculation assuming a zeroth-order independent cation distribution works surprisingly well for the present system. It is true that Ca substitution leads to a faster decrease of T_V than observed in our theoretical model. In order to account for this fact more elaborate calculations, taking into account local chemistry around the Ca atoms, should be employed. Although, such *e.g.* DFT calculations would provide additional insight into the Verwey-type transition of the present phase, the basic nature of the Verwey-type transition is now rather well established contrary to the still rather controversial behavior of Magnetite.

5.3 Conclusion

For the $Ba(Sm,Ca)Fe_2O_{5+\delta}$ oxygen-deficient double-perovskite system, Ca substitution and O doping were performed in order to study their influences on the valence-fluctuation and the MR property. It was revealed that, although the average oxidation state of Fe increased through the both doping schemes, Ca substitution suppressed the Verwey-type transition temperature more strongly. The two oxidation schemes affected the coordination numbers of the Fe species in different manners. It was found that the transition temperature is dependent on the balance in the amounts of five-coordinated Fe^{III} and five-coordinated Fe^{II}, whereas six-coordinated Fe^{III} bears little or no impact on the formation of the mixed-valence state.

Chapter 6. Iso-Valent Substitution Schemes

6.1 Introduction

In this *A*-site ordered double perovskite structure, there are two different *A*-site, *i.e. A*- and *A*'-site. The plane with *A*-site (*A*O plane), *i.e.* Ba site, has no oxygen deficiency, on the other hand, the plane with *A*'-site (*A*'O_δ plane), *i.e. RE* site, has oxygen deficiency.

In this chapter it is discussed that how the Verwey-type transition is affected by these two different isovalent substitution schemes, *i.e.* by partial Sr-for-Ba substitution and complete occupation of the rare-earth element site by different rare earth elements (Fig. 6.1.1) [VIII]. To simplify the discussions, for both substitution systems, δ was fixed to 0. And *RE* is fixed to Sm for Sr substituted systems.

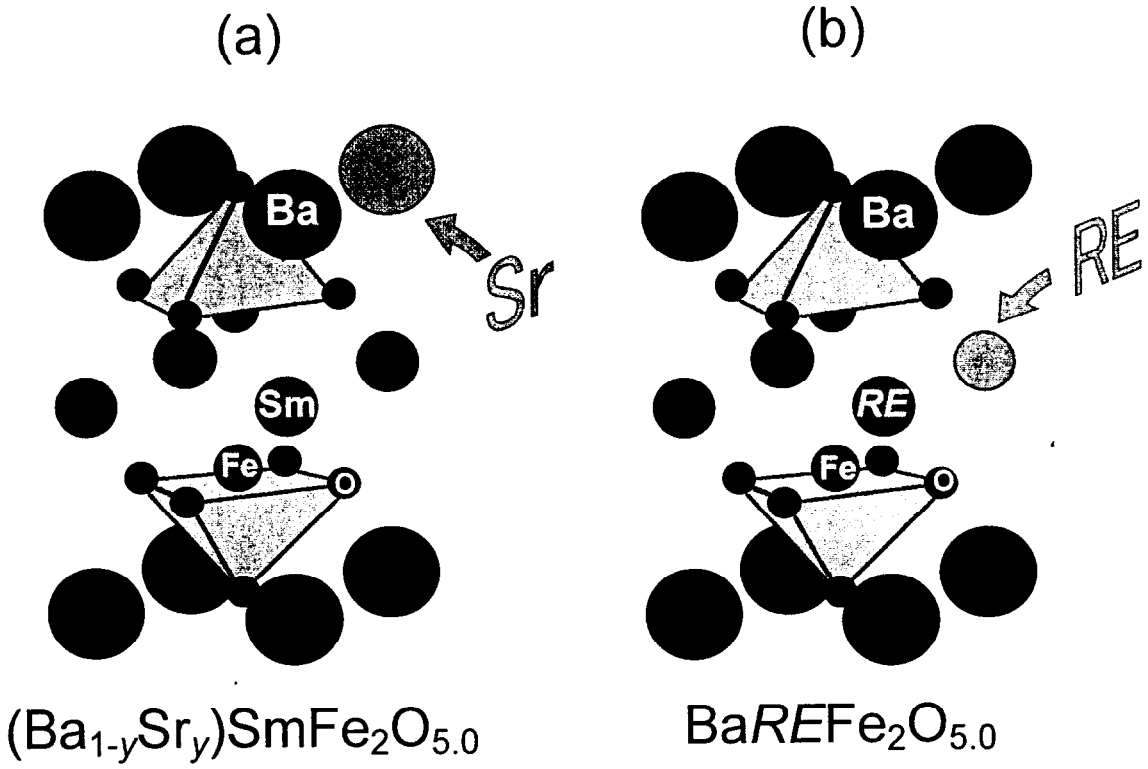

Fig. 6.1.1: A schematic illustration of (a) $(Ba_{1-y}Sr_y)SmFe_2O_{5.0}$, and (b) Ba*RE*$Fe_2O_{5.0}$ samples.

6.2 Results and Discussions

6.2.1 Change in the Lattice Parameters

All the samples were annealed in a 5 % H_2/Ar gas mixture, then controlled to $\delta \approx 0.0$ (See Experimental part). And also the data using synchrotron powder x-ray diffraction were used, then those data were analyzed by Rietveld refinement (Fig. 6.2.1). All the samples were fitted by *Pmmm* as a space group, which has been established to apply above T_V for $\delta \approx 0.0$ samples.

Fig. 6.2.2 (a) and (b) are for the lattice parameter change of $(Ba_{1-y}Sr_y)SmFe_2O_{5.0}$ and $BaREFe_2O_{5.0}$, respectively. These data were collected at room temperature (~ 300 K). In the case of Sr substitution, the change in the lattice parameter is not so big, and the orthorhombicity seems to become smaller with increasing Sr-substitution level. On the other hand, in the case of *RE* substitution, the lattice parameters of *a*-, *b*- and *c*-axis become shorter for smaller *RE* ion, and also the degree of orthorhombisity increase. The change of *c*-axis parameter was larger than the change of *a*- and *b*-axis parameters. This seems to be reasonable, because *a*- and *b*- axis parameters rather depend on the size of BaO plane, and *c*-axis parameter changes easily with *RE* ionic radius.

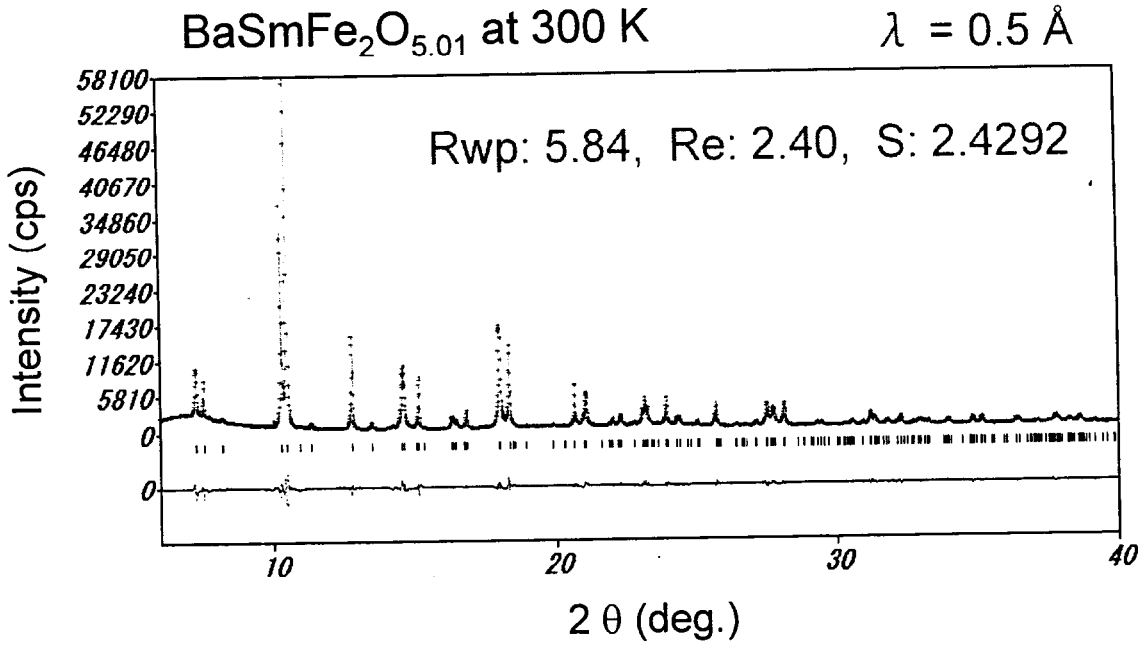

Fig. 6.2.1: Fitted data of synchrotron powder x-ray diffraction for $BaSmFe_2O_{5.01}$ at 300 K.

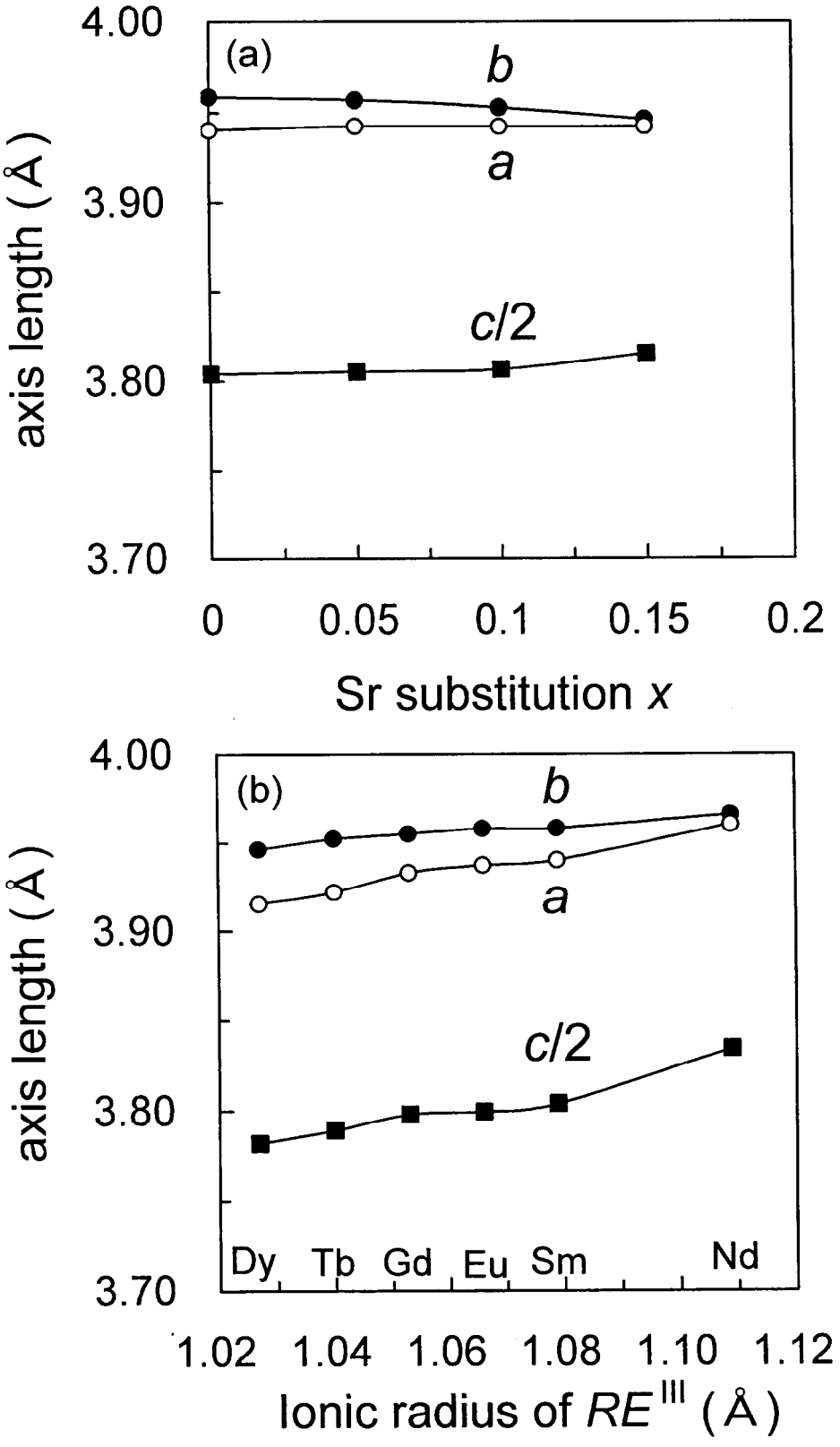

Fig. 6.2.2: Lattice parameter change for (a) $(Ba_{1-y}Sr_y)SmFe_2O_{5.0}$ and (b) $BaREFe_2O_{5.0}$ (*RE* = Dy, Tb, Gd; Eu, Sm, Nd) samples at 300 K.

6.2.2 The Change of T_V

In the resistivity measurements, the jump related to the Verwey-type transition is seen for all the samples (Fig. 6.2.3 (a) and (b)). Some samples exhibit a smaller change at higher temperature than T_V, where the premonitory transition occurs, which is explained in Chapter 7. To compare how the T_V is affected by these two substitution schemes, T_V was first plotted against the ionic radius for the two cation sites in Fig. 6.2.4. In the case of *RE* substitution, T_V increases with decreasing *RE* ionic radius. But for the Sr substitution case the trend seems to be opposite. In other words, T_V goes down with decreasing ionic radius at the Ba,Sr site. This behavior is not explained simply by a size effect. Here for the *RE* = Nd sample the T_V value seems to be a little bit low. This will be discussed later. Any way to explain this behavior, the structure analyses were carried out using the synchrotron powder XRD data collected at 300 K.

Fig. 6.2.5 shows roughly the changes in atomic positions. Here the solid arrows indicate the direction and degree of motions. As you can see, the change between Fe atoms across the *RE* layer (Fe-Fe distance) is larger than the other changes, when smaller *RE* and Sr substitution enhance. This Fe-Fe distance seems to be main parameter, so the Fe-Fe distances were plotted against T_V for both systems (Fig. 6.2.6). It was revealed that the T_V value increases as the Fe-Fe distance become shorter. Here *RE* = Y sample is not in this Figure, because T_V is 307 K (in the cooling process), so the charge-ordered state has already appeared at this temperature region, where the structural parameter is quite different (see in Chapter 7). And also this trend shows relatively good linear behavior. Only the *RE* = Nd sample is not on this line. One of this reason seems to be relating to the different crystal structure between *RE* = Nd and other *RE* samples at the temperature below T_V (charge-ordered state), which are reported by Karen *et al.* (Fig. 6.2.7) [40]. For *RE* = Nd sample the crystal structure is a little bit distorted below T_V. Another possibility to explain the reason is existence of disorder between Ba and Nd, which sometimes occurs because of the similarity of the ionic radius (Nd^{III}: 1.109 Å at *CN* = 8 and 1.27 Å at *CN* = 12, Ba^{II}: 1.42 Å at *CN* = 8 and 1.61 Å at *CN* = 12 [102]). But it may be needed further consideration about this thing.

Further structural analyses were carried out, and four parameters, which seem to affect T_V, were picked out, *i.e.* the Fe-Fe distance (L_1), between Fe atoms through O atom in FeO_2 plane (L_2), across the BaO layer (L_3), and the buckling angle (θ) (Fig. 6.2.8), and they were plotted

(Fig. 6.2.9). Here the crystal structure is orthorhombic at 300 K (above T_V) for all the samples, so the plots were done for that of *a*- and *b*-axis directions. The dashed lines for Ba*RE*$Fe_2O_{5.0}$ samples are due to the reason as mentioned before (for *RE* = Nd sample). To see a relation between these parameters and T_V, the figures were drawn (Fig. 6.2.10 and Fig. 6.2.11). In these figures, L_1 *vs.* T_V and L_3 *vs.* T_V are in a linear relation. But we concluded as the most effective parameter on T_V was L_1, which was much linear relation than L_3's.

The Fe-Fe distance (L_1) is confirmed as the important parameter on T_V. This would mean that the interaction between the FeO_2 planes across the *RE* layer influences the stability of the charge-separated phase. As mentioned in Chapter 4, Karen *et al.* reported that the interaction between FeO_2 planes change from "antiferomagnetically" to "feromagnetically" with heating through T_V. There is possibility that this kind of interaction affects on T_V. This behavior is still in discussion.

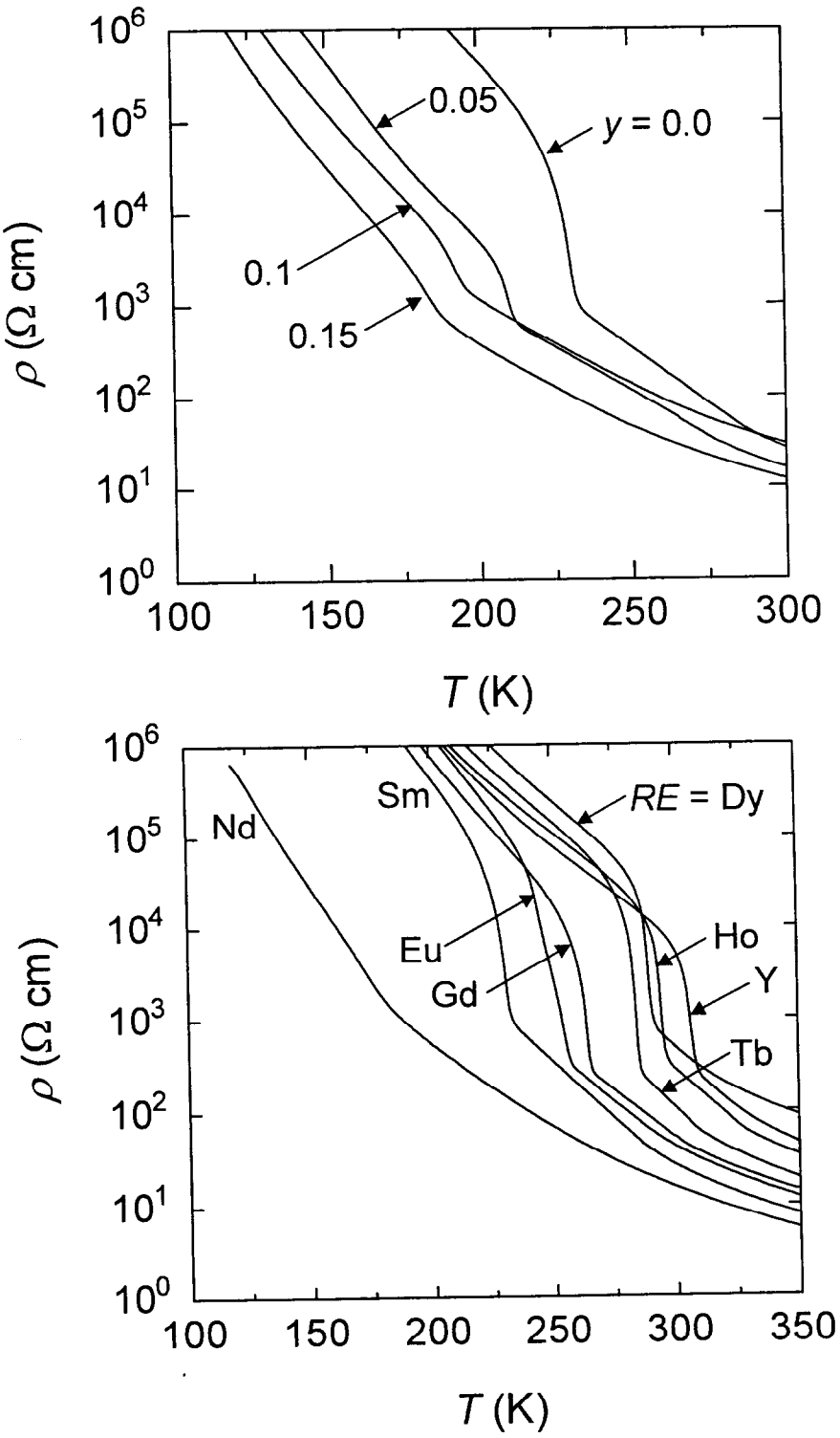

Fig. 6.2.3: Resistivity (ρ) *vs.* Temperature (T) for: (a) $(Ba_{1-y}Sr_y)SmFe_2O_{5.0}$ and (b) $BaREFe_2O_{5.0}$ (*RE* = Ho, Y, Dy, Tb, Gd, Eu, Sm, Nd) in the cooling process.

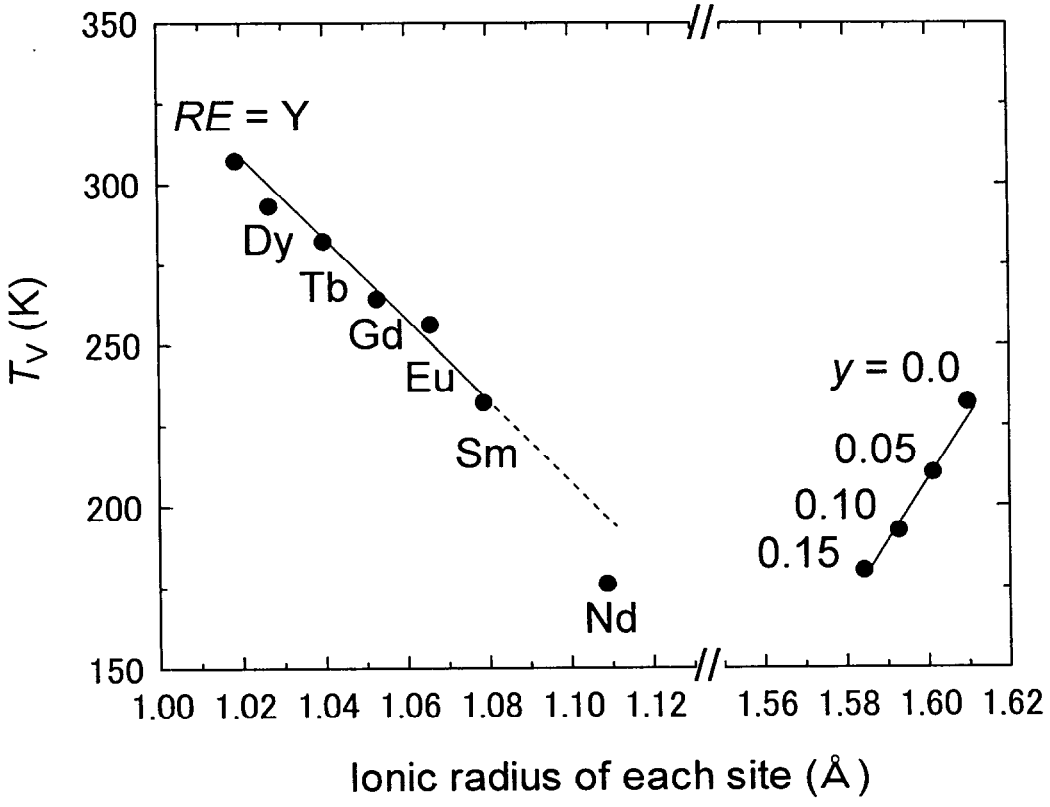

Fig. 6.2.4: T_V *vs.* Ionic radius of each site. Left part is for Ba*RE*$Fe_2O_{5.0}$, right part is for $(Ba_{1-y}Sr_y)SmFe_2O_{5.0}$ samples. The T_V was determined by MR peak in the cooling process (see text in Chapter 4).

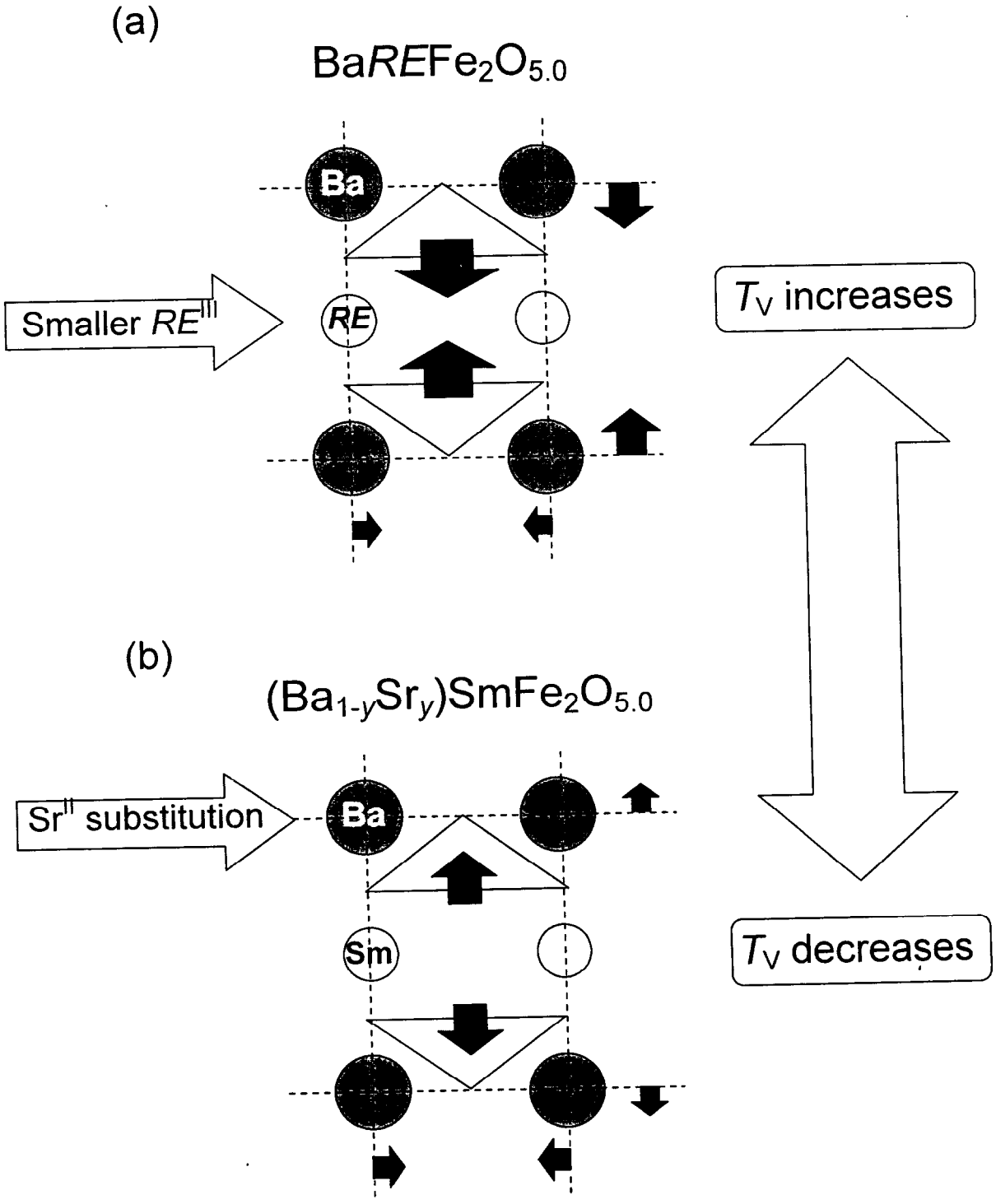

Fig. 6.2.5: The changes in atomic positions in: (a) smaller RE^{III} and (b) Sr^{II} substitution case. The solid arrows indicate the direction and degree of motions.

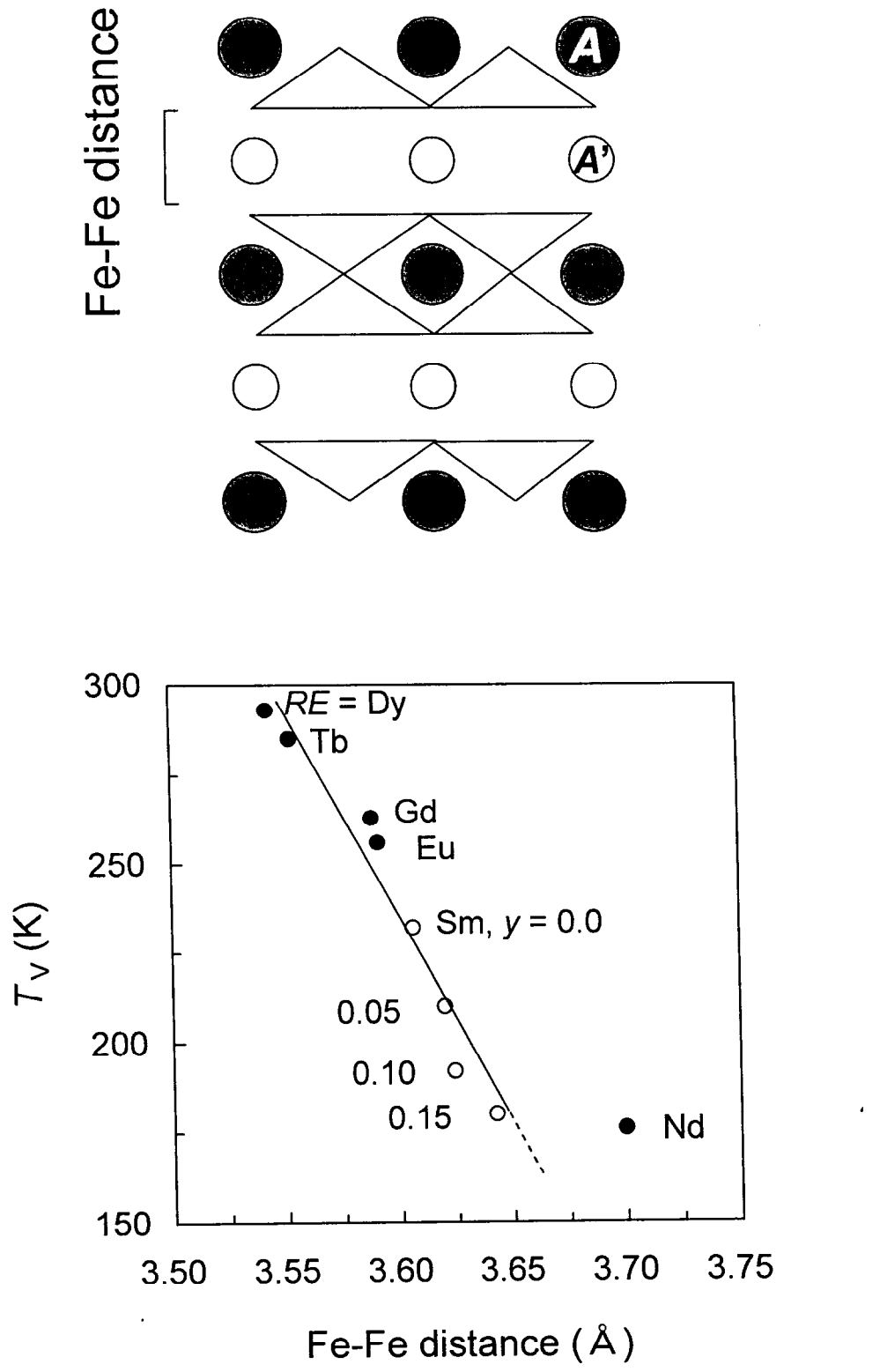

Fig. 6.2.6: T_V *vs.* Fe-Fe distance over the *RE* layer for Ba*RE*$Fe_2O_{5.0}$ (solid circle) and $(Ba_{1-y}Sr_y)SmFe_2O_{5.0}$ (open circle) samples. Top picture indicates an *A*-site ordered double perovskite.

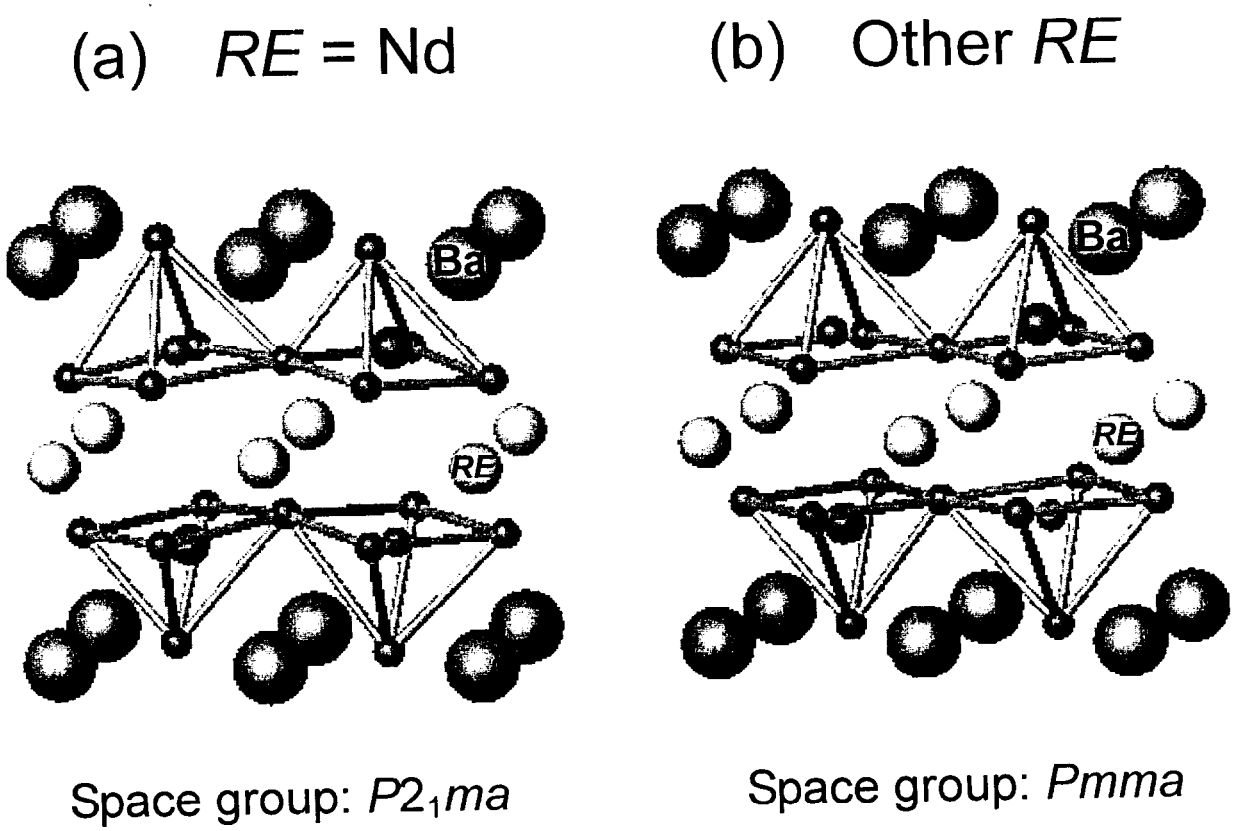

Fig. 6.2.7: The crystal structure of Ba*RE*Fe$_2$O$_{5.0}$ for; (a) *RE* = Nd sample and (b) other *RE* samples below T_V (charge-ordered state) reported by Karen *et al.* [39,40]. Small and large Fe atoms indicate Fe^{III} and Fe^{II}, respectively. For *RE* = Nd sample the crystal structure is a little bit distorted compared with that for other *RE* samples.

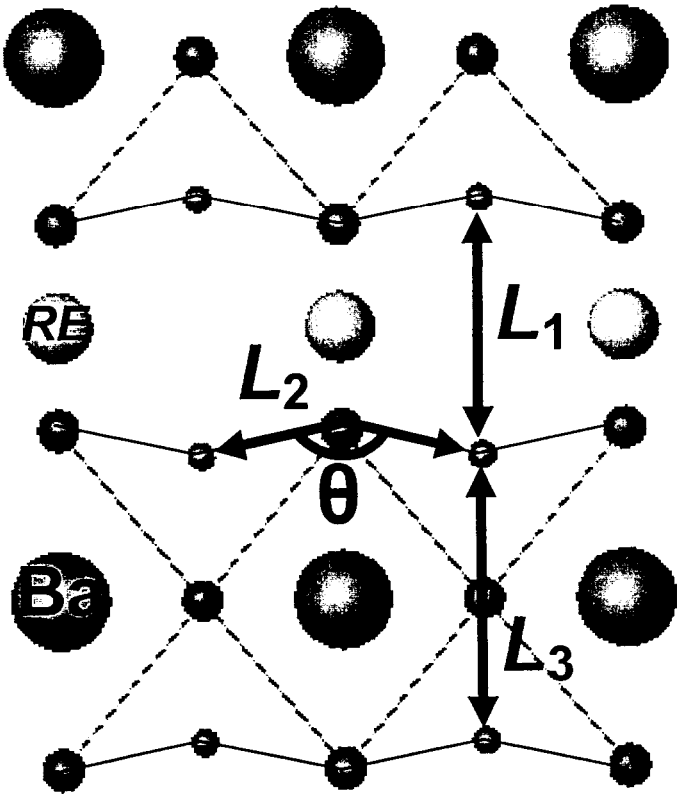

Fig. 6.2.8: A schematic illustration of the *A*-site ordered double perovskite structure. L_1, L_2, L_3, and θ are indicating the Fe-Fe distance, the length between Fe atoms through O atom in FeO_2 plane, and the buckling angle, respectively.

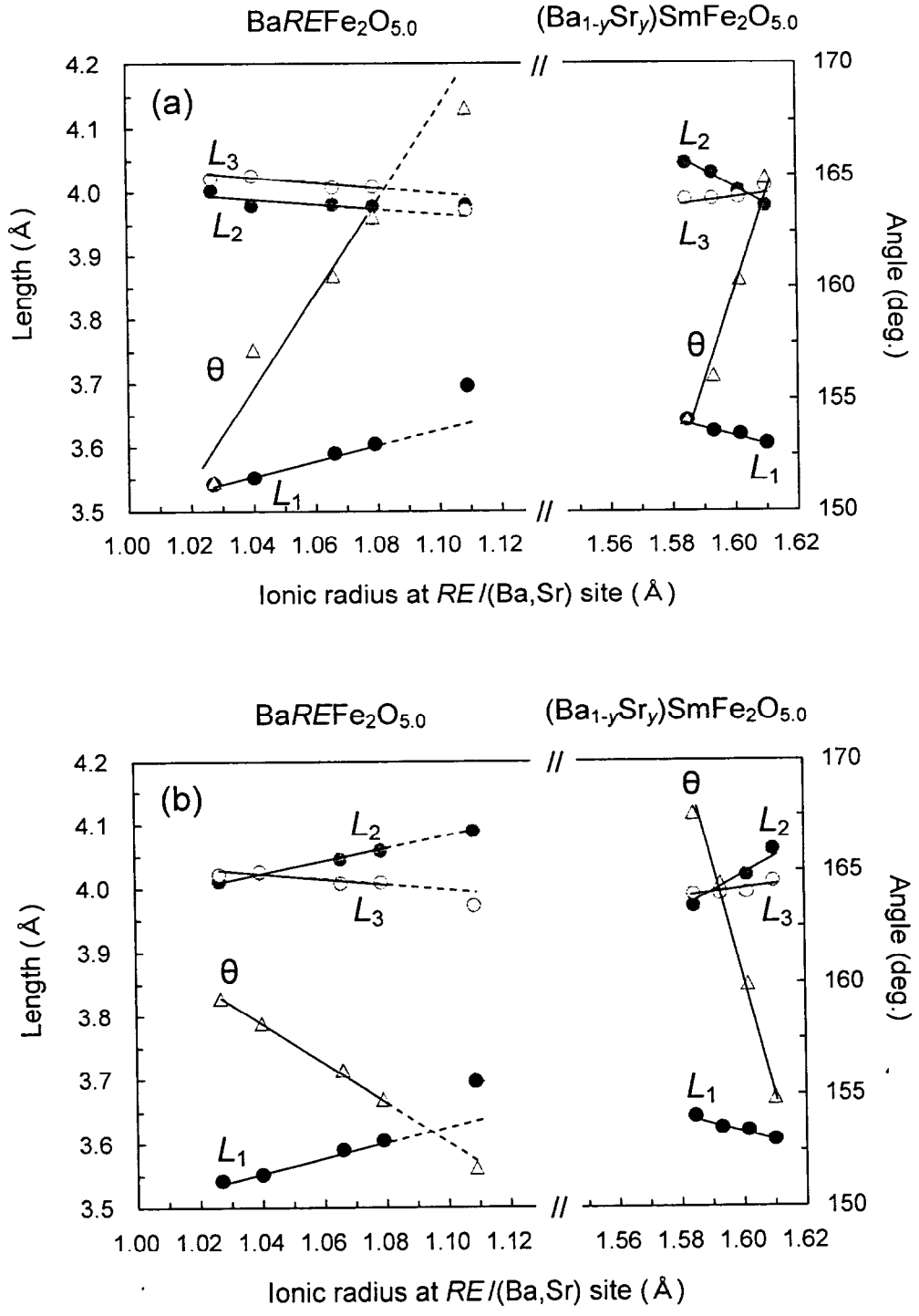

Fig. 6.2.9: L_1, L_2, L_3, and θ *vs.* ionic radius at *RE*/(Ba,Sr) site for; (a) *a*-axis direction and (b) *b*-axis direction. The dashed lines for Ba*RE*$Fe_2O_{5.0}$ samples are due to the reason as mentioned before (for *RE* = Nd sample).

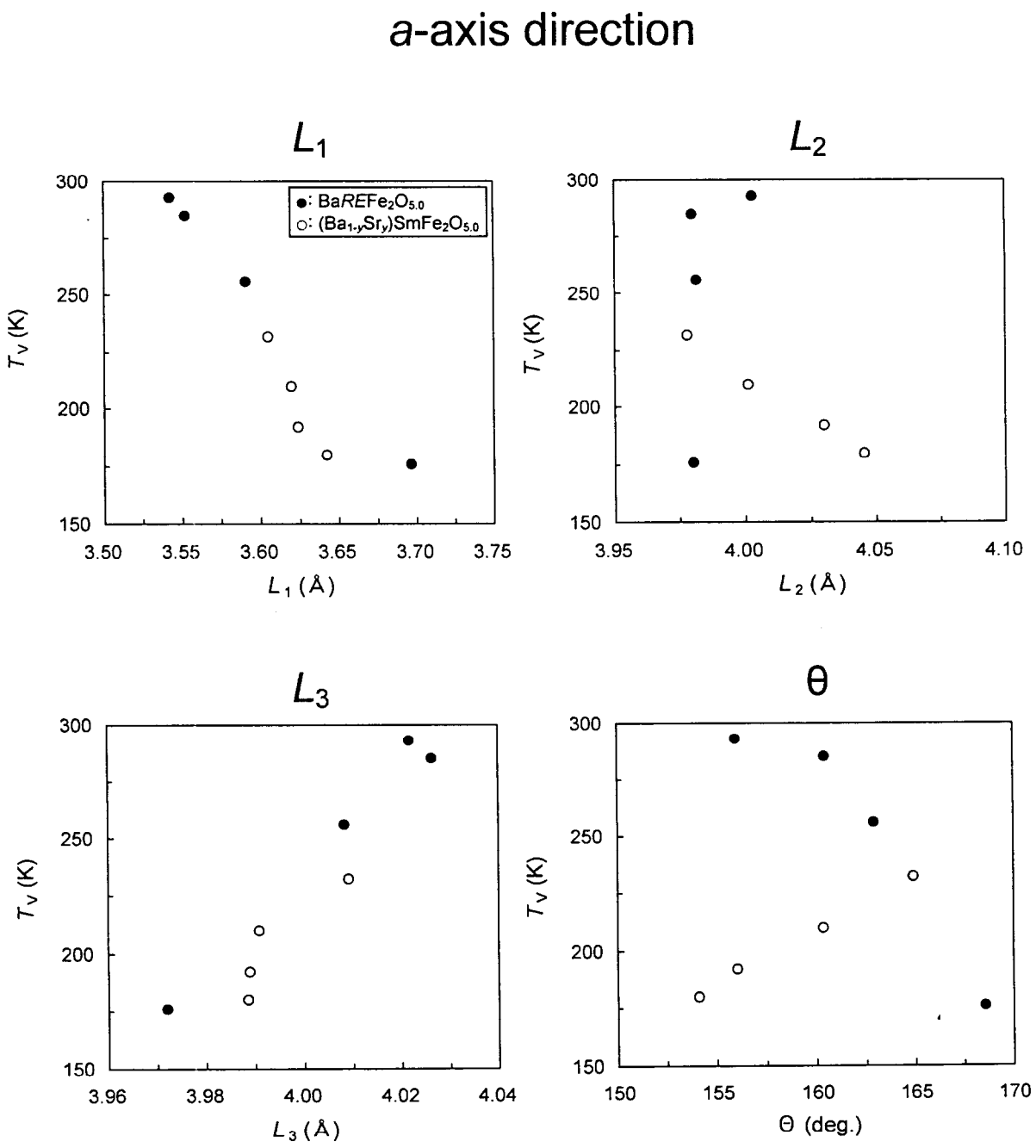

Fig. 6.2.10: L_1, L_2, L_3, and θ *vs.* T_V for Ba*RE*Fe$_2$O$_{5.0}$ (solid circle) and (Ba$_{1-y}$Sr$_y$)SmFe$_2$O$_{5.0}$ (open circle) samples for *a*-axis direction.

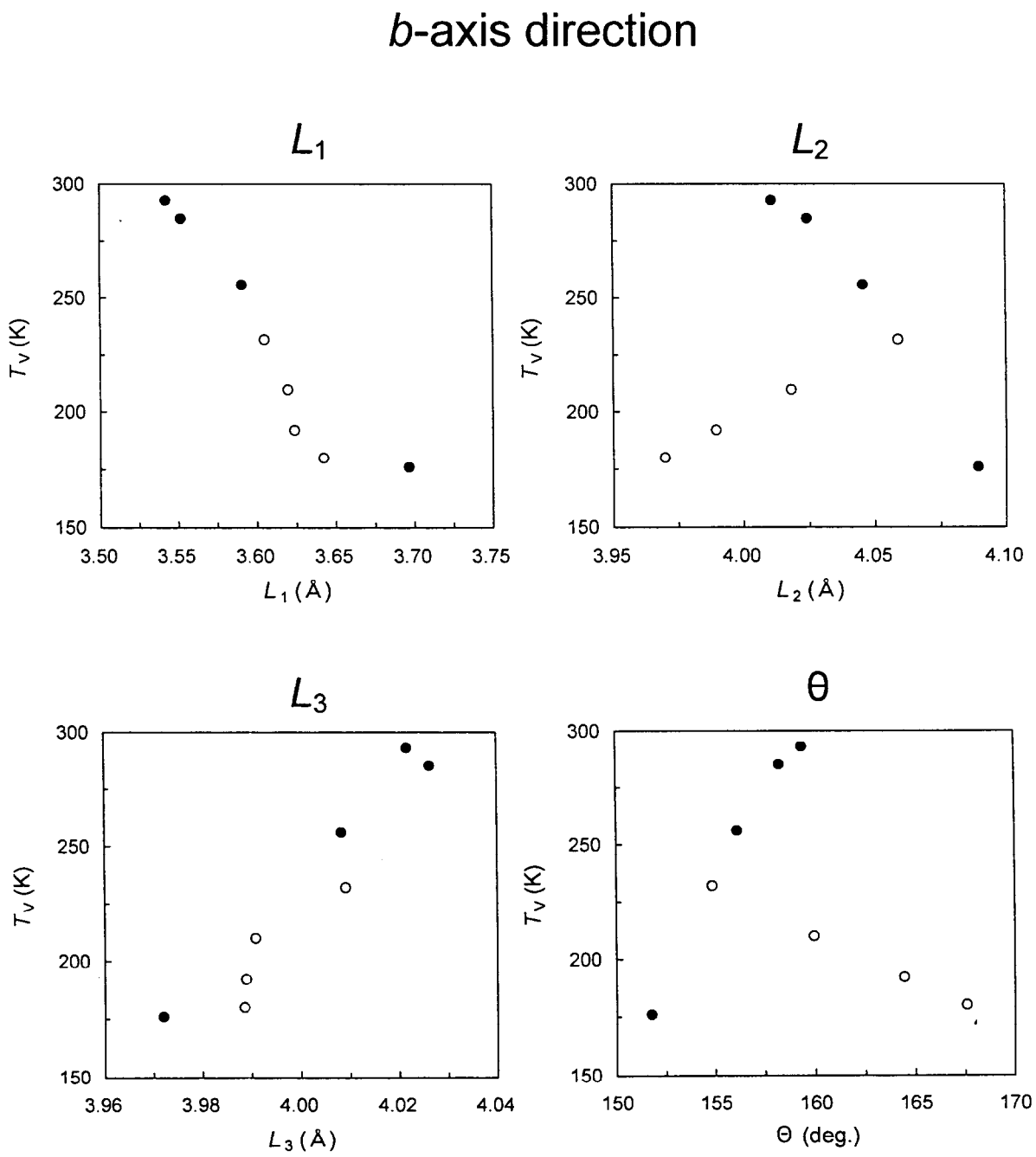

Fig. 6.2.11: L_1, L_2, L_3, and θ *vs.* T_V for Ba*RE*$Fe_2O_{5.0}$ (solid circle) and $(Ba_{1-y}Sr_y)SmFe_2O_{5.0}$ (open circle) samples for *b*-axis direction.

6.3 Conclusion

The effects of the two independent iso-valent substitution shemes, *i.e.* (i) Sr-for-Ba substitution in $(Ba_{1-y}Sr_y)SmFe_2O_{5.0}$ and (ii) occupation of the *RE* site by different *RE* ions in $BaREFe_2O_{5.0}$, on the value of T_V were studied.

It was revealed that, being common for both iso-valent substitution schemes, the T_V value is linearly dependent of the Fe-Fe distance across the *RE* layer. That is, T_V increases as the Fe-Fe distance across the *RE* layer becomes shorter. The linear dependence would mean that the interaction between the FeO_2 planes across the *RE* layer influences the stability of charge mixing-separation transition.

Chapter 7. Charge Ordering and Premonitory Transition

7.1 Introduction

The charge-order super-structure (COSS) between Fe^{II} and Fe^{III} was reported by Karen *et al.* for $BaTbFe_2O_{5.0}$ samples (Fig. 7.1.1 (a)), which was observed by synchrotron x-ray powder diffraction and Neutron powder diffraction [39]. Already it has confirmed by Mössbauer spectra that the charge separation of Fe^{II} and Fe^{III} occurs at T_V, but the observation of the charge ordering was the first time. That charge ordering pattern was the same with the Co-based double-perovskite $BaRECo_2O_{5.0}$.

In addition, another transition was observed which was called as premonitory transition (transition temperature T_p) [39-40,VI]. The T_p was just above T_V (Fig. 7.1.1 (b)). At this transition the iron valences separate from $Fe^{2.5+}$ to $Fe^{2.5+\varepsilon}$ and $Fe^{2.5-\varepsilon}$ with decreasing temperature, and the resistivity shows a small increase. So the charge separation occurs in two steps.

In this chapter, it was studied that the dependence of the *RE* ionic radius on the charge ordering and premonitory transition in the $BaREFe_2O_{5.0}$ samples.

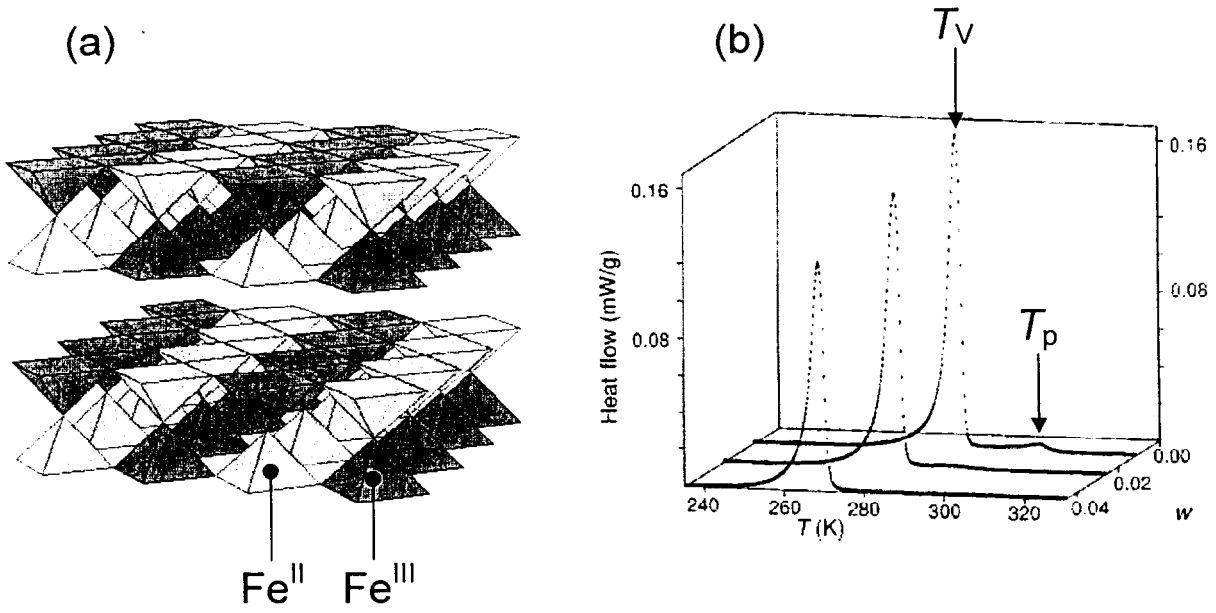

Fig. 7.1.1: The reported phenomenon by P. Karen *et al.* [39] for $BaTbFe_2O_{5+\delta}$ sample. (a) COSS between Fe^{II} and Fe^{III} below T_V. (b) Endothermal caloric effects of the Verwey-type transition and premonitory transition as seen by DSC upon heating.

7.2 Results and Discussions

7.2.1 Charge Ordering

TEM observation was carried out for Ba*RE*$Fe_2O_{5.0}$ sample (*RE* = Y, T_V = 307 K). Fig. 7.2.1 (a) and (b) are those electron diffraction (ED) patterns as temperature decreased beneath T_V with (1 $\bar{1}$ 0) incident beam. The super spots which are nothing above T_V are appeared below T_V. These super spots are obviously related to Verwey-type transition. The reason of appearance of super spots is considered as the ordering between two different FeO_5 pyramids are formed by ordering of Fe^{II} and Fe^{III} below T_V. In addition, the super spots are not in the diffraction of the *a-b* plane below T_V (Fig. 7.2.2 (a)). From these diffraction patterns, the COSS below T_V was set as illustrated in Fig. 7.2.2 (c), *i.e.* the pyramid including Fe^{II} atom or Fe^{III} are alternating as doubling in *a-b* plane and single along *c* axis.

As mentioned before, Karen *et al.* reported the COSS for the Ba*RE*$Fe_2O_{5.0}$ (*RE* = Tb) as illustrated in Fig. 7.2.2 (d) which were determined by synchrotron powder XRD and synchrotron powder diffraction [39]. This mode is different to the mode for *RE* = Y sample. This indicates that the charge ordering mode is possible to change with *RE* ionic radius in the Ba*RE*$Fe_2O_{5.0}$ samples. However it should be noticed that the super spots in the ED pattern are not sometimes appeared, *i.e.* the reproducibility is not so good. So far this reason is considered as the change of excess oxygen amount in the samples, which causes the possibility of disappearance of super spots. Actually it took for a long time until the ED observation was done, and it would be enough time to change the excess oxygen amount. Also in the synchrotron powder XRD measurements, no super peak was observed for the *RE* = Y sample. In this case also it took a long time until the measurement was done. This should be improved in the future. Another thing which indicates the possibility to change the structural parameter related to the *RE* ionic radius is the Fe-Fe distance over the *RE* layer. In Fig. 7.2.3 shows the change of the *a*-,*b*-,*c*-parameter and Fe-Fe distance over the *RE* layer against temperature. These data are from synchrotron powder XRD and refined using space group of Pmmm which is for the orthorhombic (not for the charge ordered structure). These parameters in the figures become shorter entirely as the *RE* ionic radius decreases. But *RE* = Y sample shows increase in Fe-Fe distance over the *RE* layer. This might be said that it is some changes occur in the structure with *RE* ionic radius.

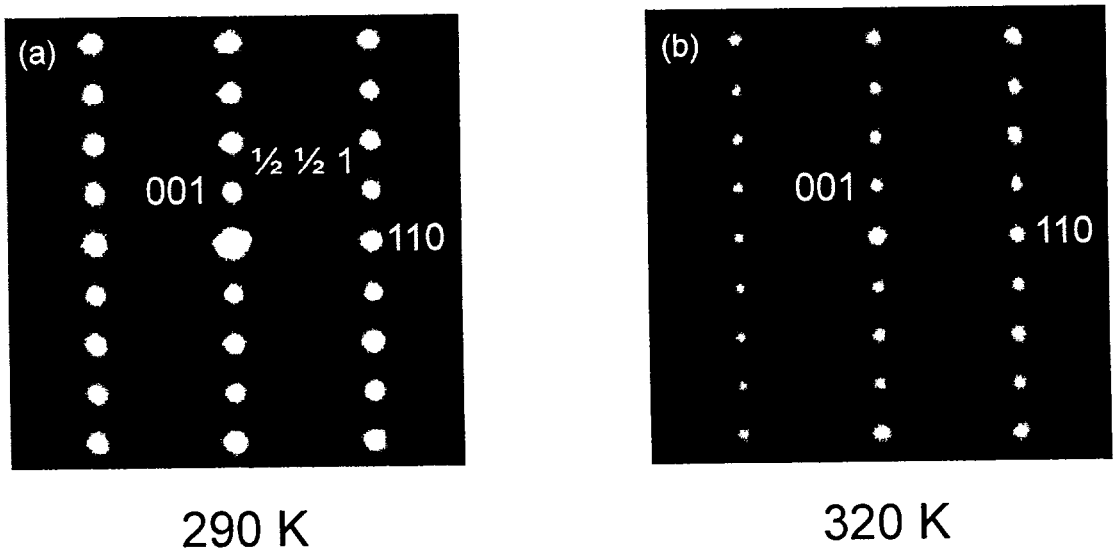

Fig. 7.2.1: Electron diffraction pattern for $BaYFe_2O_{5.0}$ sample (T_V = 307 K) with (1 $\bar{1}$ 0) incident beam. (a) The super spots appear below T_V, (b) The super spots are nothing above T_V.

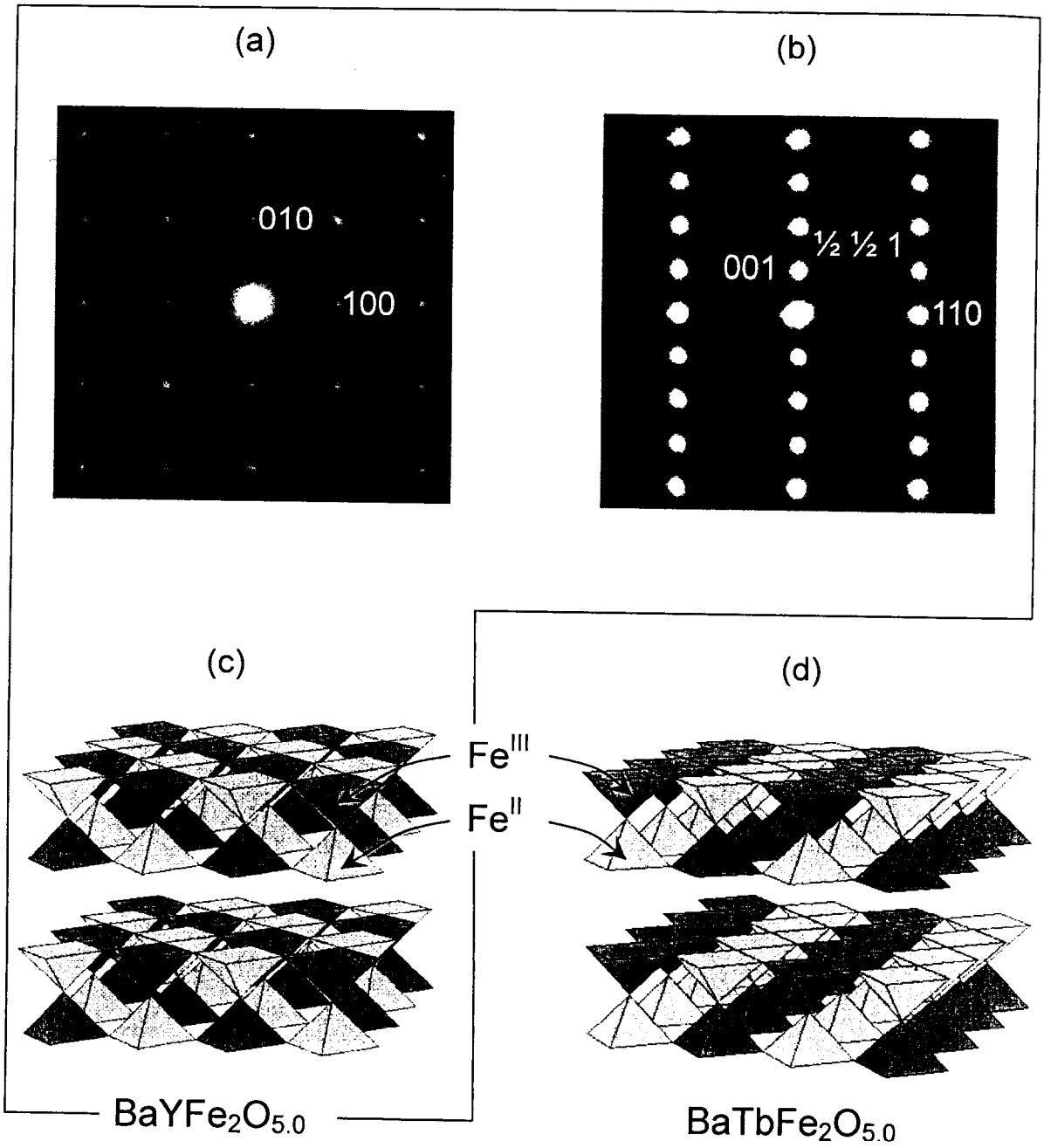

Fig. 7.2.2: (a) and (b): ED patterns in *a-b* plane and vertical plane to the *a-b* plane, respectively for the $BaYFe_2O_{5.0}$ sample at 290 K (below T_V). (c) and (d): COSS for $BaYFe_2O_{5.0}$ and $BaTbFe_2O_{5.0}$ [39] samples, respectively below T_V.

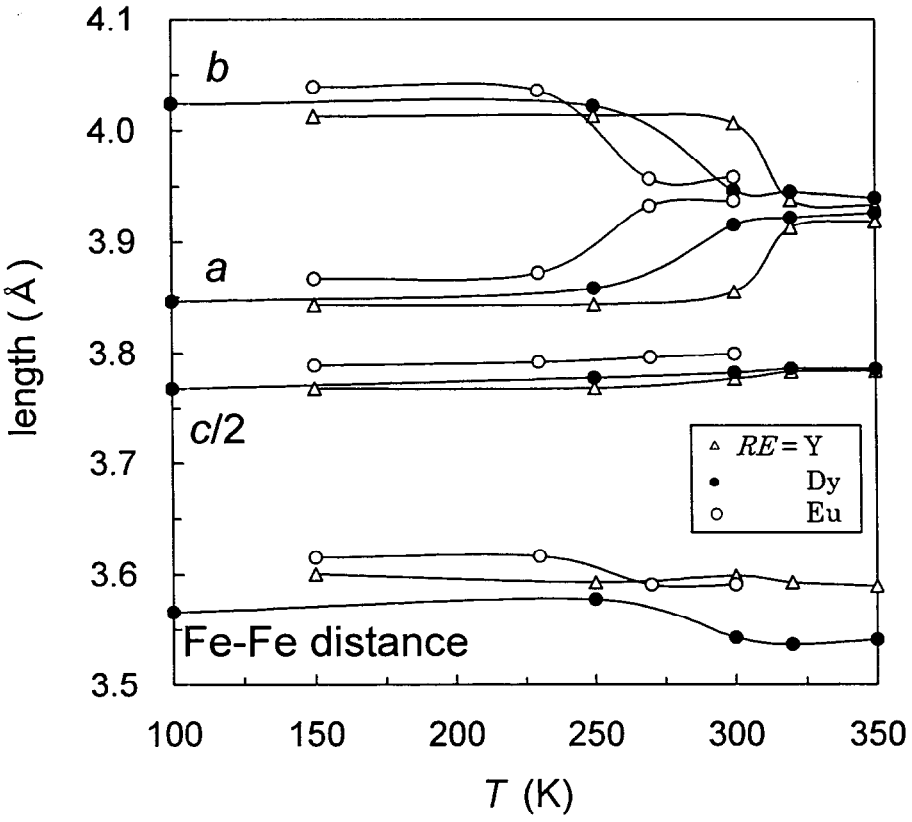

Fig. 7.2.3: Temperature *vs.* the length of *a*-, *b*-, *c*/2-axis and Fe-Fe distance over the *RE* layer in the $BaREFe_2O_{5.0}$.

7.2.2 Premonitory Transition

The premonitory transition is also sensitive to the amount of excess oxygen, *i.e.* T_p can be observed only in the Ba*RE*$Fe_2O_{5+\delta}$ ($\delta \approx 0$). All the samples which were used here were controlled to $\delta \approx 0$ by means of post annealing. The resistivity measurements for the Ba*RE*$Fe_2O_{5.0}$ samples are shown in Fig. 7.2.4 (a). The signal of the premonitory transition can be seen at the bending point just above T_V, which is more clearly observed in the differential ρ curves (Fig. 7.2.4 (b)). In the sample for *RE* = Nd which has large *RE* ionic radius, the premonitory transition is quite small or almost noting. The T_p and T_V value are plotted against *RE* ionic radius in Fig. 7.2.5. It is appeared that the hatched region ($T_p - T_V$) is decreasing as *RE* ionic radius decreases. This means that the charge-mixing/separation transition is easier to occur at once in the smaller *RE* samples like *RE* = Y and Dy. This reason is in question at this moment, but the interaction over the *RE* layer would play some roles to stabilize the charge separated/ordered phase.

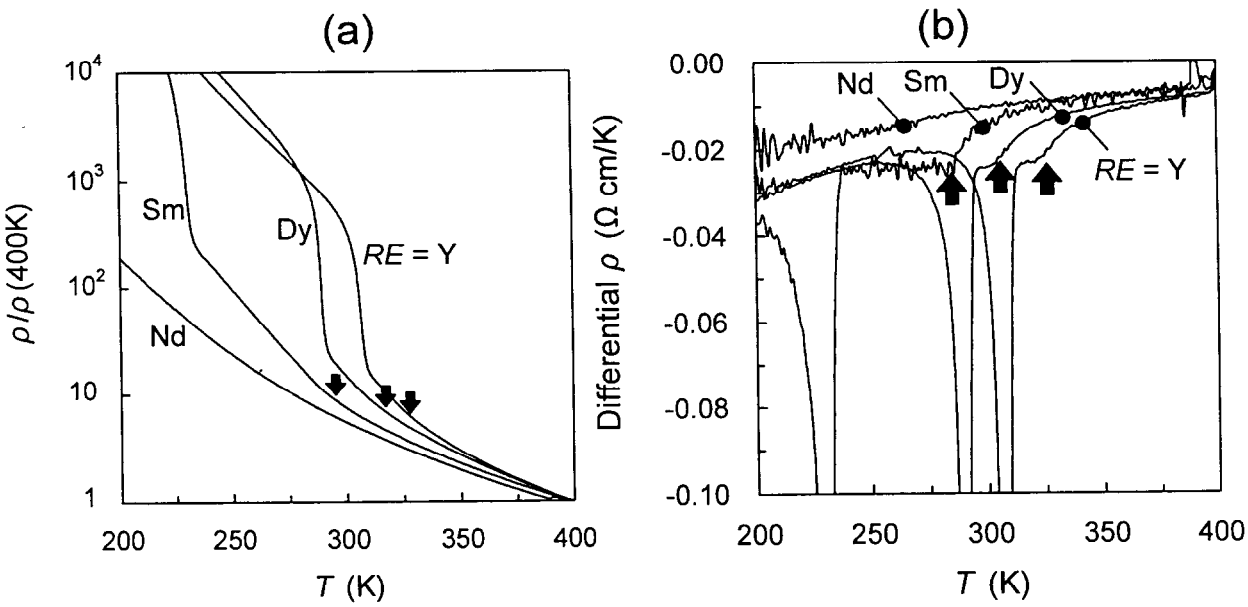

Fig. 7.2.4: The curves for Ba*RE*$Fe_2O_{5.0}$ (*RE* = Y, Dy, Sm, Nd) of: (a) The resistivity normalized at 400 K *vs.* temperature, and (b) Differential curve of resistivity *vs.* temperature. The arrows show the premonitory transition.

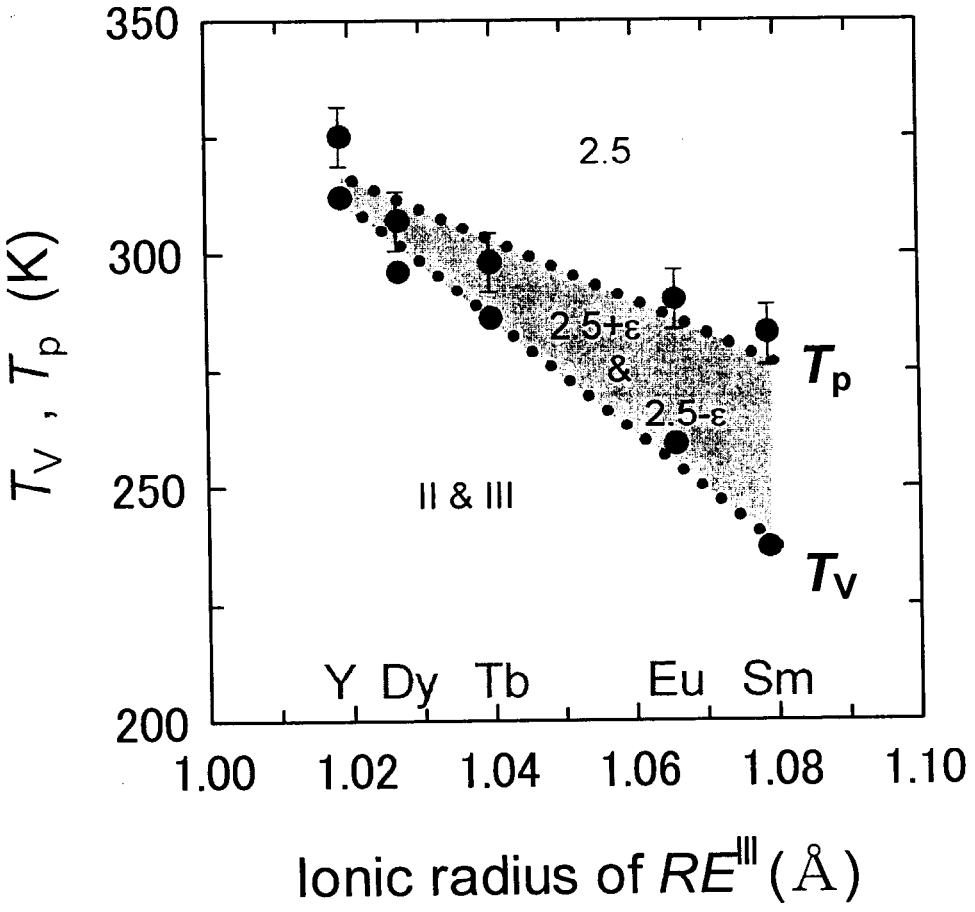

Fig. 7.2.5: T_V and T_p *vs.* ionic radius of RE^{III} for Ba*RE*Fe$_2$O$_{5.0}$ samples. The number in the figure, *i.e.* "2.5+", "2+ε & 3–ε", "II & III", indicate the valence of iron in the samples.

7.3 Conclusion

In a $BaYFe_2O_{5.0}$ sample, super spots due to charge ordering between Fe^{II} and Fe^{III} were observed by electron diffraction. The charge-order super-structure (COSS) as derived from the electron diffraction pattern was different from that reported for $BaTbFe_2O_{5.0}$ by Karen *et al.* [39]. This suggests that the COSS in $BaREFe_2O_{5.0}$ may be changed with the change in *RE* ionic radius. Observation of super spots by electron diffraction was not quite reproducible. This may be due to slight differences in the amount of excess oxygen in different samples.

Premonitory transition (at T_p) was studied by means of DSC and resistivity. In Fig. 7.2.6, phase relations in terms of temperature and the *RE* ionic radius are summarized, *i.e.* a figure in the vicinity of T_V and T_p is constructed.

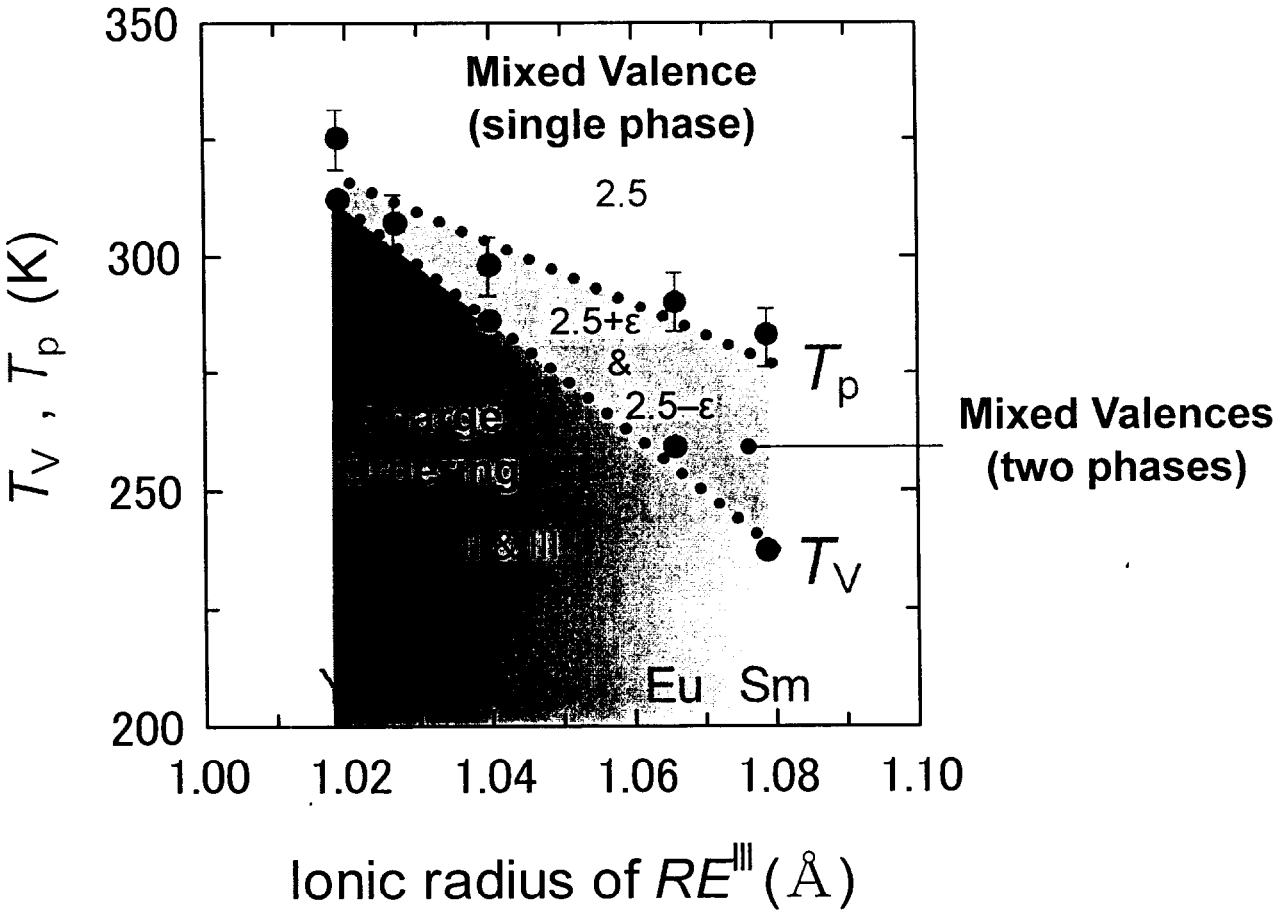

Fig. 7.2.6: A figure related to charge mixing/separation-ordering for $BaREFe_2O_{5.0}$ samples.

Chapter 8. Suggestions for Future Works

• Half-metallic property

In the related iron oxides, Fe_3O_4 and Sr_2FeMoO_6, iron atoms posses the mixed-valent II/III state. Both phases are also regarded as half-metallic materials. Therefore it was considered how to have the half-metallicity in the *A*-site ordered double-perovskite Ba*RE*$Fe_2O_{5+\delta}$. From a band structure calculation, it was suggested that if Ba*RE*$Fe_2O_{5+\delta}$ becomes ferromagnetic, there is the possibility for half-metallicity. Fig. 8.1 shows the calculation results for "ferromagnetic $BaYFe_2O_{5.0}$". For the down spin, the t_{2g} band (derived from the *xy* orbital) crosses Fermi level (E_F), while for the up spin, the e_g band (derived from the $x^2 - y^2$ orbital) crosses only slightly E_F. This is an indication of the possibility for half-metallicity. To make the Ba*RE*$Fe_2O_{5+\delta}$, system ferromagnetic, carrier doping like in the manganese oxides, or chemical substitution effects which weakens antiferromagnetic interaction should be taken.

• To clarify the dependence of the charge-ordered structure on the *RE* constituent

As mentioned in chapter 7, observation of super spots for the $BaYFe_2O_{5.0}$ phase by electron diffraction was not quite reproducible. This may be due to slight differences in the amount of excess oxygen in different samples. Actually such a slight change of the amount of excess oxygen occurs sometimes in the samples, and this influences the observation of super spots.

So the improvement of the sample quality in terms of excess oxygen control (δ should be zero) is required. The cerimetric titration method is a simple and effective method to analyze the amount of oxygen.

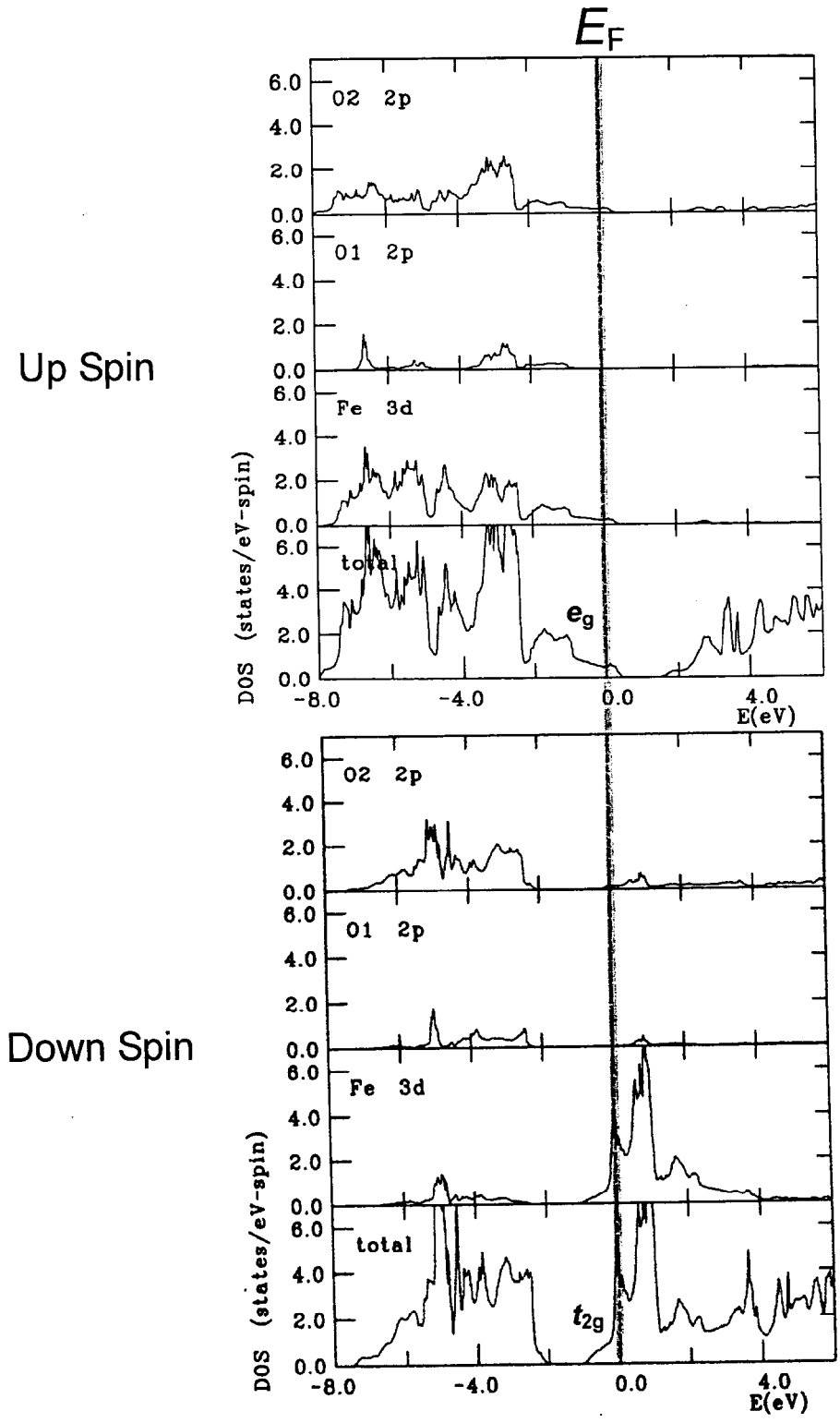

Fig. 8.1: Results of band structure calculation for $BaYFe_2O_{5.0}$ by Hamada *et al.* in Tokyo Univ. of Science. The calculation was performed by assuming that the phase has a ferromagnetic ground state.

• 0112 superconductor

No *A*-site ordered double-perovskite (0112) compounds with the transition metal site occupied by Cu only, *i.e.* Ba*RE*$Cu_2O_{5+\delta}$, do not exist yet. If such a phase were synthesized, chances are that it would be superconducting. In fact, an early effort to extend the solid solubility of Cu at the transition-metal site in the $BaY(Cu_{0.5+x}Fe_{0.5-x})_2O_{5+\delta}$ system found a narrow solubility region around the optimum of equal amounts of Fe and Cu [35]. So far the highest Cu concentration achieved at the *B* site is 70 %: a single-phase sample of $BaY(Cu_{0.7}Fe_{0.3})_2O_{5+\delta}$ was obtained through high-pressure synthesis [36].

So the high-pressure synthesis of Ba*RE*$Cu_2O_{5+\delta}$ seems to be effective, and more efforts should be made in that direction.

• Single crystals

This research was done using polycrystalline samples. But single crystal samples are desired for detailed research. So far the efforts for growing single crystals were done for the $BaSmFe_2O_{5+\delta}$ phase by the floating zone (FZ) method and the traveling solvent floating zone (TSFZ) method using $Ba_2Fe_2O_5$ as a solvent (in a flowing 5 % H_2/Ar gas mixture for both methods), but these did not succeed.

For this phase the phase diagram is not known. So the conditions for the FZ or TSFZ methods should be optimized. Especially a control of the atmosphere would be important. Furthermore, other Ba*RE*$Fe_2O_{5+\delta}$ compositions with different *RE* species should be also tried.

Chapter 9. Summary

In this research, the purpose has been to investigate the peculiar characteristics of the valence mixing-separation transition and the magnetic and magnetotransport properties of the *A*-site ordered double-perovskite systems, (Ba,Sr)(*RE*,Ca)$Fe_2O_{5+\delta}$, in terms of the chemical substitution/doping effects and examine the possibility of appearance of novel functions. The following results have been obtained.

1. Development of new technique for the synthesis of (Ba,Sr)(*RE*,Ca)$Fe_2O_{5+\delta}$ (Chapter 3)

The sample synthesis was carried out by means of a novel oxygen-getter-controlled low-O_2-pressure encapsulation method that was developed during the course of this research. In this synthesis technique, thermodynamical equilibrium of a redox couple is applied. For $(Ba_{1-y}Sr_y)(RE_{1-x}Ca_x)Fe_2O_{5+\delta}$ samples, the reaction of Fe/FeO was utilized with an oxygen partial pressure being expected to equilibrate at 7.6×10^{-16} atm at 985 °C. Under this condition, single-phase samples were obtained for the $Ba(Sm_{1-x}Ca_x)Fe_2O_{5+\delta}$ ($0 \leq x < 0.15$), $(Ba_{1-y}Sr_y)SmFe_2O_{5+\delta}$ ($0 \leq y \leq 0.15$) and $BaREFe_2O_{5+\delta}$ (*RE* = Y, Ho, Dy, Tb, Gd, Eu, Sm, Nd, La) systems. Furthermore by means of various post-annealings, $BaSmFe_2O_{5+\delta}$ ($0 \leq \delta \leq 0.28$) samples were obtained.

2. Discovery of negative magnetoresistance in *A*-site ordered double-perovskite iron-oxide systems (Chapter 4)

Negative magnetoresistance was observed about the transition temperature (T_V) of Verwey-type transition in *A*-site ordered double-perovskite iron-oxide systems. For $BaSmFe_2O_{5+\delta}$, the highest MR value was – 1.4 % for the most reduced sample ($\delta \approx 0.04$). The small MR value is considered as a reflection of a small change in the spin arrangement at T_V. Basically antiferromagnetism is dominant in the FeO_2 planes through out the temperature range of 5 K – 400 K.

3. Understanding of oxidation effect on the Verwey-type transition (Chapter 5)

As two oxidation schemes, (i) oxygen doping to the oxygen vacant site, and (ii) Ca substitution at the *RE* site, were employed in order to clarify the effect of oxidation on the Verwey-type transition and the MR property. It was revealed that, although both doping schemes increased the average oxidation state of Fe, Ca substitution suppressed T_V more strongly. The both oxidation schemes affect the coordination numbers of Fe species in different manners. As a result, it was revealed that the value of T_V is dependent on the ratio of five-coordinated Fe^{III} to five-coordinated Fe^{II}, whereas six-coordinated Fe^{III} bears little or no impact on the formation of the mixed-valence state.

4. Clarification of iso-valent substitution effect on the Verwey-type transition (Chapter 6)

Two different iso-valent substitution schemes were employed to clarify their effects on T_V in the *A*-site ordered iron-based double perovskite system: (i) Sr-for-Ba substitution in $(Ba_{1-y}Sr_y)SmFe_2O_{5.0}$ and (ii) occupation of the *RE* site by different *RE*s in $BaREFe_2O_{5.0}$.

It was revealed that the T_V value is linearly dependent of the Fe-Fe distance across the *RE* layer. In other words, T_V increases as the Fe-Fe distance across the *RE* layer becomes shorter in both iso-valent substitution schemes. This would mean that the interaction between the FeO_2 planes across the *RE* layer directly influences the stability of the phase with $Fe^{2.5+}$ (of a mixed-valence state).

5. Control of the value of T_V in the wide range (Chapter 5 & 6)

In (Ba,Sr)(*RE*,Ca)$Fe_2O_{5+\delta}$ samples, T_V value was controlled in the wide range. The lowest T_V value was 120 K for the $Ba(Sm_{0.925}Ca_{0.075})Fe_2O_{5.0}$ sample. The highest T_V value was obtained for the $BaYFe_2O_{5.0}$ sample at 307 K, *i.e.* above room temperature.

6. Study on the dependences of charge ordering and premonitory transition on *RE* species (Chapter 7)

In $BaYFe_2O_{5.0}$, super-spots due to charge ordering between Fe^{II} and Fe^{III} were observed by electron diffraction. The charge-ordering super-structure (COSS) as derived from the electron-diffraction results was different from the one for $BaTbFe_2O_{5.0}$ reported by Karen *et al.* [39]. This suggests that COSS in $BaREFe_2O_{5.0}$ depends on the *RE* ionic radius. Observation of such diffraction pattern in TEM was not straightforward, which is probably due to small differences in the amount of excess oxygen in different samples.

Furthermore the dependence of the premonitory transition (at T_p) on the *RE* constituent was studied for $BaREFe_2O_{5.0}$ samples, and it was shown that the distance between T_p and T_V decreases as the *RE* ionic radius decreases.

7. Research for the possibility for half-metallicity (Chapter 8)

The possibility of the half-metallicity in *A*-site ordered double-perovskite $BaREFe_2O_{5+\delta}$ was researched. From a band structure calculation, it was suggested that if $BaREFe_2O_{5+\delta}$ becomes ferromagnetic, there is a possibility for half-metallicity.

References

[I] "Magnetoresistance peak in the vicinity of the charge disproportionation/ordering transition in the $R_{1/3}Sr_{2/3}FeO_{3-\delta}$ (R = La, Pr) perovskite",
V. P. S. Awana, **J. Nakamura**, J. Lindén, M. Karppinen and H. Yamauchi, Solid State Commun. **119**, 159-162 (2001).

[II] "Iron mixed-valence compounds, $BaSm(Cu_{0.5+x}Fe_{0.5-x})_2O_{5+\delta}$ I: Synthesis and chemical characterization",
J. Nakamura, J. Lindén, H. Suematsu, M. Karppinen, H. Yamauchi, Physica C **338**, 121-125 (2000).

[III] "Co-existence of Intrinsic and Extrinsic Magnetoresistance in the Double-Perovskite $Sr_2Fe(Mo_{1-x}W_x)O_{6-w}$ System",
J. Lindén, T. Yamamoto, **J. Nakamura**, M. Karppinen and H. Yamauchi, Appl. Phys. Lett. **78**, 2736-2738 (2001).

[IV] "Control of Fe valence state and magnetoresisitance by means of T = Ta and W substitution in $Sr_2Fe(Mo_{1-x}T_x)O_6$",
J. Lindén, T. Yamamoto, **J. Nakamura**, H. Yamauchi and M. Karppinen, Phys. Rev. B **66**, 184408-184414 (2002).

[V] "Magnetoresistance effect in the fluctuating-valence $BaSmFe_2O_{5+w}$ system",
J. Nakamura, J. Lindèn, M. Karppinen and H. Yamauchi, Appl. Phys. Lett. **77**, 1683-1685 (2000).

[VI] **J. Nakamura**, J. Lindèn, P. Karen, H. Yamauchi and M. Karppinen, in preparation.

[VII] "Hole-doping effect on the Verwey-type transition and magnetoresistivity of $Ba(Sm,Ca)Fe_2O_{5+\delta}$",
J. Nakamura, J. Lindèn, H. Yamauchi and M. Karppinen, Solid State Commun. **121**, 269-274 (2002).

[VIII] **J. Nakamura**, H. Yamauchi and M. Karppinen, in preparation.

[1] "Homologous Series of Layered Cuprates",
H. Yamauchi, M. Karppinen and S. Tanaka, Physica C **263**, 146-150 (1996).

[2] "Structural Classification of Superconducting Cuprates",
H. Yamauchi and M. Karppinen, Superlatt. Microstruct. **21A**, 127-152 (1997).

[3] "$YBaCuFeO_{5+\delta}$: A Novel Oxygen-Deficient Perovskite with a Layer Structure", L. Er-Rakho, C. Michel, Ph. Lacorre and B. Raveau, J. Solid State Chem. **73**, 531-535 (1988).

[4] M. Pissas, C. Mitros, G. Kallias, V. Psycharis, A. Shimopoulos, A. Kostikas and D. Niarchos, Physica C **192**, 35 (1992).

[5] M. J. Ruiz-Argon, U. Amador, E. Moran and N. H. Anderson, Physica C **235**, 1609 (1994).

[6] "Mixed Oxides of Cobalt and Copper with a Double Pyramidal Layer Structure", L. Barbey, N. Nguyen, V. Caignaert, M. Hervieu and B. Raveau, Mat. Res. Bull. **27**, 295-301 (1992).

[7] "Spin State and Variation of the Spin Orientation of Co(III) in the 112-Type Phase $YBa(Co_{2-x}Cu_x)O_5$", L. Barbey, N. Nguyen, V. Caignaert, F. Studer and B. Raveau, J. Solid State Chem. **112**, 148-156 (1994).

[8] "Neutron Powder Diffraction Study of the Nuclear and Magnetic Structures of the Oxygen Deficient Perovskite $YBaCuCoO_5$", Q. Huang, P. Karen, V. L. Karen, A. Kjekshus, J. W. Lynn, A. D. Mighell, I. Natali Sora, N. Rosov and A. Santoro, J. Solid State Chem. **108**, 80-86 (1994).

[9] "Magnetic Behavior of the "112" Type Substituted Cuprate $YBaCoCu_{1-x}Fe_xO_5$", L. Barbey, N. Nguyen, A. Ducouret, V. Caignaert, J. M. Grenèche and B. Raveau, J. Solid State Chem. **115**, 514-520 (1995).

[10] "Synthesis and Structural Studies of the Perovskite-Related Compound $YBaCo_2O_{5+\delta}$", W. Zhou, C. T. Lin and W. Y. Liang, Adv. Mater. **5**, 735-738 (1993).

[11] "Solid Solution of $YBaCu_xCo_{2-x}O_5$ ($0 \le x \le 1$) and Its Intergrowth with $YBa_2Cu_3O_7$", W. Zhou, Chem. Mater. **6**, 441-447 (1994).

[12] "Magnetic and M-I Transitions in $YBaCo_2O_{5+x}$ ($0 \leqq x \leqq 0.5$)", D. Akahoshi and Y. Ueda, J. Phys. Soc. Jpn. **68**, 736-739 (1999).

[13] "Structural and Magnetic Studies of Ordered Oxygen-Deficient Perovskites $LnBaCo_2O_{5+\delta}$, Closely Related to the "112" Structure", A. Maignan, C. Martin, D. Pelloquin, N. Nguyen and B. Raveau, J. Solid State Chem. **142**, 247-260 (1999).

[14] "Magnetoresistance in the oxygen deficient $LnBaCo_2O_{5.4}$ (Ln = Eu, Gd) phases",

C. Martin, A. Maignan, D. Pelloquin, N. Nguyen and B. Raveau, Appl. Phys. Lett. **71**, 1421-1423 (1997).

[15] "Charge ordering in the layered Co-based perovskite $HoBaCo_2O_5$",
E. Suard, F. Fauth, V. Caignaert, I. Mirebeau and G. Baldinozzi, Phys. Rev. B **61**, R11871-R11874 (2000).

[16] "Effect of Oxygen Content and Oxygen Vacancy Ordering on the properties of $TbBaCo_2O_{6-\delta}$",
N. V. Kasper, I. O. Troyanchuk, D. D. Khalyavin, N. Hamad, L. Haupt, P. Fröbel, K. Bärner, E. Gmelin, Q. Huang and J. W. Lynn, Phys. Stat. Sol. B **215**, 697-701 (1999).

[17] "Low to High Spin-State Transition Induced by Charge Ordering in Antiferromagnetic $YBaCo_2O_5$",
T. Vogt, P. M. Woodward, P. Karen, B. A. Hunter, P. Henning and A. R. Moodenbaugh, Phys. Rev. Lett. **84**, 2969-2972 (2000).

[18] "Reentrant paramagnetic behavior and spin-state transition in the layered cobalt oxide $GdBaCo_2O_{5+\delta}$",
W. S. Kim, E. O. Chi, H. S. Choi, N. H. Hur, S. J. Oh and H. C. Ri, Solid State Commun. **116**, 609-614 (2000).

[19] "Interplay of structural, magnetic and transport properties in the layered Co-based perovskite $LnBaCo_2O_5$ (Ln = Tb, Dy, Ho)",
F. Fauth, E. Suard, V. Caignaert, B. Domenges, I. Mirebeau and L. Keller, Eur. Phys. J. B **21**, 163-174 (2001).

[20] "Metal-insulator transition induced by a spin-state transition in $TbBaCo_2O_{5+\delta}$ (δ = 0.5)",
Y. Moritomo, T. Akimoto, M. Takeo, A. Machida, E. Nishibori, M. Takata, M. Sakata, K. Ohoyama and A. Nakamura, Phys. Rev. B **61**, R13325-R13328 (2000).

[21] "Optical Study of Metal-Insulator Transition in $SmBaCo_2O_{6-\delta}$ Single Crystal",
T. Saito, T. Arima, Y. Okimoto and Y. Tokura, J. Phys. Soc. Jpn. **69**, 3525-3528 (2000).

[22] "Effect of iron doping on the properties of $TbBaCo_2O_{5.5}$ layered perovskite",
M. Kopcewicz, D. D. Khalyavin, I. O. Troyanchuk, H. Szymczak, R. Szymczac, D. J. Logvinovich and E. N. Naumovich, J. Appl. Phys. **93**, 479-486 (2003).

[23] "A Ferrimagnetic Manganese Oxide with a Layered Perovskite Structure: $YBaMn_2O_5$",
J. P. Charpman, J. P. Attfield, M. Molgg, C. M. Friend and T. P. Beales, Angew. Chem.

35, 2482-2484 (1996).

[24] "Giant Negative Magnetoresistance in Perovskitelike $La_{2/3}Ba_{1/3}MnO_x$ Ferromagnetic Films",
R. von Helmolt, J. Wecker, B. Holzapfel, L. Schultz and K. Samwer, Phys. Rev. Lett. **71**, 2331-2333 (1993).

[25] "Magnetoresistance in magnetic manganese oxide with intrinsic antiferromagnetic spin structure",
K.-I. Chahara, T. Ohno, M. Kasai and Y. Kozono, Appl. Phys. Lett. **63**, 1990-1992 (1993).

[26] "A variable temperature neutron diffraction study of the layered perovskite $YBaMn_2O_5$",
J. A. McAllister and J. P. Attfield, J. Mater. Chem. **8**, 1291-1294 (1998).

[27] "Order-Disorder Phenomena in New $LaBaMn_2O_{6-x}$ CMR Perovskites. Crystal and Magnetic Structure",
F. Millange, V. Caignaert, B. Domengès and B. Raveau, Chem. Mater. **10**, 1974-1983 (1998).

[28] "Successive Phase Transitions in a Metal-Ordered Manganite Perovskite $YBaMn_2O_6$",
T. Nakajima, H. Kageyama and Y. Ueda, J. Phys. Chem. **63**, 913 (2002).

[29] "Change in charge and orbital alignment upon antiferromagnetic transition in the *A*-site-ordered perovskite manganese oxide $RBaMn_2O_6$ (R = Tb and Sm)",
T. Arima, D. Akahoshi, K. Oikawa, T. Kamiyama, M. Uchida, Y. Matsui and Y. Tokura, Phys. Rev. B **66**, 140408(R) (2002).

[30] "Charge/Orbital Ordering Structure in Ordered Perovskite $Sm_{1/2}Ba_{1/2}MnO_3$",
M. Uchida, D. Akahoshi, R. Kumai, Y. Tomioka, T. Arima, Y. Tokura and Y. Matsui, J. Phys. Soc. Jpn. **71**, 2605-2608 (2002).

[31] "Synthesis and Properties of $YBaMn_2O_{5+\delta}$",
T. P. Beales, M. Mölgg, J. Jutson and C. M. Friend, Phys. State. Sol. **161**, 271-282 (1997).

[32] "$YBaMn_2O_5$: Crystal and Magnetic Structure Reinvestigation",
F. Millange, E. Suard, V. Caignaert and B. Raveau, Mater. Res. Bull. **34**, 1-9 (1999).

[33] "Spin, charge, and orbital ordering in the ferromagnetic insulator $YBaMn_2O_5$",
R. Vidya, P. Ravindran, A. Kjekshus and H. Fjellvåg, Phys. Rev. B **65**, 144422 (2002).

[34] "Alternative charge-order polymorph for harf-doped manganites in $TbBaMn_2O_6$",

A. J. Williams and J. P. Attfield, Phys. Rev. B **66**, 220405R (2002).

[35] "$YBa_2Fe_3O_8$ and the YCu(O)–BaCu(O)–YFe(O)–BaFe(O) Phase Diagram", P. Karen, P. H. Andersen and A. Kjekshus, J. Solid State Chem. **101**, 48-58 (1992).

[36] "Layered (Cu,Fe) oxides of double perovskite structure. II. Extension of solid solubility of copper in (Ba,La)$Y(Cu_{0.5+x}Fe_{0.5-x})_2O_{5+\delta}$ via high-pressure heat treatment", M. Nagase, J. Lindén, H. Suematsu, M. Karppinen and H. Yamauchi, Phys. Rev. B **59**, 1377-1382 (1999).

[37] "Synthesis and structural investigations of the double perovskites $REBaFe_2O_{5+w}$ (RE = Nd, Sm)", P. Karen and P. M. Woodward, J. Mater. Chem. **9**, 789-797 (1999).

[38] "Valence-state mixing and separation in $SmBaFe_2O_{5+w}$", J. Lindén, P. Karen, A. Kjekshus, J. Miettinen, T. Pietari, M. Karppinen, Phys. Rev. B **60**, 15251-15260 (1999).

[39] "Verwey transition in mixed-valence $TbBaFe_2O_5$: Two attempts to order charges", P. Karen, P. M. Woodward, J. Lindén, T. Vogt, A. Studer, P. Fischer, Phys. Rev. B **64**, 214405-214419 (2001).

[40] "Verwey Transition under Oxygen Loading in $RBaFe_2O_{5+w}$ (R = Nd and Sm)", P. Karen, P. M. Woodward, P. N. Santhosh, T. Vogt, P. W. Stephens and S. Pagola, J. Solid State Chem. **167**, 480-493 (2002).

[41] "Effects of oxygen nonstoichiometry and of its distribution on Verwey-type transition and structure of $GdBaFe_2O_{5+w}$", P. Karen, J. Solid State Chem. (to be published).

[42] "Charge Disproportionation in $CaFeO_3$ Studied with the Mössbauer Effect", M. Takano, N. Nakanishi, Y. Takeda, S. Naka and T. Takada, Mater. Res. Bull. **12**, 923-928 (1977).

[43] Y. Takeda, S. Naka and Y. Takeda, J. de Physique **40**, C2 331 (1979).

[44] M. Takano, J. Kawauchi, N. Nakanishi and Y. Takeda, J. Solid State Chem. **39**, 75 (1981).

[45] Y. Takeda, K. Kajiura, S. Naka and M. Takano, Froc. Inter. Conf. Kyoto, 929 (1980).

[46] M. Takano, N. Nakanishi, Y. Takeda, S. Naka and T. Takeda, Mat. Res. Bull., **12**, 923 (1977).

[47] "Valence State of the Fe Ions in $Sr_{1-y}La_yFeO_3$",

M. Takano, J. Kawachi, N. Nakanishi and Y. Takeda, J. Solid State Chem. **39**, 75-84 (1981).

[48] "The Structural Consequences of Charge Disproportionation in Mixed-Valence Iron Oxides. I. The Crystal Structure of $Sr_2LaFe_3O_{8.94}$ at Room Temperature and 50 K", P. D. Battle, T. C. Gibb and P. Lightfoot, J. Solid State Chem. **84**, 271-279 (1990).

[49] "Charge Ordered States in $La_{1-x}Sr_xFeO_3$", J. Q. Li, Y. Matsui, S. K. Park and Y. Tokura, Phys. Rev. Lett. **79**, 297-300 (1997).

[50] "Optical spectroscopy of charge-ordering transition in $La_{1/3}Sr_{2/3}FeO_3$", T. Ishikawa, S. K. Park, T. Katsufuji, T. Arima and Y. Tokura, Phys. Rev. B **58**, R13326-R13329 (1998).

[51] E. Garcia-Gonzalez, M. Parras, J. M. Gonzalez and M. Vallet-Regi, J. Solid State Chem. **124**, 278 (1996).

[52] "Variation of charge-ordering transitions in $R_{1/3}Sr_{2/3}FeO_3$ (R = La, Pr, Nd, Sm, and Gd)", S. K. Park, T. Ishikawa, Y. Tokura, J. Q. Li and Y. Matsui, Phys. Rev. B **60**, 10788-10795 (1999).

[53] "Charge Ordering and Magnetotransport Transitions in $Sm_{1/3}Sr_{2/3}FeO_{3-\delta}$", Y. M. Zhao, M. Hervieu, N. Nguyen and B. Raveau, J. Solid State Chem. **153**, 140-144 (2000).

[54] J. Mizusaki, M. Okuyasu, S. Yamauchi and K. Fueki, J. Solid State Chem. **99**, 166 (1992).

[55] "Electric Conduction of Magnetite (Fe_3O_4) and its Transition Point at Low Temperatures", E. J. W. Verwey, Nature (London) **144**, 327-328 (1939).

[56] "Dielectric Spectroscopy of Ferromagnetic Semiconductors", P. A. Miles, W. B. Westphal and A. von Hippel, Rev. Mod. Phys. **29**, 279-307 (1957).

[57] "Physical Properties and Cation Arrangement of Oxides with Spinel Structures II. Electronic Conductivity", E. J. W. Verwey, P. W. Haayman and F. C. Romeijan, J. Chem. Phys. **15**, 181-187 (1947).

[58] "Electronic Conduction in Oxides", N. Tsuda *et al.*, Springer-Verlag, Berlin, Heidelberg (1991).

[59] "^{57}Fe Mössbauer spectroscopic examination of a single crystal of Fe_3O_4",
F. J. Berry, S. Skinner and M. F. Thomas, J. Phys. Condens. Matter **10**, 215-220 (1998).

[60] "The low-temperature crystal structure of magnetite",
H. P. Rooksby and B. T. M. Willis, Acta Cryst. **6**, 565-566 (1953).

[61] "Crystal symmetry of the low temperature phase of magnetite",
M. Iizumi and G. Shirane, Solid State Commun. **17**, 433-436 (1975).

[62] "X-Ray Study of the Phase Transition in Magnetite",
J. Yoshido and S. Iida, J. Phys. Soc. Jpn. **47**, 1627-1633 (1979).

[63] "Charge ordering in magnetite at low temperatures",
J. M. Zuo, J. C. H. Spence and W. Petuskey, Phys. Rev. B **42**, 8451-8464 (1990).

[64] "NMR in magnetite below and around the Verwey transition",
P. Novák, H. Štěpánková, J. Englich, J. Kohout and V. A. M. Brabers, Phys. Rev. B **61**, 1256-1260 (2000).

[65] "Structure of Magnetite (Fe_3O_4) below the Verwey Transition Temperature",
M. Iizumi, T. F. Koetzle, G.Shirane, S. Chikazumi, M. Matsui and S. Todo, Acta Cryst. B**38**, 2121-2133 (1982).

[66] "Resonant "Forbidden" Reflections in Magnetite",
J. García, G. Subías, M. G. Proietti, H. Renevier, Y. Joly, L. L. Hodeau, J. Blasco, M. C. Sánchez and J. F. Bérar, Phys. Rev. Lett. **85**, 578-581 (2000).

[67] "High-pressure study of Fe_3O_4 through the Verwey transition",
S. K. Ramasesha, M. Mohan, A. K. Singh, J. M. Honig and C. N. R. Rao, Phys. Rev. B **50**, 13789-13791 (1994).

[68] "Effect of pressure on the metal-nonmetal transition and conductivity of Fe_3O_4",
G. A. Samara, Phys. Rev. Lett. **21**, 795-797 (1968).

[69] H. H. Schloessin and R. Govidarajan, in High Pressure in Science and Technology, edited by C.Homan, R. K. MacCrone, and E.Whalley, MRS Symposia Proceedings No. 22 (Materials Research Society, Pittsburgh, 1984), p. 345.

[70] "Pressure effect on the anomalous electrical conductivity of magnetite",
Y. Kakudate, N. Mori and Y. Kino, J. Magn. Magn. Mater. **12**, 22-25 (1979).

[71] "Pressure Dependence of the Verwey Transition of $Fe_{3-y}O_4$ Obtained by Magnetic Permeability Measurements",
S. Tamura, J. Phys. Soc. Jpn. **59**, 4462-4465 (1990).

[72] "Metallization of magnetite (Fe_3O_4) under high pressure",
S. Todo, N. Takeshita, T. Kanehara, T. Mori and N. Môri, J. Appl. Phys. **89**, 7347-7349 (2001).

[73] "Electron states, magnetism, and the Verwey transition in magnetite",
Ze Zhang and Sashi Satpathy, Phys. Rev. B **44**, 13319-13331 (1991).

[74] "Band Structure in the High Temperature Phase of Fe_3O_4",
A. Yanase and K. Siratori, J. Phys. Soc. Jpn. **53**, 312-317 (1984).

[75] "Spin-resolved photoelectron spectroscopy of Fe_3O_4",
S. A. Morton, G. D. Waddill, S. Kim, I. K. Schuller, S. A. Chambers and J. G. Tobin, Surf. Sci. **513**, L451-L457 (2002).

[76] "Evidence for the half-metallic ferromagnetic state of Fe_3O_4 by spin-resolved photoelectron spectroscopy",
Y. S. Dedkov, U. Rüdiger and G. Güntherodt, Phys. Rev. B **65**, 064417 (2002).

[77] "Oxidation of the Fe(110) surface: An Fe_3O_4(111)/Fe(110) bilayer",
H. -J. Kim, J. –H. Park and E. Vescovo, Phys. Rev. B **61**, 15284-15287 (2000).

[78] "Fe_3O_4(111)/Fe(110) magnetic bilayer: Electronic and magnetic properties at the surface",
H. -J. Kim, J. –H. Park and E. Vescovo, Phys. Rev. B **61**, 15288-15293 (2000).

[79] "New Class of Materials: Half-Metallic Terromagnets",
R. A. de Groot and F. M. Mueller, Phys. Rev. Lett. **50**, 2024-2027 (1983).

[80] "Magnetic and crystallographic properties of several $C1_b$ type Heusler compounds",
R. B. Helmholdt, R. A. de Groot, F. M. Mueller, P. G. Van Engen and K. H. J. Buschow, J. Magn. Magn. Matter. **43**, 249-255 (1984).

[81] "Thousandfold Change in Resistivity in Magnetoresistive La-Ca-Mn-O Films",
S. Jin, T. H. Tiefel, M. Mc-Cormack, R. A. Fastnacht, P. Ramesh and L. H. Chen, Science **264**, 413-415 (1994).

[82] "Electronic structure of $La_{0.5}Ca_{0.5}MnO_3$",
P. K. de Boer, H. van Leuken, R. A. de Groot, T. Rojo and G. E. Barberis, Solid State Commun. **102**, 621-626 (1997).

[83] "Electronic structure and half-metallic transport in the $La_{1-x}Ca_xMnO_3$ system",
Warren E. Pickett and David J. Singh, Phys. Rev. B **53**, 1146-1160 (1996).

[84] "CrO2 predicted as a half-metallic ferromagnet",

K. Schwarz, J. Phys. F: Met. Phys. **16**, L211-L215 (1986).

[85] "CrO_2: A self-Doped Double Exchange Ferromagnet",
M. A. Korotin, V. I. Anisimov, D. I. Khomskii and G. A. Sawatzky, Phys. Rev. Lett. **80**, 4305-4308 (1998).

[86] "Room-temperature magnetoresistance in an oxide material with an ordered double-perovskite structure",
K. -I. Kobayashi, T. Kimura, H. Sawada, K. Terakura and Y. Tokura, Nature (London) **395**, 677-680 (1998).

[87] "Evidence for valence fluctuation of Fe in Sr_2FeMoO_{6-w} double perovskite",
J. Lindén, T. Yamamoto, M. Karppinen and H. Yamauchi, Appl. Phys. Lett. **76**, 2925-2927 (2000).

[88] "The Thermodynamics of Substances of Interest in Iron and Steel Making from 0 °C to 2400 °C",
F.D. Richardson and J.H.E. Jeffes, J. Iron Steel Inst. **160**, 261-270 (1948).

[89] "Structure and Magnetism of $Pr_{1-x}Sr_xFeO_{3-\delta}$",
H. W. Brinks, H. Fjellvåg, A. Kjekshus and B. C. Hauback, J. Solid State Chem. **150**, 233-249 (2000).

[90] "A ^{57}Fe Mössbauer Study of the Cubic Perovskite-Type Phase $LaBa_2Fe_3O_{8+w}$ ($-0.20 < w < 0.83$)",
J. Lindén, M. Lippmaa, P. Karen, A. Kjekshus and M. Karppinen, J. Solid State Chem. **138**, 87-97 (1998).

[91] "The system iron-oxygen, I. The wüstite field and related equilibria",
L. S. Darken and R. W. Gurry, J. Am. Chem. Soc. **67**, 1398-1412 (1945).

[92] "The system iron-oxygen, II. Equilibrium and thermodynamics of liquid oxide and other phases",
L. S. Darken and R. W. Gurry, J. Am. Chem. Soc. **68**, 798-816 (1946).

[93] "Equilibrium relationships of Fe_3O_4, Fe_2O_3, and oxygen",
J. W. Greig, E. Posnjak, H. E. Merwin and R. B. Sosman, Am. J. Sci. **30**, 239-316 (1935).

[94] "Phase Equilibria among Oxides in Steel Making",
A. Muan and E. F. Osborn, 236 pp., Addison Wesley, Reading, MA, (1965).

[95] "Stability relations of iron oxides: phase equilibria in the system Fe_3O_4-Fe_2O_3 at

oxygen pressures up to 45 atmospheres",
B. Phillips and A. Muan, J. Phys. Chem. **64**, 1451-1453 (1960).

[96] "Giant negative magnetoresistance in perovskitelike $La_{2/3}Ba_{1/3}MnO_x$ ferromagnetic films",
R. von Helmolt, J. Wecker, B. Holzapfel, L. Schultz and K. Samwer, Phys. Rev. Lett. **71**, 2331-2333 (1993).

[97] "Giant Magnetotransport Phenomena in Filling-Controlled Kondo Lattice System: $La_{1-x}Sr_xMnO_3$",
Y. Tokura, A. Urushibara, Y. Moritomo, T. Arima, A. Asamitsu, G. Kido and N. Furukawa, J. Phys. Soc. Jpn. **63**, 3931-3935 (1994).

[98] "Low Temperature Magnetoresistance and the Magnetic Phase Diagram of $La_{1-x}Ca_xMnO_3$",
P. Schiffer, A. P. Ramirez, W. Bao and S.-W. Cheong, Phys. Rev. Lett. **75**, 3336-3339 (1995).

[99] "Magnetic and electronic properties of a single crystal of ordered double perovskite Sr_2FeMoO_6",
Y. Tomioka, T. Okuda, Y. Okimoto, R. Kumai, K.-I. Kobayashi and Y. Tokura, Phys. Rev. B **61**, 422-427 (2000).

[100] "Structure and Magnetic Studies of Ordered Oxygen-Deficient Perovskites $LnBaCo_2O_{5+\delta}$, Closely Related to the "112" Structure",
A. Maignan, C. Martin, D. Pelloquin, N. Nguyen and B. Raveau, J. Solid State Chem. **142**, 247-260 (1999).

[101] "Ordering and Antiferromagnetism in Ferrites",
P. W. Anderson, Phys. Rev. **102**, 1008-1013 (1956).

[102] "Revised Effective Ionic Radii and Systematic Studies of Interatomic Distances in Halides and Chalcogenides",
R. D. Shannon, Acta Cryst. **A32**, 751-767 (1976).

[103] "Novel methods of synthesis and wet-chemical redox analysis for magnetoresistive double-perovskite Sr_2FeMoO_{6-w}",
T. Yamamoto, J. Liimatainen, J. Lindén, M. Karppinen and H. Yamauchi, J. Mater. Chem. **10**, 2342-2345 (2000).

[104] "Influence of W/Ta Substitution at the Mo Site on the Fe Valence and

Magnetoresistive Properties of Sr_2FeMoO_6",
J. Lindén, T. Yamamoto, H. Yamauchi and M. Karppinen, Physica B **312-313**, 787-788 (2002).

[105] "Iron valence in double-perovskite $(Ba,Sr,Ca)_2FeMoO_6$: Isovalent substitution effect", R Y. Yasukawa, M. Karppinen, J. Linden, T. S. Chan, R. S. Liu, and H. Yamauchi, Phys. Rev. B, submitted (2003).

[106] "Observation of Antiphase Boundaries in Sr_2FeMoO_6",
J. Lindén, M. Karppinen, T. Shimada, Y. Yasukawa and H. Yamauchi, Phys. Rev. B, submitted (2003).

Acknowledgments

My supervisor, professor Hisao Yamauchi and professor Maarit Karppinen are gratefully acknowledged for their good suggestions, fruitful discussions and supports for whole my study life.

Dr. Sergey R. Lee is gratefully acknowledged for his significant suggestions in sample preparation by encapsulation technique with oxygen getter, and that was a start point of my study. Important suggestions, discussions, writing the papers and the helps of my study by Dr. Johan Lindén, Dr. Veer Pal Singh Awana and professor Pavel Karen are acknowledged.

I am grateful to Dr. Masaya Uchida and Dr. Yoshio Matsui for the TEM observations. I should be grateful to professor Satoshi Sasaki for his help of synchrotron XRD at Spring-8. Professor Noriaki Hamada is acknowledged for the band structure calculations.

Dr. Teruki Motohashi and professor Hisayuki Suematsu are gratefully acknowledged for taking care of me in my student life.

The members who I have studied with in Yamauchi-Karppinen group, Dr. T. Akao, Dr. H. Yunhui, Dr. T. Nakane, Dr. N. Kiryakov, Mr. H. Okamura, Mr. T. Hosomi, Mr. Y. Takahama, Mr. M. Kochi, Mr. Y. Morita, Mr. T. Yamamoto, Mrs. Yasukawa, Mr. T. Nagashima, Mr. S. Ichihara, Mr. R. Ueda, Ms. M. Ushiki, Mr. M. Kitabatake, Mr. M. Yaegashi, Mr. K. Mizogami, Mr. T. Shimada, Mr. Y. Shimizu, Mr. T. Watanabe, Mr. P. Germanas, Mr. H. Okamoto, Mr. T. Konno, Mr. T. Nomura, Y. Hirota, Mr. T. Fujita, Mr. K. Sakai, Mr. M. Matvejeff, Mr. E. Naujalis, Ms. J. Lybeck, Ms. J. Poulsen, Mr. Kobayashi, Mr. K. Mori, Mrs. A. Takahashi, Mrs. J. Yanagihara are acknowledged for the help of various things in my student life.

March, 2003

Jin Nakamura

Curriculum Vitae

Name: Jin NAKAMURA

Birth: Sept. 29, 1974 in Yamato-shi, Japan

Nationality: Japanese

Education :

1994.4 – 1998.3 : Department of Applied Physics, Applied Physics, Faculty of Science, Tokyo University of Science.

1998.3 : Batchelor of Science (Tokyo University of Science).

1998.4 – 2000.3 : Department of Innovative and Engineered Materials, Interdisciplinary Graduate School of Science and Engineering, Tokyo Institute of Technology (Master Course).

2000.3 : Master of Science (Tokyo Institute of Technology).

2000.4 – present : Department of Innovative and Engineered Materials, Interdisciplinary Graduate School of Science and Engineering, Tokyo Institute of Technology (Doctoral Course).

List of Publications :

1. "Iron Mixed-Valent Compounds, $BaSm(Cu_{0.5+x}Fe_{0.5-x})_2O_{5+\delta}$. I: Synthesis and Chemical Characterization",
J. Nakamura, J. Lindén, H. Suematsu, M. Karppinen and H. Yamauchi, Physica C **338**, 121-125 (2000).

2. "Iron Mixed-valent Compounds, $BaSm(Cu_{0.5+x}Fe_{0.5-x})_2O_{5+\delta}$. II: The $Fe^{2.5+}$ State and Magnetic Properties",
J. Lindén, **J. Nakamura**, T. Pietari, T. Taniyama, M. Karppinen and H. Yamauchi, Physica C **338**, 126-131 (2000).

3. "Magnetoresistance Effect in the Fluctuating-Valence $BaSmFe_2O_{5+w}$ System",
J. Nakamura, J. Lindén, M. Karppinen and H. Yamauchi, Appl. Phys. Lett. **77**, 1683-1685 (2000).

4. "Observation of Mixed-Valence State in the $BaSm(Cu_{1-x}Fe_x)_2O_{5+\delta}$ Double-Perovskite Phase",
J. Lindén, **J. Nakamura**, P. Karen, A. Kjekshus, M. Karppinen and H. Yamauchi, In: Advances in Superconductivity XII, T. Yamashita and K. Tanabe (Eds.), Springer, Tokyo **2000**, pp. 95-97.

5. "Synthesis and Magnetism of Pr-Based Rutheno-Cuprate Compound $RuSr_2PrCu_2O_{8-\delta}$",
V.P.S. Awana, **J. Nakamura**, M. Karppinen, H. Yamauchi, S.K. Malik and W.B. Yelon, Physica C **357-360**, 121-125 (2001).

6. "Magnetoresistance Peak in the Vicinity of the Charge Disproportionation/Ordering Transition in the $R_{1/3}Sr_{2/3}FeO_{3-\delta}$ (R = La, Pr) Perovskite",
V.P.S. Awana, **J. Nakamura**, J. Lindén, M. Karppinen and H. Yamauchi, Solid State Commun. **119**, 159-162 (2001).

7. "Co-existence of Intrinsic and Extrinsic Magnetoresistance in the Double-Perovskite $Sr_2Fe(Mo_{1-x}W_x)O_{6-w}$ System",
J. Lindén, T. Yamamoto, **J. Nakamura**, M. Karppinen and H. Yamauchi, Appl. Phys. Lett. **78**, 2736-2738 (2001).

8. "Possible Ordering of Ru and Cu in the Charge-Reservoir of Magneto-Superconductor $RuSr_2GdCu_2O_8$ (Ru-1212): Magnetic, Transport, and TEM Microstructural Studies",
V.P.S. Awana, S. Ichihara, **J. Nakamura**, M. Karppinen, H. Yamauchi, J. Yang, W.B. Yelon, W.J. James and S.K. Malik, J. Appl. Phys. **91**, 8501-8503 (2002).

9. "Hole-Doping Effect on the Verwey-Type Transition and Magnetoresistivity of $Ba(Sm,Ca)Fe_2O_{5+\delta}$",
J. Nakamura, J. Lindén, H. Yamauchi and M. Karppinen, Solid State Commun. **121**, 269-274 (2002).

10. "Glass Component Induced Hysteresis/Memory Effect in Magnetoresistance of $Pr_{0.9}Sr_{0.1}CoO_{2.99}$",
V.P.S. Awana, **J. Nakamura**, M. Karppinen, H. Yamauchi and S.K. Malik, J. Magn. Magn. Mater. **250**, 6-11 (2002).

11. "Control of Fe valence state and magnetoresistance by means of T = Ta and W substitution in $Sr_2Fe(Mo_{1-x}T_x)O_6$",
J. Lindén, T. Yamamoto, **J. Nakamura**, H.Yamauchi and M. Karppinen, Phys. Rev. B **66**, 184408-184414 (2002).

12. "Magnetoresistance about the Verwey-type transition in $BaGdFe_2O_{5+w}$",
J. Nakamura, J. Lindén, P. Karen, H.Yamauchi and M. Karppinen, in preparation.

13. "Verwey-type transition in $(Ba,Sr)REFe_2O_{5.0}$: Isovalent cation substitution effects",
J. Nakamura, H.Yamauchi and M. Karppinen, in preparation.

List of Presentations :

1. "Studies on Double Perovskites, $A'A''(Cu_{0.5+x}Fe_{0.5-x})_2O_{5+\delta}$ II : Synthesis and Preliminary Characterization of Novel Double-Perovskite Iron Oxides $BaREFe_2O_{5+\delta}$",
   J. Nakamura, H. Suematsu, M. Karppinen and H. Yamauchi, The Japan Society of Applied Physics and Related Societies (The 46th Spring Meeting), Mar. 28-31, 1999, Tokyo Univ. Science (Chiba).

2. "Studies on Double Perovskites, $A'A''(Cu_{0.5+x}Fe_{0.5-x})_2O_{5+\delta}$ III : Control of the Mixed Valence of Iron in $BaREFe_2O_{5+\delta}$",
   J. Nakamura, H. Suematsu, J. Lindén, M. Karppinen and H. Yamauchi, The Japan Society of Applied Physics and Related Societies (The 60th Autumn Meeting), Sep. 1-4, 1999, Kounan Univ. (Hyogo).

3. "Iron Mixed-Valence Compounds, $BaSm(Cu_{0.5+x}Fe_{0.5-x})_2O_{5+\delta}$ I : Synthesis and Characterization",
   J. Nakamura, J. Lindén, T. Taniyama, H. Suematsu, M. Karppinen and H. Yamauchi, 5th International Workshop on Chemical Designing and Processing of High-T_c Superconductors (Chem-HTSC V), Oct. 15-16, 1999, Tokyo Inst. Tech. (Kanagawa).

4. "Studies on Double Perovskite, $A'A''(T,Fe)_2O_{5+\delta}$ IV : Solubility of Cu and Control of Excess Oxygen in the $BaSm(Cu_{0.5+x}Fe_{0.5-x})_2O_{5+\delta}$ Double Perovskite",
   J. Nakamura, J. Lindén, M. Karppinen and H. Yamauchi, The Japan Society of Applied Physics and Related Societies (The 47th Spring Meeting), Mar. 28-31, 2000, Aoyama Gakuin Univ. (Tokyo).

5. "Iron-Oxide Double Perovskites (I) : Valence Fluctuation and Magnetoresistivity in $BaSmFe_2O_{5+\delta}$",
   J. Nakamura, J. Lindén, M. Karppinen and H. Yamauchi, The Physical Society of Japan (The 55th Meeting), Sep. 22-25, 2000, Niigata Univ. (Niigata).

6. "Control of Charge Mixing/Separation and Magnetoresistance by Means of Oxygen Doping and Cation Substitution in the Double Perovskite Ba(Sm,Ca)$Fe_2O_{5+\delta}$",
J. Nakamura, J. Lindén, M. Karppinen and H. Yamauchi, 6th International Workshop on Chemical Designing and Processing of High-T_c Superconductors (Chem-HTSC VI), Oct. 12-13, 2000, Tokyo Inst. Tech. (Kanagawa).

7. "Iron-Oxide Double Perovskites (III) : Cation Substitution Effects in (Ba,Sr)*RE*$Fe_2O_{5+\delta}$",
J. Nakamura, J. Lindén, V. P. S. Awana, M. Karppinen and H. Yamauchi, The Physical Society of Japan (The 56th Meeting), Mar. 27-30, 2001, Chuo Univ. (Tokyo).

8. "Chemical Control of Verwey-Type Transition and Magnetoresistance Properties of Double Perovskite (Ba,Sr)(*RE*,Ca)$Fe_2O_{5+\delta}$",
T. Motohashi, **J. Nakamura**, J. Lindén, M. Karppinen and H. Yamauchi, The Physical Society of Japan (The 57th Meeting), Sep. 17-20, 2001, Tokushima Bunri Univ. (Tokushima).

9. "Mixed-Valence State and Charge Ordering in Double Perovskite Ba*RE*$Fe_2O_{5+\delta}$ (*RE* = Y, Dy, Eu, Sm, Nd)",
J. Nakamura, M. Uchida, Y, Matsui, T. Motohashi, J. Lindén, M. Karppinen and H. Yamauchi, The Japan Society of Applied Physics and Related Societies (The 49th Spring Meeting), Mar. 27-30, 2002, Tokai Univ. (Kanagawa).

10. "Charge Separation/Ordering in Oxygen-Deficient Double Perovskite Ba*RE*$Fe_2O_{5.0}$",
J. Nakamura, M. Uchida, Y. Matsui, J. Lindén, T. Motohashi, M. Karppinen and H. Yamauchi, The Physical Society of Japan (Autumn Meeting), Sep. 6-9, 2002, Chubu Univ. (Aichi).

11. "Isovalent Substitution Effects in (Ba,Sr)*RE*$Fe_2O_{5+\delta}$",
J. Nakamura, M. Karppinen and H. Yamauchi, 8th International Workshop on Chemical Designing and Processing of High-T_c Superconductors and Related Materials (Chem-HTSC VIII), Nov. 8-9, 2002, Tokyo Inst. Tech. (Kanagawa).

12. "Isovalent Substitution Effect on the Verwey-Type Transition in an *A*-Site Ordered Double-Perovskite System, (Ba,Sr)*RE*$Fe_2O_{5.0}$",
J. Nakamura, M. Karppinen and H. Yamauchi, The Physical Society of Japan (The 58th Meeting), Mar. 28-31, 2003, Tohoku Univ. (Miyagi).

Miscellaneous :

Participated and completed a NORFA course on "The use of neutrons in structural studies of crystalline and disordered materials" held on 13-24 August 2001, in Studsvik and Uppsala, Sweden.